WORKSHOP ON INDUSTRIAL AND ENVIRONMENTAL APPLICATIONS OF DIRECT AND LARGE EDDY SIMULATIONS

August 5-7, 1988
Boğaziçi University
Istanbul

ABSTRACTS

REPORT DOCUMENTATION PAGE

Form Approved OMB No. 0704-0188

1. AGENCY USE ONLY (Leave blank)	2. REPORT DATE	3. REPORT TYPE AND DATES COVERED
	1 August 1998	Conference Proceedings

4. TITLE AND SUBTITLE

Industrial and Environmental Applications of Direct and Large Eddy Simulation of Turbulent Flows

5. FUNDING NUMBERS

F61775-98-WE078

6. AUTHOR(S)

Conference Committee

7. PERFORMING ORGANIZATION NAME(S) AND ADDRESS(ES)

Bogazici University
Bebek
Istanbul 80815
Turkey

8. PERFORMING ORGANIZATION REPORT NUMBER

N/A

9. SPONSORING/MONITORING AGENCY NAME(S) AND ADDRESS(ES)

EOARD
PSC 802 BOX 14
FPO 09499-0200

10. SPONSORING/MONITORING AGENCY REPORT NUMBER

CSP 98-1065

11. SUPPLEMENTARY NOTES

12a. DISTRIBUTION/AVAILABILITY STATEMENT

Approved for public release; distribution is unlimited.

12b. DISTRIBUTION CODE

A

13. ABSTRACT (Maximum 200 words)

The Final Proceedings for Industrial and Environmental Applications of Direct and Large Eddy Simulation of Turbulent Flows, 5 August 1998 - 7 August 1998

This is an interdisciplinary conference. Topics include: Large Eddy Simulation (LES); Direct Numerical Simulation (DNS); Mathematical and Computational Methods; and Turbulence (subgridscale) Closure.

14. SUBJECT TERMS

EOARD, Large Eddy Simulation (LES), Direct Numerical Simulation (DNS)

15. NUMBER OF PAGES

81

16. PRICE CODE

N/A

17. SECURITY CLASSIFICATION OF REPORT	18. SECURITY CLASSIFICATION OF THIS PAGE	19. SECURITY CLASSIFICATION OF ABSTRACT	20. LIMITATION OF ABSTRACT
UNCLASSIFIED	UNCLASSIFIED	UNCLASSIFIED	UL

CONTENTS

Direct and Large Eddy Simulation of Environmental Flows: Some Recent Advances

Joel H. Ferziger
Department of Mechanical Engineering
Stanford University
Stanford CA

August 1998

1 Introduction

Environmental and geophysical flows occur on much larger scales than flows in industrial devices; one consequence is that the Earth's rotation often plays a significant role in them. Furthermore, the horizontal scales are generally much larger than the vertical ones so that the motions on the largest scales are essentially two dimensional. Finally, stratification is often important in these flows, sometimes so much so that, despite the large scales and high Reynolds numbers, the flow state is essentially laminar. All of these effects make simulation of environmental flows very challenging and different from industrial flows.

One of the most difficult issues in simulation of these flows is the need to deal with the real world in real time. In weather or ocean prediction the goal is to predict the actual state of the system at some time not too far in the future rather than the statistical quantities that are typically needed in engineering. This requires simulation of a single realization rather than an ensemble average flow, providing a severe constraint on the approaches that can be used. There is a limit on how far into the future the state can be predicted—the well-known 'butterfly' problem. (Exceptions are climate studies and some types of pollution studies.)

The field is vast and no one paper or even a book could cover all of it. In this paper, we shall concentrate on some issues in small scale meteorology and oceanography. Although they deal with the smallest scales of interest in these fields, the dimensions are very large compared to those found in industrial applications. We may be dealing with the atmospheric boundary layer (typically 1-2 km deep), the oceanic mixed layer (typically 100-300 m deep), an estuary, or the atmosphere in an urban area and its surroundings; these have horizontal dimensions of tens of kilometers. On these scales, three dimensionality is important but Coriolis and stratification effects may also play major roles.

The difficulties of simulating these flows are considerable but the value of accurate predictions is enormous; the effects of weather and the state of the ocean are constantly in the news. We shall show, that even in some of the simpler flows, there remain issues to be resolved that differ from those encountered in industrial flows. Then we shall give some examples of some recent simulations in this area.

2 Environmental vs. Industrial Flows

With the exception of some very simple but important building block flows, direct numerical simulation (DNS) of turbulent flows is beyond the capability of present computers and will remain so for the indefinite future. For industrial flows, this leaves one with the choice of doing large eddy simulations (LES) or computations based on the Reynolds averaged Navier–Stokes (RANS) equations which employ well-known one point turbulence models. The trade-off is a simple one—the low cost of RANS vs. the improved accuracy and detail of LES. In the environmental area, the RANS concept might be applicable in some applications such as climate the prediction of the average state of an estuary but weather or oceanic state predictions must produce an accurate estimate of the actual future state. For that purpose, there is no choice but to use LES. Indeed, LES originated in meteorology as a response to this need.

As already noted, a typical LES of the atmospheric boundary layer or the oceanic mixed layer simulates a domain whose horizontal dimensions are hundreds of meters to tens of kilometers. The surfaces might be idealized as smooth but they are almost always rough on the scale of a typical near-surface turbulent eddy. As these flows do not normally separate (separation does occur in the presence of topography) and because it is impossible to represent the surface (let alone such features as trees) exactly, it is usually represented by means of an artificial boundary condition. Using such a condition also eliminates the need for a fine grid near the surface which increases the cost of engineering simulations. Due to the size of the domain and the fact that only about a hundred grid points can be used in each coordinate direction, the grid size or filter width must be tens of meters, which is much larger than the Kolmogoroff scale (typically a few centimeters). This would be no problem for homogeneous turbulence with a filter scale in the inertial subrange but significant dynamics occur at scales smaller than the grid size. For example, entrainment takes place in small zones at the edge of a plume or in the inversion at the top of the atmospheric boundary layer, a phenomenon that is difficult to simulate and remains a subject of research.

Consequently, there may be a dynamic length scale smaller than the subgrid scale cutoff. This makes it necessary to use a turbulence model in which the length scale is not pre-selected (as in the Smagorinsky model) and subgrid scale modeling may then resemble RANS modeling more than it does the kind of subgrid scale modeling used for laboratory scale flows. It also follows that the similarity required for the dynamic procedure to work may not be available in these flows.

At the larger scales of meteorology and oceanography, the flows become almost two dimensional and the Coriolis force, which plays a role at the small scales, becomes dominant. It goes without saying that DNS is totally impossible at these scales and the meaning of LES needs to be reconsidered. Solution of the Navier–Stokes equations is impossible and simplifications of them are often used; it is not unusual to solve different sets of equations at each scale. The averaging scales are now hundreds of kilometers and almost all of what an engineer would consider turbulence lies in the subgrid scale. Despite the dominance of two dimensionality, the weak motions in the vertical direction play an essential role and cannot be ignored entirely. At these scales the parameterization of the subgrid scales is required to represent a very wide range of phenomena and the difficulty of constructing them is extreme. A goal of smaller scale simulations is to provide these parameterizations; this task is made very difficult by the large range of parameters and conditions needed to specify the state of the smaller scale flow. Furthermore, the similarity on which the dynamic subgrid scale model is based does not exist at these scales because two dimensional turbulence is qualitatively different in character from three dimensional turbulence.

We shall describe some simulations relevant to environmental fluid mechanics, both DNS and LES, which have been done recently. Specifically, we look at turbulence subject to stratification and shear and the problem of upwelling in the coastal ocean.

3 Simulations

3.1 Stratified Sheared Homogeneous Turbulence

Homogeneous sheared turbulence has been studied from the earliest days of turbulence simulation; shear, of course, tends to amplify the intensity of turbulence. The addition of stable stratification introduces a force that tends to reduce the intensity of the turbulence by allowing conversion of its kinetic energy into potential energy. The interplay of the two forces is what makes the study of this type of flow interesting. The parameter traditionally used to characterize the relative importance of the two forces is the gradient Richardson number $Ri = (g/\rho)(\partial\rho/\partial z)/(\partial U/\partial z)^2$. Recent studies of inhomogeneous flows show that this parameter does not correlate the data well; for example, it varies by more than an order of magnitude with distance from the wall in stratified turbulent channel flow. A better parameter is the turbulent Froude number $Fr = q/NL$ where N is the Brunt-Väisälä frequency $N^2 = (g/\rho)(\partial\rho/\partial z)$. It can be regarded as the inverse square root of a Richardson number but it is based on turbulence rather than mean flow properties. The data can be correlated quite nicely with this variable. Especially important for correlation purposes is the mixing efficiency which is the roughly the fraction of the energy extracted from the mean flow that goes into the production of potential energy. It correlates very well as a function of Froude number.

There is also an important effect of the means of creation of the turbulence on the properties of the resulting turbulence. When shear is the primary forcing, the component of the turbulent fluctuations in the mean flow direction (which is usually horizontal in stratified flows) is larger than the other components. On the other hand, when turbulence is created by a grid oscillating in the vertical direction, the largest fluctuations are in the vertical direction; this is not a direct effect of the grid motion but is due to a selection process which allows vertical motions to penetrate further into the stratified fluid. The mixing efficiency correlation derived for shear turbulence does not work in this case and it is necessary to create a Froude number based on the vertical component of the turbulence to collapse all of the data. Turbulent diffusion (transport of turbulent energy through the agency of the third order correlations) exhibits similar differences in shear- and grid-generated turbulence and for similar reasons.

3.2 Oceanic Upwelling

An interesting phenomenon occurs on the eastern boundaries of oceans i.e. off the west coasts of continents. Here, one often finds stable high pressure areas (especially in local summer) which drive long-shore currents which, in the northern hemisphere, are from north to south. The Coriolis force drives these currents offshore and the surface water is replaced by deep ocean water that is colder and more nutrient-laden than the water it replaces. The deep water also has a different velocity than the surface water and the combination of velocity and density gradients can lead to an instability that makes the boundary between the two fluid masses very irregular. This upwelling process is responsible for a surprisingly large part of the mixing that occurs in the ocean; some estimates say that half of all mixing between surface and deep water is due to upwelling.

Despite the fact that the flow is turbulent, many of the properties of upwelling can be

predicted with the aid of linear stability theory. It is also possible to create a laboratory experiment that mimics the process and to perform simulations of it. Both of the latter have relatively smooth surfaces not representative of the actual ocean but it is possible to introduce idealizations of coastal geography and bathymetry. These show that capes and ridges cause significant increases in the mixing that occurs in the ocean.

Numerical Considerations in Large Eddy Simulation of Complex Turbulent Flows

Parviz Moin
Stanford University

We report on numerical issues in large eddy simulations that have been identified in recent computations and theoretical studies. These issues range from spatial discretizations to the impact of boundary conditions and grid resolution. We also describe the results from several large eddy simulations of complex turbulent flows including those performed with a novel numerical technique based on B-splines.

Computations of flow over a circular cylinder at the sub-critical Reynolds number of 3900 were carried out with a fifth order upwind biased scheme, second order central difference scheme and the B-spline method with a zonal grid. One-dimensional power spectra of the velocity fluctuations in the wake of the cylinder show that the inherent dissipation in the upwind scheme leads to very pronounced damping of the velocity fluctuations at medium to high frequencies. The agreement of the power spectra obtained with the B-spline method with the data is excellent. The non-dissipative second order scheme agrees with the data better than the fifth order upwind scheme. Near the cylinder, turbulence statistics from the three computations are in good agreement with each other, however, further downstream, the B-spline method is in significantly better agreement with the data. An interesting result from these computations was the demonstration that inadequate grid resolution can lead to early transition in shear layers emanating from the cylinder. A cautionary note is that such computations may show fortuitous agreement with experiments that also suffer from early transition due to external disturbances.

Additional examples of large eddy simulation of complex flows that will be presented are: combustion in a co-axial jet combustor, flow near the trailing edge of a hydrofoil and flow in an asymmetric diffuser. In the diffuser flow, it

will be demonstrated that the flow is very sensitive to inflow velocity profile. In the case of the combustor, the exit boundary has a profound effect on the vortex breakdown which is essential for flame stability and mixing in the combustor.

Finally, a summary of some of the current efforts aimed at making LES an engineering tool will be presented. Specifically, the development of suitable wall boundary conditions for LES and parallelization of LES codes will be discussed. Chapman's(1979) estimates for the required computational resources and the demonstrated capabilities of DOE's ASCI computers will be used to project the near term utility of LES.

Insights for LES from Structure-Based Turbulence Modeling

S. C. Kassinos and W. C. Reynolds
Department of Mechanical Engineering
Stanford University
Stanford, CA 94305-3030, USA

We have spent the past several years constructing improved one-point Reynolds-Averaged Navier-Stokes (RANS) turbulence models based on new structure concepts and new one-point tensors that carry important structural information. From this work we have learned a great deal about how (and why) homogeneous turbulence responds to different types of mean deformation. Insights from this work are important in Large Eddy Simulation (LES) because, except in the wall region, LES models assume local homogeneity.

The Smagorinski model and others like it assume equilibrium between the locally homogeneous sub-grid turbulent stress field and the instantaneous local strain rate of the resolved field. For some types of deformation, such an equilibrium might not even exist. If it does, the model should take into account the alteration of this equilibrium due to the type of mean deformation, and due to strong mean or frame rotation, but these effects are not properly included in any model that we have seen.

One key example is the case of turbulence subjected to an imposed axisymmetric expansion, say with mean (or large-eddy) strain-rates $S_{11} = -\Gamma$ and $S_{22} = S_{33} = \Gamma/2$. Analysis, DNS, and experiments all indicate that the Reynolds stress anisotropy in this flow is *larger* if the deformation is *slow* than if it is rapid. The anisotropy appears to grow continuously and shows no sign of leveling off at an equilibrium state. Moreover, upon removal of the imposed strain-rate, the stress anisotropy continues to *increase*, rather than returning to isotropy as the lore of turbulence says should happen. Since regions of local momentary axisymmetric expansion occur all over LES flows, it would seem that sub-grid models that could capture this effect would be preferable.

Another case where current LES sub-grid models are weak is in flows with strong frame or mean rotation. Under combinations of strain and rotation that lead to elliptical streamlines of the mean flow, the turbulence behaves very strangely. The turbulence state oscillates and does not equilibrate; DNS simulations (Blaisdell) shows that the kinetic energy of the turbulence grows, whereas quasi-equilibrium turbulence models of the sort used in LES for sub-grid turbulence predict decay.

The reasons for these seemingly strange effects become clear when one understands our new one-point structure tensors, the way that they are related, and the way that they are altered by mean deformation. All this should be useful in considering the way that sub-grid scale turbulence should be related to the imposed resolved-scale deformation. The purpose of this paper is to review what has been learned from our structure-based analyses, and to suggest how it might be applied in the development of better sub-grid turbulence models for LES.

Large-Eddy Simulation of Separation and Transition for Turbomachinery Flows

Peter R Voke[1] and Zhiyin Yang[2]

[1] University of Surrey, Guildford, U.K.
[2] University of Loughborough, U.K.

Abstract. Methods for the direct and large-eddy simulation of flows about turbomachinery blading are presented. For incompressible flows, both direct and large-eddy simulation require the solution of a Poisson equation for pressure, which is often the main source of computational expense in simulations within complex boundaries. Marked computational advantages are described for a flow which is periodic in one dimension through the use of Fourier techniques. With simple conditions fulfilled, it is possible to discrete Fourier transform the Poisson equation for the pressure field, decomposing the problem into a set of two-dimensional problems of similar type. We demonstrate that even when a complex geometry and body-fitted curvilinear coordinates are used in the other two dimensions, for instance to solve flow around a 2D turbine blade or blade row, the resulting Fourier-transformed 2D problems are much more efficiently solved than the 3D problem by iterative means.

We show results for the case of LES of flow over an idealised turbine leading edge shape. The simulation shows laminar separation from the point where the surface curvature changes, 2D instabilities in the separated shear layer, and breakdown to large-scale 3D structures prior to reattachment. Of particular interest is the interaction with the wake-like outer flow with the re-established shear at the wall, leading to a secondary boundary-layer transition similar to bypass transition. The simulation is carried out using general curvilinear coordinates with the contravariant velocity components and finite volume discretisation, together with a generalised dynamic subgrid scale model.

1 Introduction

Simulations of transition and turbulence over turbomachinery blades are necessarily three-dimensional. However they frequently need to be performed in computational domains in which one dimension can be assumed uniform, with a statistically homogeneous flow solution in that dimension which may be assumed to be periodic. Derivatives in the periodic direction can then be computed efficiently through the use of discrete Fourier transforms.

The periodic dimension is the spanwise dimension z. The requirements for the use of the Fourier method are: (i) That the unknown field whose solution is sought may be assumed periodic in z, an assumption which can be made if the turbulent pressure field is statistically homogeneous in z and the periodic length is greater than twice the correlation length of the field in z; (ii) that the mesh used in the z direction is even; and (iii) that any differencing formulae

applied to the field to generate the discretised equations are also homogeneous (this rules out certain types of upwind differencing in z).

The gains in computational efficiency through the use of Fourier methods are generally very significant. They arise partly because of the reduction of the dimension of the problem and the lack of any connection between the solution for different discrete wave numbers, and also partly because the higher wave-number problems have increased diagonal dominance in the solution of Poisson-like equations. This results in greatly accelerated convergence of the higher wave-number problems and a corresponding saving of computer resource.

A large-eddy simulation of flow over a NACA 4412 aerofoil has been performed by Kaltenbach and Choi [1] at an angle of attack of 12° and a chord Reynolds number of 1.64×10^6. They used body-fitted coordinates with second-order finite differences and the contravariant velocities discretised on a staggered mesh – a method which is very similar to that used by us for somewhat less ambitious flows. Their mesh of $638 \times 79 \times 48$ cells was barely adequate for an LES of the 4412 foil, with both streamwise and spanwise cell sizes being rather large in terms of wall units, and a number of less satisfactory results were noted. A smoothing filter was required to suppress grid-scale oscillations in the laminar flow upstream, and transition to turbulence was found to occur immediately following the region in which the filter was applied. Values of the shape factor H dropped more rapidly in the simulated boundary layer in the mid-chord region of the aerofoil than is found experimentally [2] and near the trailing edge there were substantial differences in the turbulence intensities between simulation and experiment.

2 Covariant Navier-Stokes equations

We are primarily interested in geometries that are quite complex in two dimensions such as a 2D aerofoil or turbine blade row. These situations naturally involve curved surfaces over which the development of boundary layers, including transition, separation, reattachment and sometimes relaminarisation is to be followed. Here the natural approach is to use general curvilinear coordinates, and this section describes one approach to this aspect of the simulation. Note, however, that the Fourier techniques described below for pressure solution also work very well for 2D geometries with sharp corners such as the flow over a square cylinder [3].

There are two main approaches to Navier-Stokes simulation in general curvilinear coordinates: one using scalar generalised equations for the conservation of Cartesian components of mementum; and a second method, used here, based on the fully general covariant Navier-Stokes equations representing the conservation of contravariant vector velocity components.

The familiar NS equations become

$$\partial_t(Ju^i) = -Jg^{ij}\partial_j p - J(u^i u^j)_{,j} + 2J(\nu s^{ij})_{,j} \qquad (1)$$

where J is the Jacobian of the coordinate transformation and g^{ij} is the metric tensor. These geometric quantities are computed in advance of the simulation to high accuracy. The equations are multiplied by the Jacobian of the transformation J in order to cast the equations and the discretisation in conservative form. p is the pressure over density. The strain rate is given by

$$s^{ij} = g^{ik}u^j_{,k} + g^{jk}u^i_{,k} = g^{ik}(\partial_k u^j + \Gamma^j_{kl}u^l) + i \leftrightarrow j \,, \tag{2}$$

an expression that involves the connection coefficients Γ^j_{kl} which are computed in advance. The symbol $+i \leftrightarrow j$ indicates the addition of symmetrising terms identical to those preceeding but with the indices i and j interchanged. ∂_j is the partial derivative with respect to x^j and the $_{,j}$ notation indicates the covariant derivative, also involving the connection coefficients. The covariant divergences in equation (1), for instance, are

$$J(u^i u^j)_{,j} = \partial_j(Ju^i u^j) + J\Gamma^i_{jk}u^k u^j \,, \tag{3}$$

and similarly for the viscous term. The mass conservation law in general coordinates reads

$$\partial_i(Ju^i) = 0 \,, \tag{4}$$

and hence one can derive a generalised Poisson equation for the pressure simply by taking the divergence of equation (1).

The momentum advancement is explicit except for the pressure term which is solved by a standard projection method. The spatial discretisation is performed by one of the standard approaches used in LES, with the geometric quantities computed to higher order in space in advance of the simulation for several distinct points of the staggered mesh arrangement. Note that all the geometric quantities are 2D fields, with values independent of z, greatly reducing the storage requirements.

3 Fourier pressure solution

We simulate turbomachinery blades and related flows using an approach similar broadly to that of Kaltenbach and Choi [1] which allows a partial use of the direct Fourier technique for pressure solution. Taking the divergence of equation (1), one obtains the general version of the familiar pressure Poisson equation:

$$\partial_i(Jg^{ij}\partial_j p) = R \,, \tag{5}$$

where R is the divergence of the provisional mass flux field Ju^i.

The equation can now be discrete Fourier transformed in z (a very rapid computational task) to obtain a set of decoupled equations,

$$\frac{\partial}{\partial x}Jg^{11}\frac{\partial \tilde{p}}{\partial x} + \frac{\partial}{\partial x}Jg^{12}\frac{\partial \tilde{p}}{\partial y} + \frac{\partial}{\partial y}Jg^{21}\frac{\partial \tilde{p}}{\partial x} + \frac{\partial}{\partial y}Jg^{22}\frac{\partial \tilde{p}}{\partial y} - Jk_z^2\tilde{p} = \tilde{R} \,. \tag{6}$$

(This process can be performed even when the z derivatives are replaced by finite-difference formulae, provided z in the simulation is periodic and has an even mesh, though k_z then has a slightly different meaning.)

The 2D equations (6), one for each value of k_z, can be solved very fast even when the geometry is complex. Non-zero values of k_z increase the diagonal dominance of the system of equations, resulting in very rapid convergence of any iterative scheme employed regardless of the type of discretisation used for the x and y derivatives. The small number of low-k_z equations which converge too slowly are speeded up using acceleration techniques such as multigrid [4]. By this means, it is possible to obtain pressure solution times for LES in 2D complex geometries that are almost as fast in some cases (though not as accurate) as the direct solvers available in very simple geometries.

Equation (6) contains cross-derivative terms which generally affect the diagonal dominance of the matrices and slow the convergence of iterative solutions. These terms increase in magnitude with the skewness of the mesh (they are absent altogether for orthogonal coordinates). Thus highly skewed meshes should be avoided for the sake of efficiency. Nevertheless we expect the use of a Fourier technique to yield performance enhancements in the pressure solution compared to a fully 3D solver of a least a factor of 5 and sometimes up to 60.

4 Dynamic subgrid-scale procedure

A dynamic subgrid-scale procedure is employed in our simulations since the flow is lmainra, transitional and finally fully turbulent. A dynamic model is a method of accounting for the unresolved motions and their effect on a large-eddy simulation that uses the information available in the simulation itself maximally. We can think of a large-eddy simulation as accurately representing filtered velocity fields after a large-scale filter has been applied to the true velocity fields. When applied to the Navier-Stokes equations, the filter, represented by an overbar, results in equations that look superficially very like the time-averaged (Cartesian) Navier-Stokes equations:

$$\frac{\partial \overline{u}_i}{\partial t} = -\frac{1}{\rho}\frac{\partial \overline{p}}{\partial x_i} - \frac{\partial(\overline{u_i u_j})}{\partial x_j} + \frac{\partial}{\partial x_j}\nu\left(\frac{\partial \overline{u}_i}{\partial x_j} + \frac{\partial \overline{u}_j}{\partial x_i}\right) \tag{7}$$

The term $\overline{u_i u_j}$ cannot be computed, and the difference between it and the part that can be computed, $\overline{u}_i\overline{u}_j$, is the subgrid Reynolds stress τ_{ij}, analogous to the familiar Reynolds stress occuring in the time-average Navier-Stokes equations.

The subgrid Reynolds stress represents the effects of the subgrid motions on the resolved fields of the LES. In contrast to the standard Reynolds stress whose length and velocity scales are those of the entire turbulent flow field, the length scale and velocity scale associated with the subgrid Reynolds stress can be deduced simply and on a local basis from the mesh and the resolved

velocity field of the simulation. The length scale is derived from the local mesh (Δ) and the velocity scale is dictated by the small-scale motions on the mesh, roughly equivalent to the largest sub-grid velocities.

The earliest estimate for the velocity scale, based on the local strain rate scalar s, due to Smagorinsky [5], was $s\Delta$. He went on to combine these scales into the simple gradient diffusion model:

$$\tau_{ij} - \delta_{ij}\tau_{kk}/3 = \nu_s s_{ij} \tag{8}$$

$$\nu_s = C\Delta^2 s \tag{9}$$

$$s = \sqrt{2 s_{ij} s_{ij}} \tag{10}$$

C is predicted theoretically from the Kolmogorov spectrum in homogeneous isotropic turbulence [6] to be 0.17^2.

This very simple model proved surprisingly successful for several decades. The model in fact has clear shortcomings. Tests of its predictions against directly simulated flow fields show that the correlation between the tensors in equation (8) is low. In shear flows, particularly wall-bounded flows, the model is far too strong and the value of C has to be decreased in a pragmatic way; the reasons for this are now quite well understood.

The dynamic procedure is a new approach in which the value of C, instead of being adjusted artificially based on the experience of the simulator, is deduced from the LES itself [7]. This allows the value of C to respond to local flow conditions, varying in time and space. A base subgrid-scale model such as Smagorinsky is needed first. We then consider what would happen if the same LES flow field were simulated on a coarser mesh, effectively filtering the velocity field on a sacle larger than that actually used for the LES. This coarser filter, called the test filter, is usually chosen to be twice the size of the mesh. The result of applying the test filter (indicated by a caret) to the simulated flow fields is the twice-filtered Navier-Stokes equations:

$$\frac{\partial \hat{\bar{u}}_i}{\partial t} = -\frac{1}{\rho}\frac{\partial \hat{\bar{p}}}{\partial x_i} - \frac{\partial(\widehat{\bar{u}_i \bar{u}_j})}{\partial x_j} + \frac{\partial}{\partial x_j}(\nu + \nu_s)\left(\frac{\partial \hat{\bar{u}}_i}{\partial x_j} + \frac{\partial \hat{\bar{u}}_j}{\partial x_i}\right) \tag{11}$$

Once more the filtered non-linear term is modelled, but in this case the difference

$$T^{ij} = \widehat{\bar{u}_i \bar{u}_j} - \hat{\bar{u}}_i \hat{\bar{u}}_j \tag{12}$$

is called the subtest-scale stress.

The dynamic procedure is based on the assumption that the subgrid stress and subtest stress can be modelled in a formally similar manner, by applying the basis model at both filter scales, Δ and 2Δ:

$$\tau_{ij} - \delta_{ij}\tau_{kk}/3 = C\Delta^2 \bar{s}\bar{s}_{ij} \tag{13}$$

$$T_{ij} - \delta_{ij}T_{kk}/3 = C(2\Delta)^2 \hat{\bar{s}}\hat{\bar{s}}_{ij}\,. \tag{14}$$

Germano pointed out an exact identity relating the traceless part of the test-to-grid transfer stress, which is computable in the simulation, to the difference

between the two modelled stresses, the subtest-scale and the subgrid-scale stress:

$$L_{ij} \equiv \widehat{\overline{u}_i \overline{u}_j} - \hat{\overline{u}}_i \hat{\overline{u}}_j \tag{15}$$

$$L'_{ij} \equiv L_{ij} - \delta_{ij} L^{kk}/3 = T_{ij} - \delta_{ij} T_{kk}/3 - (\tau_{ij} - \delta_{ij}\tau_{kk}/3) \equiv C M_{ij} \,, \tag{16}$$

The models for T_{ij} and τ_{ij} from equations (13) and (14) are substituted into (16) to define the tensor M_{ij}. Thus we deduce that C must be

$$C = L'_{ij}/M_{ij} \,, \tag{17}$$

yielding five separate equations for C since five components of each tensor on the right hand side are independent (the tensors being symmetric and traceless).

The least-squares estimate of the optimal solution for C is [8]

$$C = \frac{< L'_{ij} M_{ij} >}{< M_{kl} M_{kl} >} \,, \tag{18}$$

where the angle brackets represent an average over the homogeneous direction z in the flow in which we do not wish the dynamic procedure to generate local variation of C. The resulting C is a function of time and the inhomogeneous coordinates x and y.

The dynamic procedure has been presented above in Cartesian coordinates for the sake of simplicity, but its derivation can be carried out in general curvilinear coordinates by exact analogy and without difficulty. The result is that we can deduce a dynamic subgrid coefficient C as

$$C = \frac{< L'^{ij} g_{ik} g_{jl} M^{kl} >}{< M^{kl} g_{ik} g_{jl} M^{kl} >} \,, \tag{19}$$

where L'^{ij} is the traceless part of

$$\widehat{\overline{u}^i \overline{u}^j} - \hat{\overline{u}}^i \hat{\overline{u}}^j \tag{20}$$

and M^{kl} is similarly the contravariant counterpart of M_{kl} arising from the difference between test- and subgrid-scale modelled stresses in general coordinates. A question does arise regarding the variation of the filter scale on a curvilinear mesh, since we treat the uniform mesh in the transformed plane as defining the filter at both grid and test levels. Clearly this does not take account in any way of the change of scale of the mesh in physical space, which will affect the turbulence evolution.

The practical computation of C from equation (19) is considerably more complex than in the Cartesian case (18) owing to the presence of the metric tensor coupling the various components. A simple alternative that we have utilised for the simulation whose results are given below is to return to equation (17), or rather its covariant equivalent

$$C = L'^{ij}/M^{ij} \,, \tag{21}$$

and select one of the five equations to define C. This is justified in the case of transition over a leading edge where there is a clear principal strain rate and component of the subgrid Reynolds stress, namely the 12 component,

$$C = L'^{12}/M^{12}\,. \tag{22}$$

The least squares form involving the sum of all six components of the stresses is dominated by the 12 component in this case, so the simplification (22) leads to almost the same distribution of values of C. Of course there is also considerable saving in cost by using the dynamic procedure in this form, without detectable change in the quality of the results. The dynamic computation of C involving filtering on the test scale is still quite expensive and is carried out not at every time step but every ten steps, generating a distribution of C that is used for the following ten steps.

In the simulation of the transitional flow described below, the value of C increases from zero as the flow becomes unstable and reaches normal LES levels when the flow becomes fully turbulent. In fact both M^{ij} and L^{ij} tend to zero in laminar regions, making equations (21) or (22) poorly conditioned or singular. The algorithm for computing C behaves unpredictably in laminar or nearly laminar regions and must be modified to ensure that C approaches zero in a sensible and controlled manner. We do this by changing equation (22) to

$$C = L'^{12}/(M^{12} + \epsilon)\,. \tag{23}$$

ϵ is a selected small quantity related, for instance, to the global average of M^{12}. Typically ϵ is of the order of 10^{-6} of the values of M^{12} occurring in turbulent regions.

5 . Transition following a curved leading edge

We present results from a simulation of the flow over a flat plate with a semi-circular leading edge, Figure 1. The fully general coordinate system around this geometry is needed since an orthogonal coordinate system will have an inconvenient junction between a cylindrical and a Cartesian mesh region just at the critical point where the curved leading edge joins the flat surface. This is the point at which the laminar flow separates. Any disturbances in this region, including those with a numerical origin, will affect the flow radically and lead to erroneous conclusions. A previous simulation by us [9] used an orthogonal coordinate system and suffered from the problems indicated, including rapid and excessive growth of instabilities in the separated shear layer whose origin could be traced to numerical effects. This does not occur in the simulation with fully general curvilinear coordinates.

The overall geometry is indicated by an instantaneous flow field in Figure 1. The Reynolds number based on the plate thickness d is 3450. The simulation uses 408 (streamwise, wrapped round the leading edge) by 72 (wall-

normal) by 64 (spanwise) meshes and is performed using the techniques outlined in previous sections, including the generalised dynamic subgrid-scale model. The circular inflow boundary and the lateral boundaries are eight leading-edge diameters ($8d$) distant from the surface, corresponding to a blockage ratio of 16. The inflow velocity is constant, U_o, and aligned with the plate. The lateral boundaries are free-slip but impermeable. On the outflow boundaries, $9.5d$ downstream of the leading edge, we apply a convective boundary condition based on the mean streamwise velocity.

The spanwise dimension of the domain is $2d$. Some simulations have been performed using a spanwise dimension of $4d$ without any appreciable change in the behaviour of the flow. In terms of wall units based on the turbulent boundary layer downstream of reattachment, the streawise mesh sizes vary from $\Delta x = 10$ to 30.5, while $\Delta z = 9$ and at the wall $\Delta y = 1$ (the distance from the wall to the first specified value of u and w. The time step used in the simulation is $0.005U_o/d$.

Statistics are gathered by averaging in time once the simulation is in its fully developed state and also over the span direction and on both sides of the plate. The simulation is run for 4000 time steps ($200U_o/d$) to allow the transition and turbulent boundary layer to become established, and the statistics discussed below are then gathered over a further 30000 time steps ($150U_0/d$), with a sample taken every 20 steps (1500 samples).

Insignificant small-scale instability is found around the leading edge, but the stagnation point does move from side to side if the division of the mass flux on either sides of the plate is not constrained. The simulation can become permanently asymmetric with this outflow condition, so we have constrained the mass flux through the outflows to be precisely equal on either side of the plate at every time step, the total flux balancing the inflow.

Figures 2 and 3 show the mean and rms fluctuating parts of the streamwise velocity compared with experiment [10] at three streamwise stations, one in the centre of the bubble ($x/l = 0.44$), one just beyond the mean reattachment position ($x/l = 1.09$ and one a little further downstream ($x/l = 1.64$). Both experiment and data have the same low level of free-stream turbulence ($<$ 0.1%) though in the simulation this weak disturbance is imposed artificially through pseudorandom forcing just upstream of the separation point. The experimental blockage ratio is lower than that in the simulation, leading to a slightly longer bubble length ($2.75d$) than in the simulation (about $2.2d$). The experimental data are therefore compared at corresponding values of x/l, where l is the mean reattachment length. For the same reason all profiles are plotted as functions of y/l.

The agreement of the mean profiles is excellent, apart from the velocity at the edge of the bubble which is higher in the simulation owing to the different blockage ratio. However, in the bubble the simulation shows higher peaks of u' occurring closer to the wall. The experimental data was taken with a single hot-wire probe in the shear layer and the bubble, and has been discarded in

the region where measured rms u' exceeds 30% of the local mean U. The disagreement seen in this region appears to arise from lack of resolution of the transition process in the thin bubble by the LES rather than experimental errors, since the position of the peak fluctuation relative to the mean profile is known to agree for a wide variety of separation bubbles and is in the position found in this experiment also. Otherwise the agreement is excellent.

Note that at the $x/l = 1.64$ station the simulation shows a double peak of u', a new near-wall peak having appeared below the peak that persists downstream of the free shear layer. This effect is not apparent in the experimental data at this station. It would indicate that two regions exist: a wake-like disturbance downstream of the bubble which is partially separated from the near wall production region; further evidence of this double layer structure and its origin will be presented below.

Figure 4 shows the vertical (v') fluctutation, for which experimental data are not available. In figure 5 we have the mean principal shear dU/dy, to illustrate the position of the bubble and the rapid re-establishment of high near-wall shear immediately after reattachment, underneath the separated shear layer. It is important however to bear in mind that these quantities are time means of highly fluctuating instantaneous flows, though the origin of the double layer structure is clear in the two distinct mean shear regions.

We are particularly interested in the product $v'^2 dU/dy$ which is the main contribution to the production of the $u'v'$ stress. This is shown in figure 6, normalised by the product of the maximum v'^2 (occurring here in the separated shear layer) and the maximum dU/dy, which, beyond reattachment, occurs at the wall. Note the slight evidence for the double layer structure at $x/l = 1.64$ in this figure.

Figure 7 shows the principal off-diagonal stress $u'v'$. There is no evidence here for a secondary peak of the stress close to the wall even at $x/l = 1.64$, and in fact the main contribution continues to be from the separation bubble and its wake-like aftermath to the end of the computational domain. However, looking at the main contribution to the u production $u'v'dU/dy$ in Figure 8, we find a powerful near-wall peak has developed since the level of $u'v'$ stress from the outer layer overlaps in a narrow region with the high dU/dy peaking at the wall. This explains the origin, in statistical terms, of the rapid development of a near wall peak in u' beyond reattachment.

In order to increase our understanding of the processes involved in this transition process, we separate two-dimensional and three-dimensional parts of the velocity field at a specific instant in the simulation. Figure 9 shows the mesh in the sub-region we focus on, and Figure 10 colour contours of the streamwise velocity component at an arbitrary z plane. The picture clearly suggests a 3D breakdown of the separated shear layer about two thirds of the way down the bubble, with the asymmetry between the two sides being quite clear, suggesting a symmetry-breaking transition process is under way.

Figures 11 to 14 clarify this. Figure 11 shows span-average streamwise velocity contours at the same instant, revealing that the bubble is indeed two-dimensional for the first two-thirds of its length but that only minor aspects of the breakdown process involve coherent 2D processes, masked here by the strong overall profile of $<u>$. The 2D component of the breakdown process is more clearly apparent in Figure 12 which shows the span-average vertical velocity $<v>$. This picture indicates that weak rolls of fluid are present, predominant wallward motions being interspersed with regions of motion away from the wall. The structures do occur in a region away from the wall, as if forming an assymmetric wake of the separtion region, and form a semi-coherent pattern with irregular streamwise spacing.

The three-dimensional parts of the velocity fields are given as contours in Figure 13 ($u- <u>$) and Figure 14 ($v- <v>$)). The three-dimensional disturbances in u are seen first about half way along the bubble, become established by about $x/l = 0.7$ and are highly significant at and beyond the mean reattachment point. This confirms the general view that 3D breakdown promotes the reattachment and also suggests that the highly variable position of reattchment in time and z is related to the chapotic nature of the 3D breakdown locally. Figure 14 reveals that vertical 3D motions occur later, being first seen just upstream of mean reattachment, and are less pronounced, with an irregular streamwise structure. This is also true for span-wise motions (not shown). The 3D motions however approach the wall more closely than the 2D rolls, and the u and v pictures are related, there being a strong suggestion of the correlation between negative u (yellow-red in Figure 13) and motion away from the wall (blue above the plate and red below in Figue 14). The ingress of of these 3D vertical fluctuations into the very near wall region where the instantaneous shear du/dy is also high supports our view of the mechanism of transition.

We have presented strong evidence for a simple conceptual model of the process of transition in this type of flow from these data. The separation is two-dimensional and laminar. Three-dimensional breakdown occurs in the second half of the bubble, with the growth of 3D vertical motions resulting in turbulent transport leading to reattachment which is highly variable in time and streamwise and spanwise position. The turbulent second half of the bubble gives rise to a qusi-regular asymmetric wake-like disturbance propogating downstream, clearly separate from the wall layer. Three-dimensaional disturbances within this 'wake', however, approach closer to the wall and impinge on the growing shear of the near wall layer, promoting a second transition process that is similar in most respects to bypass transition stimulated by similar levels of free-stream turbulence [11].

It is the relatively small scale of these 3D incursions that allows them to reach in close to the wall and interect with the high shear layer, lifting low speed fluid away from the wall and pushing higher speed fluid towards it. The creation of irregularly spaced streaks (not shown here) in the near wall region

is thought to lead to redistribution of fluctuations through pressure-strain interaction, producing vertical (v) fluctuations and leading to self-sustained turbulence in the boundary layer.

6 Discussion

Wew have presented a numerical simulation of the transition to turbulence occurring through separation bubbles on a plate with a semi-circular leading edge. The boundary layers develop in the densely meshed regions on either side of the plate, and are fully turbulent well before they reach the two outflow boundaries. The layers on either side of the plate are statistically independent, just as they would be in the more complex case of a turbine blade. The flow separates and transition takes place as the separated flow becomes unstable, first in a two-dimensional mode but passing into a three-dimensional breakdown which results in rapid reattachment.

The large-scale instabilities originating in the bubble subsequently disturb the reattached boundary layer. As the mean shear at the wall is re-established, large-scale disturbances in the outer region of the boundary layer coming downstream rather like a wake from the separation bubble stimulate a secondary transition near the wall. The mechanisms at work here appear to be similar to those that operate during bypass transition in the presence of free-stream turbulence [11], [9].

7 Conclusions

Methods for performing large-eddy and direct numerical simulations using general curvilinear coordinates have been described, together with the use of Fourier techniques for efficient pressure solution in this context. We have shown how it is possible to combine iterative methods with discrete Fourier transforms to obtain very acceptable pressure solution times, comparable with those obtained by direct methods in simpler geometries. Results for a transitional flow using general coordinates in two dimensions demonstrate the efficacy of the approach. These methods are currently in use for the simulation of turbine blade flows and will also be used in the LES of aerofoils in future.

Acknowledgements

The authors gratefully acknowledge the support of the UK Engineering and Physical Scinces Rresaerch Council, the Defense Evaluation and Rsearch Agency, and Rolls Royce plc who funded this research. The computations were carried out on a Cray J9-32 at Rutherford-Appleton Laboratory, funded by EPSRC.

References

1. Kaltenbach H. J. and Choi H. (1995) Large-eddy simulation of flow around an airfoil on a structured mesh. Annual Research Briefs 1995, Center for Turbulence Research, Stanford University and NASA Ames, 51–60.
2. Hastings R. C. and Williams B. R. (1987) Studies of the flow field near an NACA 4412 aerofoil at nearly maximum lift. *Aeronautical Journal* **91** 29–44.
3. Voke P. R. Flow past a square cylinder: test case LES2. *Direct and Large-Eddy Simulation II* (ed. Chollet, Voke & Kleiser) (1997) 355–373. See also following papers in the same volume.
4. Zeng S. and Wesseling P. (1994) Multigrid solution of the incompressible Navier-Stokes equations in general coordinates. *SIAM J. Num. Analysis*, **31** (6), 1764–1784.
5. Smagorinsky J. (1963) General circulation experiments with the primitive equations. I. The basic experiment. *Monthly Weather Review*, **91**, 99–164.
6. Lilly D. K. (1966) On the application of the eddy viscosity concept in the inertial sub-range of turbulence. *NCAR manuscript no. 123.* NCAR, Boulder CO.
7. Germano M., Piomelli U., Moin P. and Cabot W.H. (1991) A dynamic subgrid-scale eddy viscosity model. *Phys. Fluids A* **3**, 1760–1765 and 3128.
8. Lilly D. K. (1992) A proposed modification of the Germano subgrid scale closure method. *Phys. Fluids A* **4**, 633–635.
9. Voke P. R., Yang Z. and Savill A. M. (1996) Large-eddy simulation of transition following a leading-edge separation bubble. *Eng. Turb. Model. & Exp. 3* (ed. W. Rodi & G. Bergeles) Elsevier, Amsterdam, 601–610.
10. Coupland J. (1994) Private Communication.
11. Voke P. R. and Yang Z. Y. (1995) Numerical Study of Bypass Transition. *Phys. Fluids*, **7**, 2256–2264.

Figure Captions

Figure1. Instantaneous flow field about the plate with curved leading edge: whole domain. Note the fine mesh in the region of primary interest close to the surface.

Figure 2. Mean flow velocity U at three positions measured from the blend point. Left to right, $x/l = 0.44, 1.09, 1.64$.

Figure 3. RMS streamwise velocity fluctuation u' at $x/l = 0.44, 1.09, 1.64$.

Figure 4. RMS wall-normal velocity fluctuation v' at $x/l = 0.44, 1.09, 1.64$.

Figure 5. Mean principal shear dU/dy at $x/l = 0.44, 1.09, 1.64$.

Figure 6. Stress production term $\overline{v'^2}dU/dy$, normalised by peak $\overline{v'^2}$ and peak dU/dy, at $x/l = 0.44, 1.09, 1.64$.

Figure 7. Principal Reynolds stress $\overline{u'v'}$ at $x/l = 0.44, 1.09, 1.64$.

Figure 8. Fluctuation production term $\overline{u'v'}dU/dy$, normalised by peak $\overline{u'v'}$ and peak dU/dy, at $x/l = 0.44, 1.09, 1.64$.

Figure 9. Mesh in the subdomain depicted in figures 10 to 14.

Figure 10. Contours of streamwise velocity u at a single instant for a selected spanwise plane. Blue, positive; red, negative.

Figure 11. Contours of span-averaged streamwise velocity $<u>$ at a single instant. Blue, positive; red, negative.

Figure 12. Contours of instantaneous span-averaged vertical velocity $<v>$. Blue, positive; red, negative.

Figure 13. Contours of 3-dimensional part of the streamwise velocity field $u- <u>$ at one instant for a selected spanwise plane. Blue, positive; red, negative.

Figure 14. Contours of the 3-dimensional part of the vertical velocity field $v- <v>$ at one instant for a selected spanwise plane. Blue, positive; red, negative.

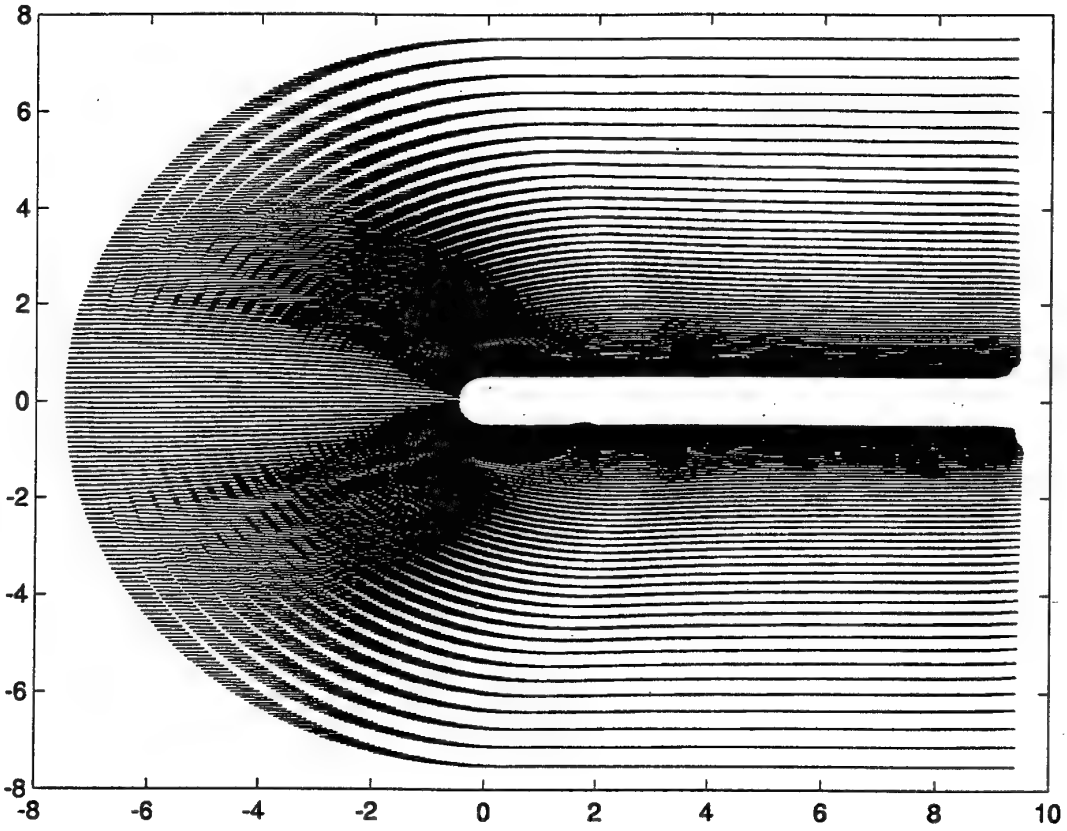

Istanbul 1998: Voke & Yang, Figure 1

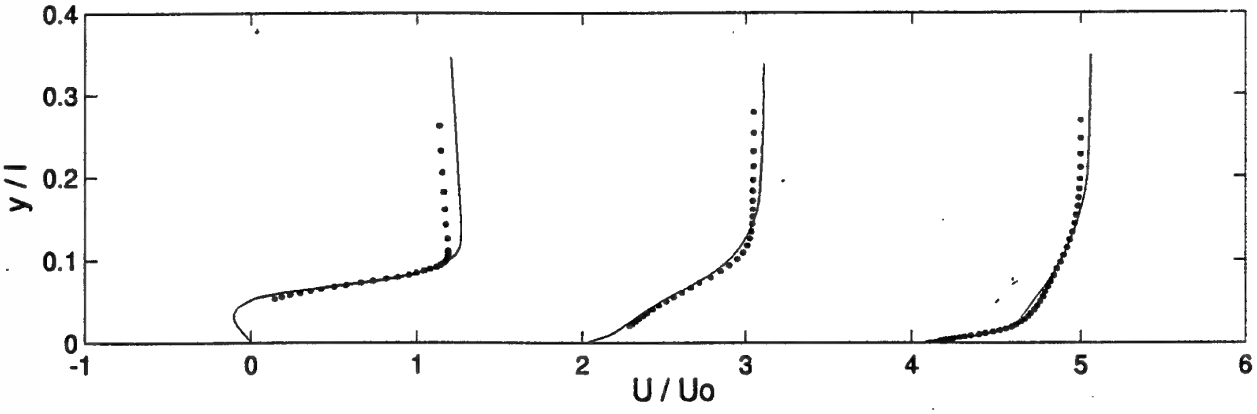

Istanbul 1998: Voke & Yang, Figure 2

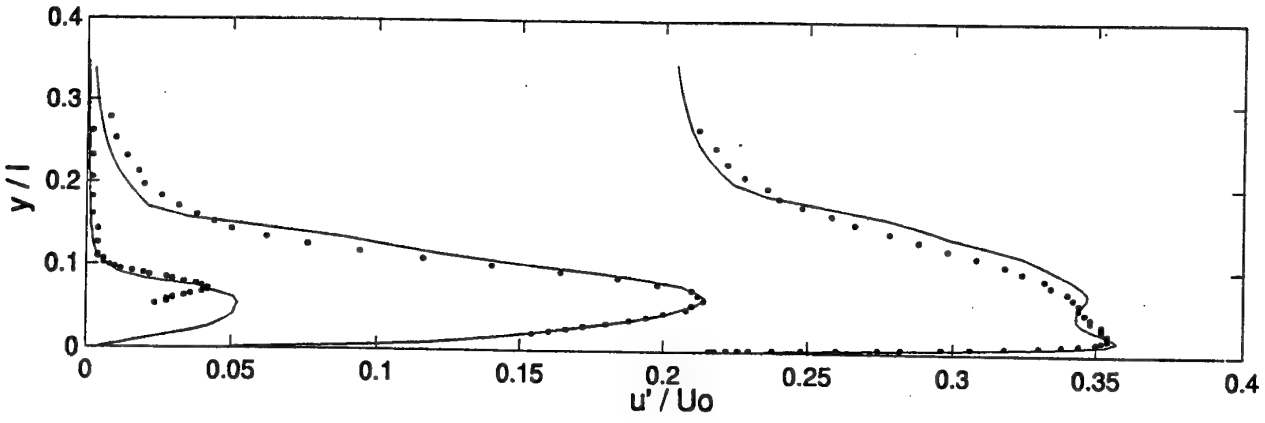

Istanbul 1998: Voke & Yang, Figure 3

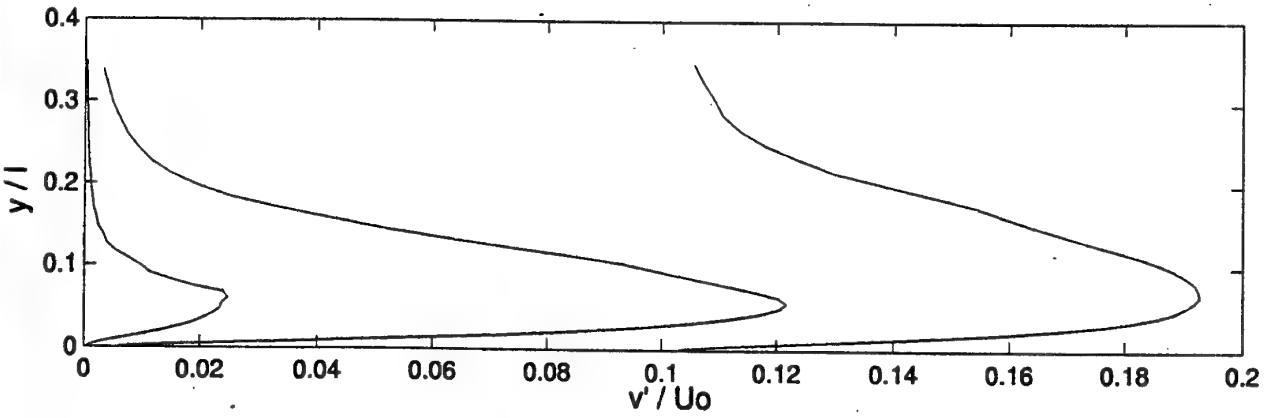

Istanbul 1998: Voke & Yang, Figure 4

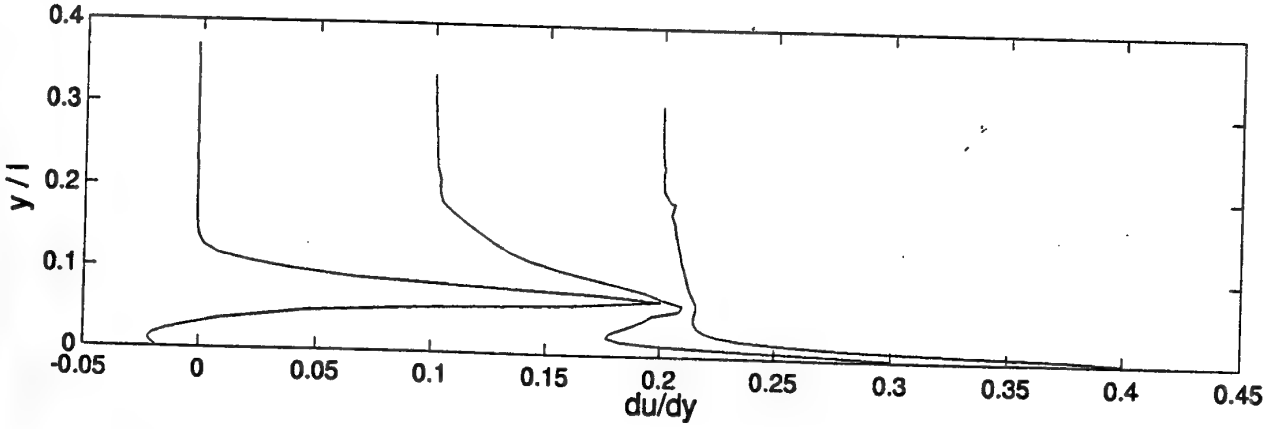

Istanbul 1998: Voke & Yang, Figure 5

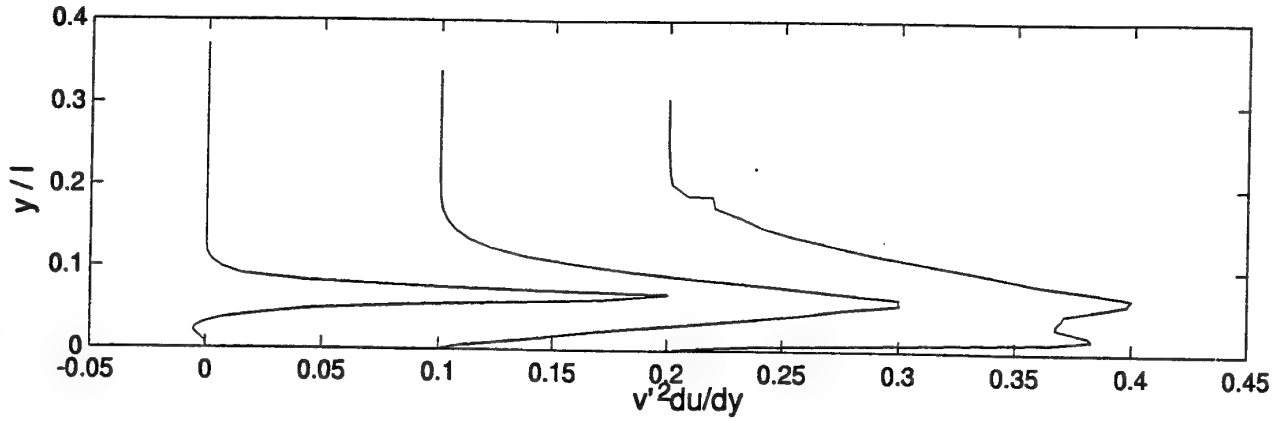

Istanbul 1998: Voke & Yang, Figure 6

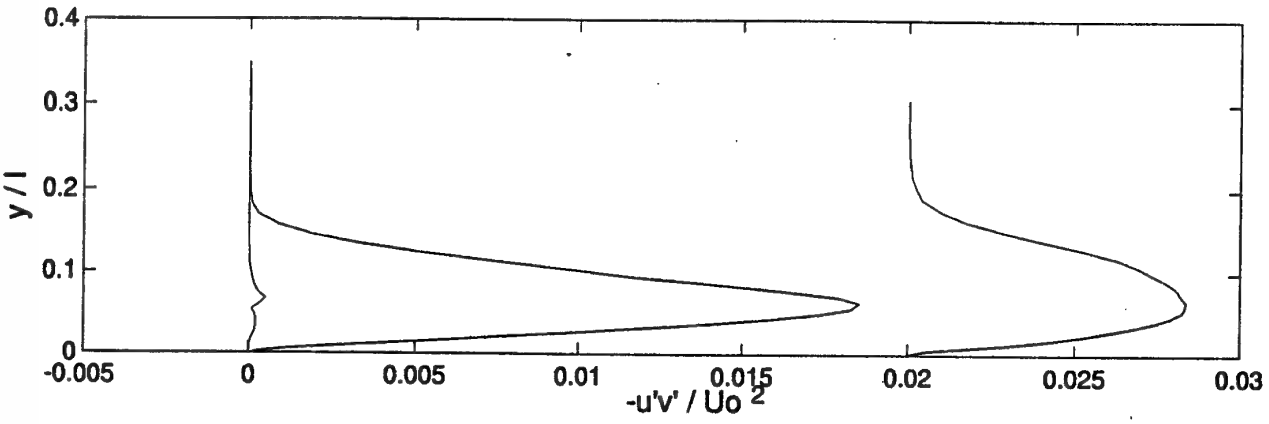

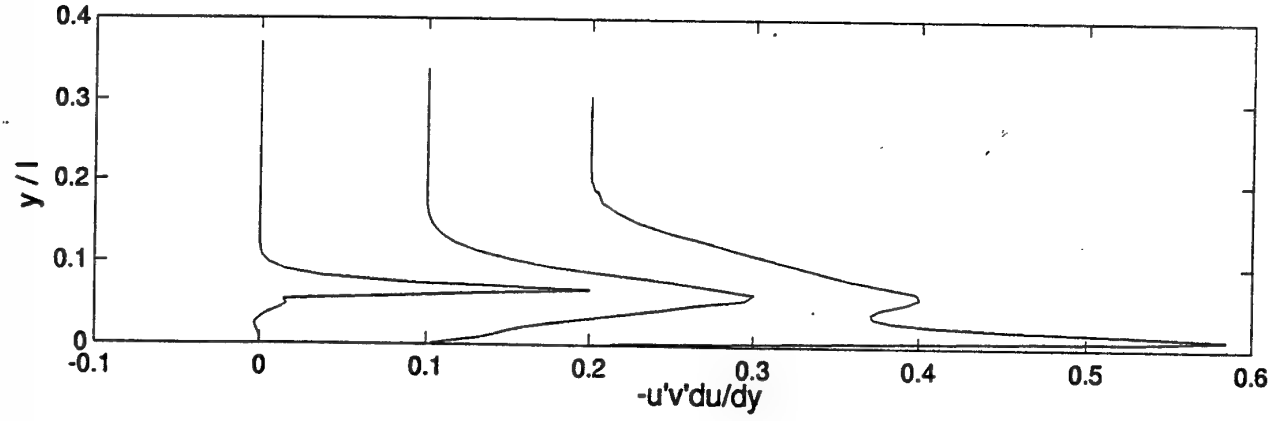

Istanbul 1998: Voke & Yang, Figure 8

Istanbul 1998: Voke & Yang, Figure 9

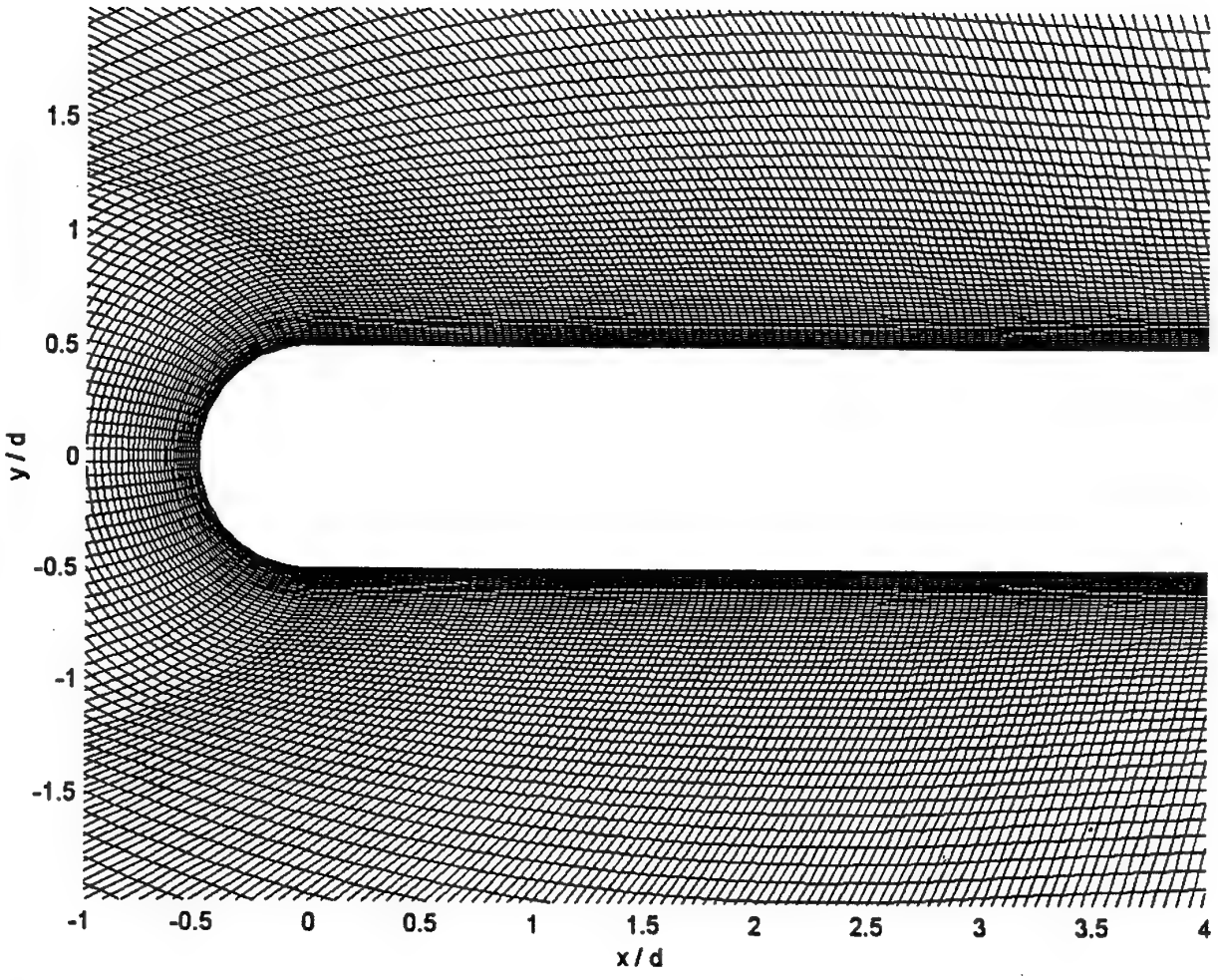

Istanbul 1998: Voke & Yang, Figure 10

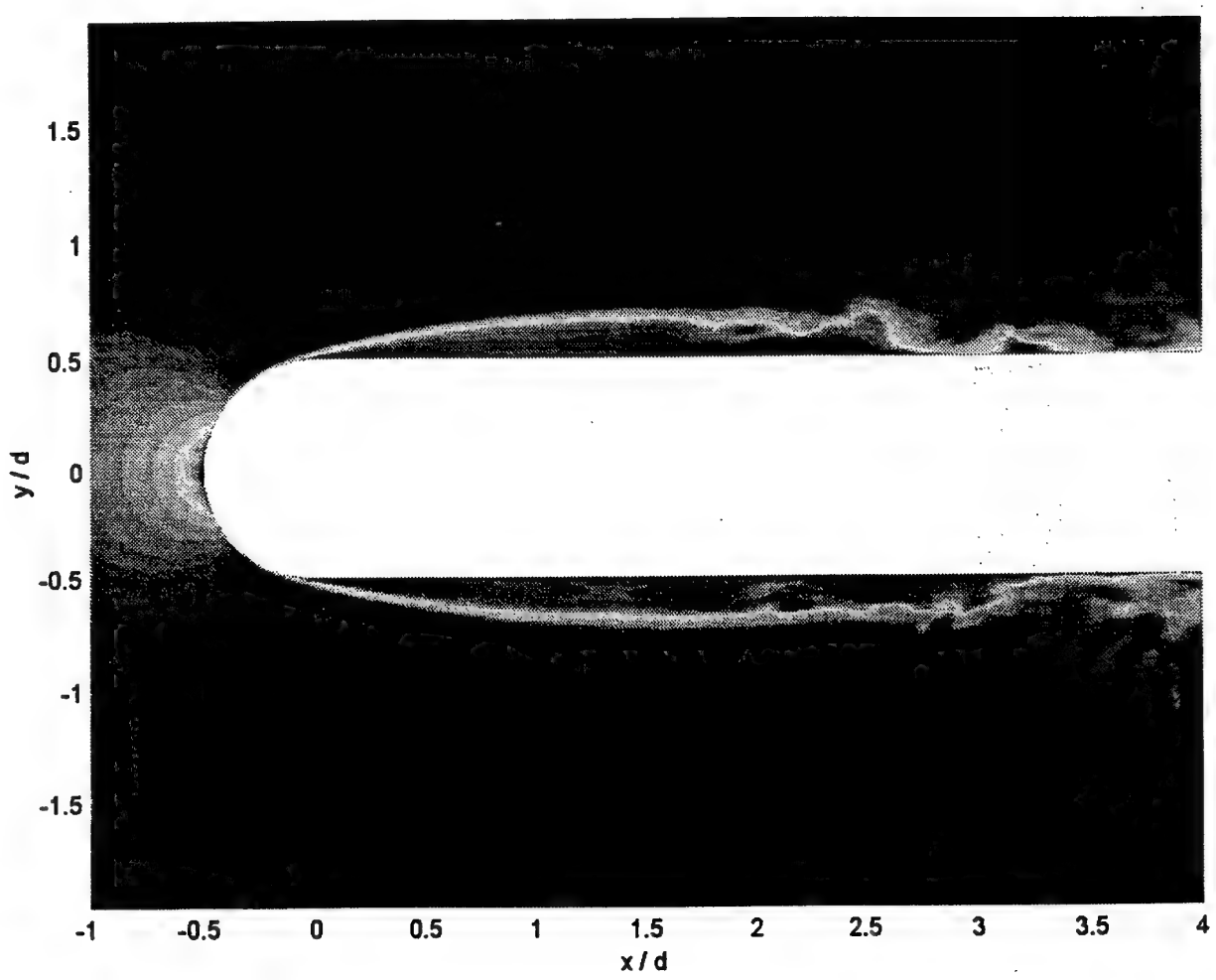

Istanbul 1998: Voke & Yang, Figure 11

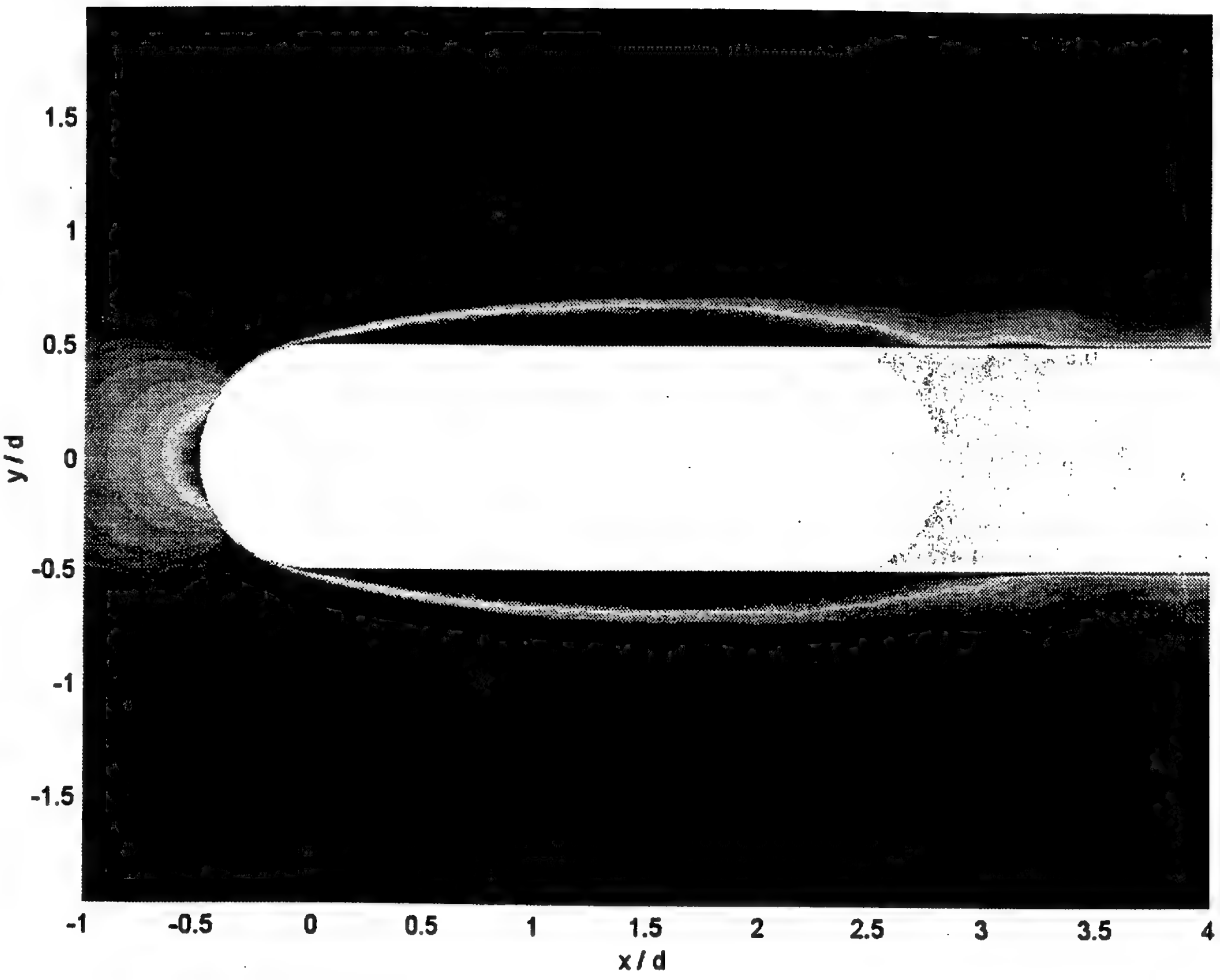

Istanbul 1998: Voke & Yang, Figure 12

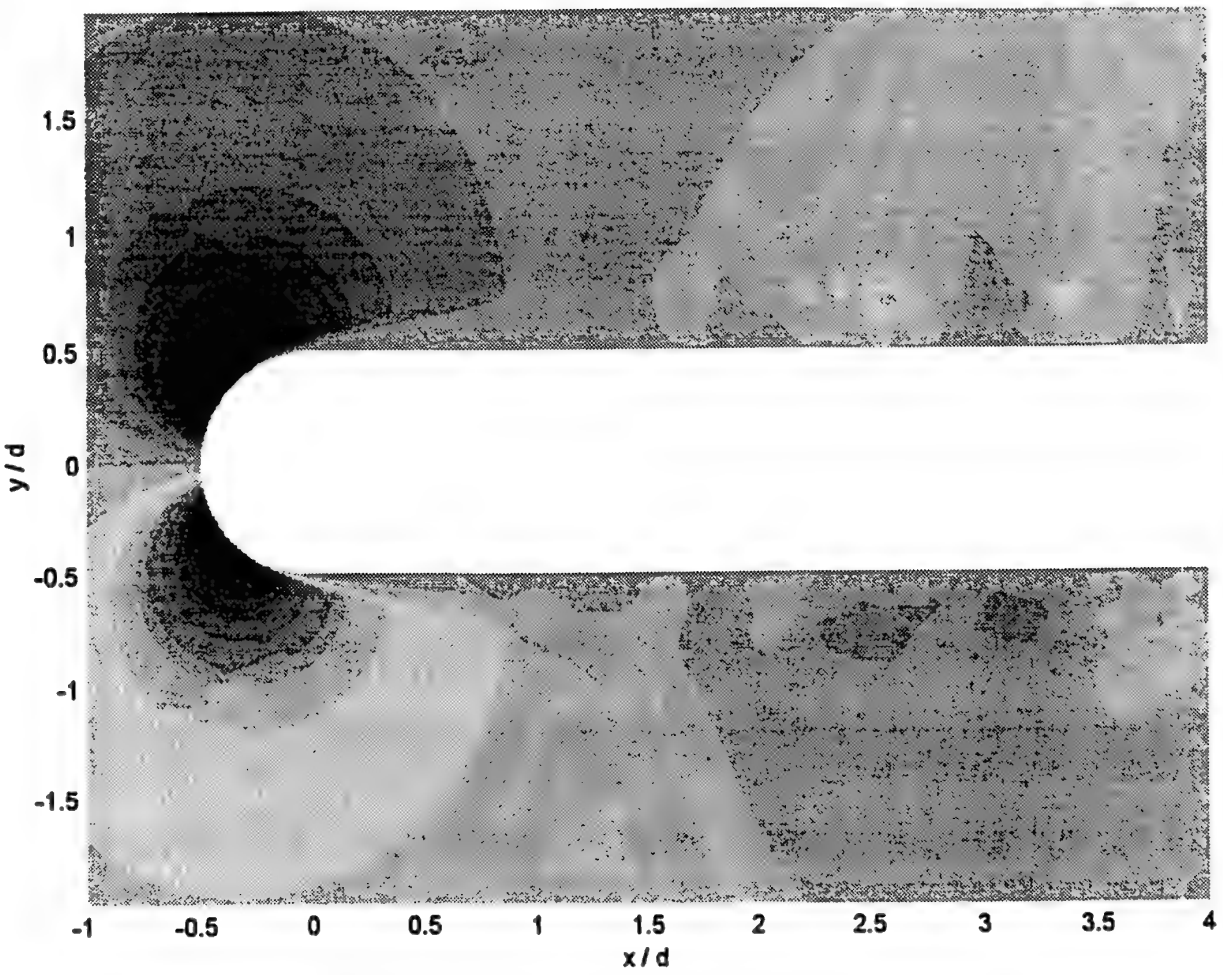

Istanbul 1998: Voke & Yang, Figure 13

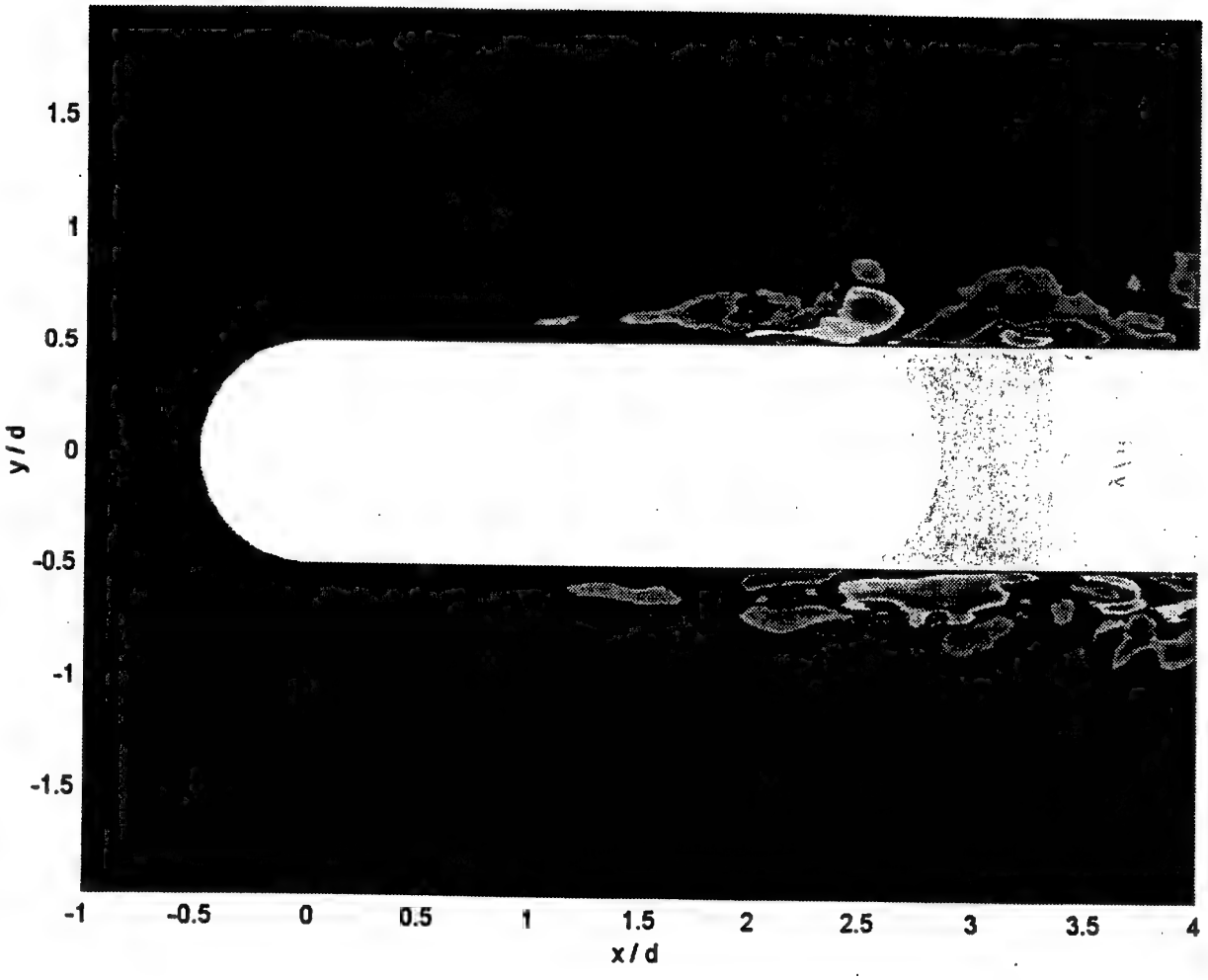

Istanbul 1998: Voke & Yang, Figure 14

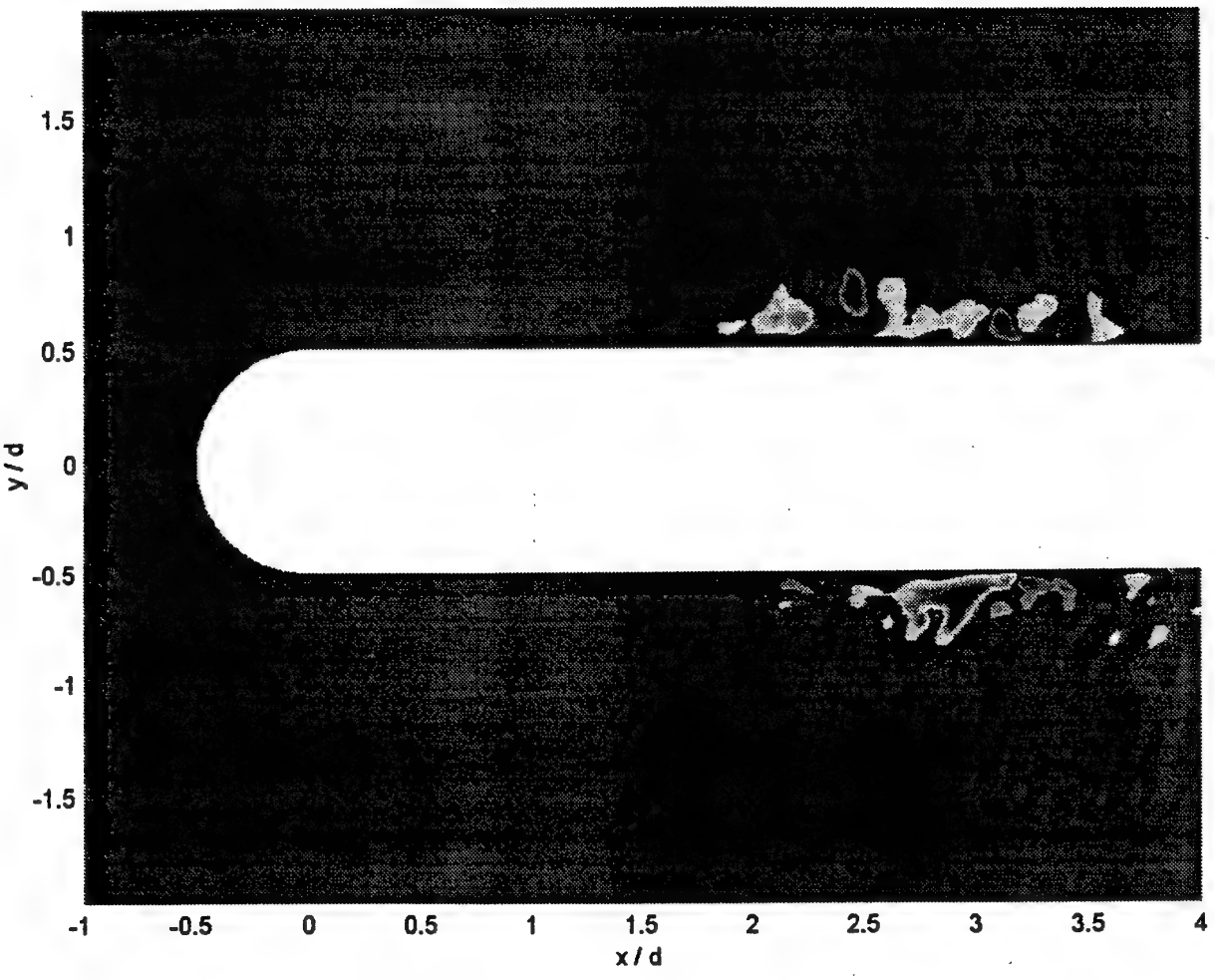

Pushing DNS to the limit

R.W.C.P. Verstappen and A.E.P. Veldman
Department of Mathematics, University of Groningen
P.O.Box 800, 9700 AV Groningen, The Netherlands

Direct Numerical Simulation (DNS) is the most accurate, but also the most expensive, way of computing complex turbulent flows. In view of the computational complexity of DNS, our first concern is to reduce the computational costs as far as we can get. This implies - among others - that the number of grid points has to be kept as small as possible. To use the lowest possible number of grid points, spatial discretization methods for the Navier-Stokes equations need to be strained to their limit.

On nonuniform grids various ways exist to discretize convective and diffusive operators. In [1], we have proposed to apply a high-order finite-volume discretization method that preserves the spectral properties of the convective and diffusive operators, i.e. convection $\leftrightarrow$ skew-symmetric; diffusion $\leftrightarrow$ symmetric positive definite. It is our experience that in this way the error of the convective discretization does not interfere with the diffusion on the smallest length scales. The energy of the discrete system is conserved, if the physical dissipation is turned off. The time-advancement is carried out by an explicit one-leg method. For more details about the numerics, we refer to [1].

We have applied this numerical method to simulate a number of complex flows. The problem considered in this paper is the fully developed flow in a channel, where a matrix of cubes is placed regularly at one wall of the channel. The matrix consists of 25×10 cubes in the streamwise and the spanwise direction, respectively. The width of the channel is $3.4h$, where h denotes the width of a cube. The pitch of the cubes is $4h$, in both the streamwise and the spanwise direction. The Reynolds number (based on the width of the channel and the bulk velocity) is equal to $Re = 13,000$.

Flow measurements by Meinders & Hanjalić [2] have showed that the influence of the in- and outlet can be neglected around the 18th row of cubes (counted from the inlet). Hence, to simulate the flow there, we may confine the computational domain to a sub-channel unit of dimension $4h \times 3.4h \times 4h$ with periodic boundary conditions in the stream- and spanwise direction. Figure 1 displays a sub-channel unit.

The flow through the sub-channel was one of the test cases at the 6th ERCOFTAC/IAHR/COST Workshop on Refined Flow Modeling [3]. Four groups have presented the results of their Reynolds-average Navier-Stokes (RANS) computations. Both

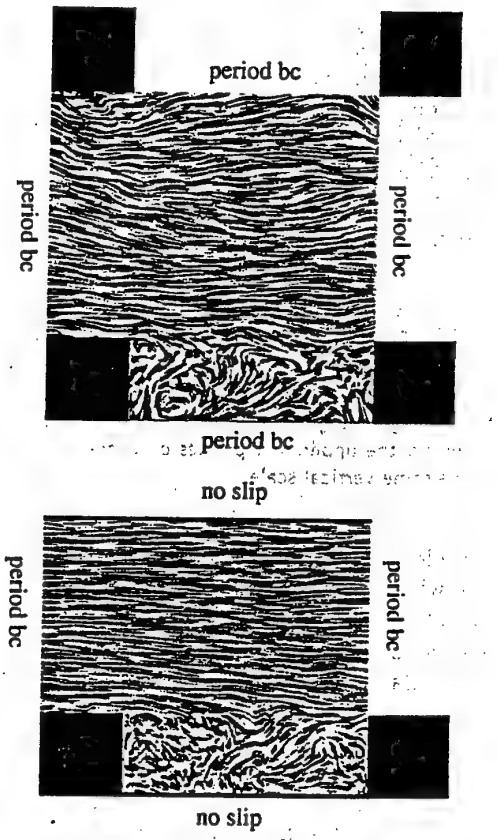

Figure 1: Top- and side-view of a sub-channel unit. Shown is an instantaneous flow field (of the 100^3 simulation) at two planes through the centre of the cubes.

high- and low-Re-number RANS-models were applied. The RANS computation that agreed the best with the available experimental data used a 67 by 72 by 57 grid. We have computed solutions of the incompressible Navier-Stokes equations (without using any turbulence model) on a number of grids. Figure 2 shows a comparison of the mean streamwise velocity of our 60^3 and the 100^3 Navier-Stokes computations, that of the best RANS computation and the experimental data of Meinders & Hanjalić. On a corresponding grid, the mean velocities computed from the Reynolds averaged Navier-Stokes equations agree less with the experimental data than the results of the 60^3 Navièr-Stokes computation. The velocity profiles of the RANS computation are much too smooth. In addition, the maxima of the veloci-

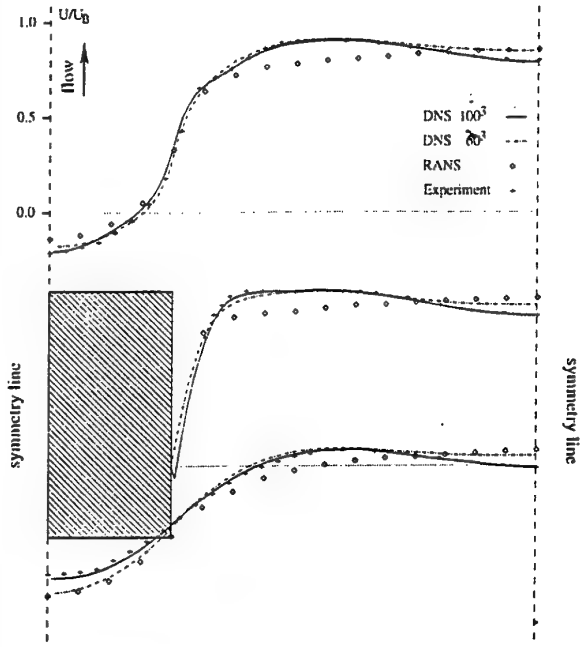

Figure 2: Comparison of the mean streamwise velocity at half cube height. The horizontal corresponds to the spanwise direction. The dashed vertical lines are lines of symmetry. The geometry is drawn to scale. The velocity scale is shown for the uppermost profiles only; the other profiles have the same vertical scale.

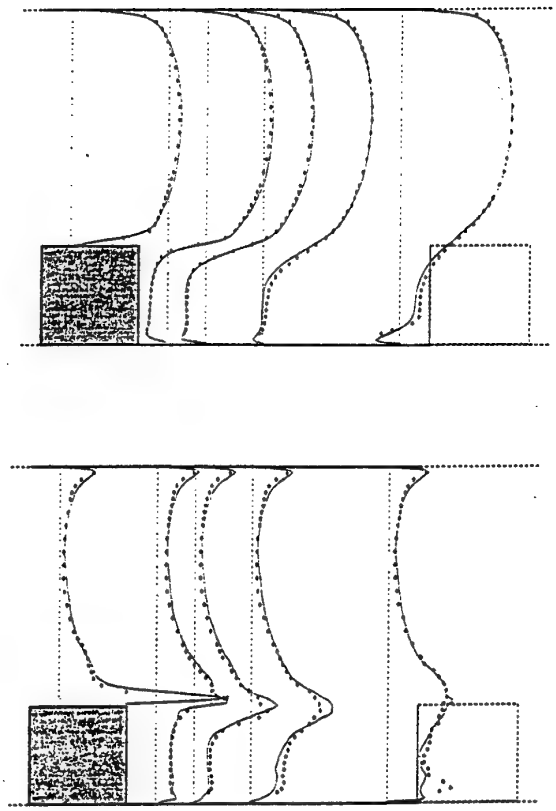

Figure 3: A comparison of first-order statistics (upper picture) and second-order statistics (lower picture) of the DNS with experimental data. Shown are the mean streamwise velocity $\overline{u}$ (upper picture) and $\overline{u'u'}$ (lower picture) in the plane parallel to the streamwise direction that bisects the cubes. The continuous lines correspond to the DNS; the experimental data is depicted by the dots.

ties are located in the symmetry-plane between two cubes, which is in distinct disagreement with the experimental data.

First- and second-order statistics obtained from the 100^3 simulation at the cross section of the channel that bisects a cube are compared to the available experimental data in Figure 3. Here, the averages are computed over 200 (non-dimensional) time units. The profiles of the mean streamwise velocity and the mean-square of the fluctuating streamwise velocity are in good agreement with the experiments, except in the front of a cube, where some discrepancies between the mean-squares of the fluctuating streamwise velocities exist.

So, in conclusion, the 100^3 simulation reproduces the turbulent fluctuations reasonably well, whereas the 60^3 simulation displays some shortcomings. This naturally poses the question: how many grid points are required for a numerical simulation of the flow under consideration, without any turbulence model? To answer this question, we have also performed a 144^3 simulation. With the help of the solutions on three different grids, 60^3, 100^3 and 144^3, the convergence of the numerical approximation upon grid refinement is addressed. Here, the experimental results of Meinders & Hanjalić [2] form the frame of reference. The spectra of the 60^3, 100^3 and 144^3 simulations are compared, to identify the scales of motion that are significant for the first- and second-order statistics. In addition, near the flat wall of the channel, the numerical solutions are also compared to those of the DNS of Kim *et al.* [4] and those of Gilbert & Kleiser [5]. Up to $y^+ \approx 250$, the 100^3 and 144^3 solutions obey the log law accurately, where we have taken 5.5 for the additive constant and 2.5 for the coefficient.

Finally, the budgets for the Reynolds stresses are computed from flow fields of the 144^3 simulation.

References

1. R.W.C.P. Verstappen and A.E.P. Veldman, *J. Engng. Math.* **32** (1997) 143–159.
2. E.M. Meinders, K. Hanjalić, The flow in a matrix of cubical protrusions placed in a fully developed low Re number channel flow, submitted.
3. K. Hanjalić and S. Obi (eds.) Proc. 6th ERCOFTAC/IAHR/COST Workshop on Refined Flow Modeling, Delft University of Technology (1997).
4. J. Kim, P. Moin and R. Moser, *J. Fluid Mech.* **177** (1987) 133–166.
5. N. Gilbert and L. Kleiser, Proc. Turbulent Shear Flows 8 (1991).

International Workshop on
INDUSTRIAL AND ENVIRONMENTAL APPLICATIONS OF DNS AND LES, Istanbul 1998

Large eddy simulation of a transitional flow over a backward facing step with boundary layer manipulations

G. Bärwolff, TU Berlin, FB Mathematik
Germany

We consider a backward facing step channel and we investigate the flow for a Reynolds number of 3000 built with the velocity u_0 of the block inflow profil and the step height H (see fig. 1). The top of the channel is considered as a slip wall and in the lateral direction a periodic behavior is assumed. With the aim of the drag reduction or a decreasing reattachment lenght in the wake of the step acoustic manipulations of the boundary layer in front of the step were performed by experiments and numerical simulations ([1], [2] and [5]). It was found a good agreement of the experimental and numerical results, especially in the case of the reattachment length but also related to the mean velocity field and the rms-profiles. The numerical investigations are done as direct numerical simulations and large eddy simulations. For the direct numerical simulations about 10 million grid points are needed for the spatial discretization. In the case of the large eddy simulations it is possible to work with about 500 thousands of spatial grid points. We use a subgrid scale model of Germano type following Akselvoll/Moin [3]. During the numerical simulations the sufficiency of LES to describe the flow over the backward facing step physical correctly could be shown.
Beside the accoustic boundary layer manipulation over slits with certain frequencies experiments are done with oblique backward facing steps or with moving boundaries to simulate oblique geometries. Based on the experiences of the above discussed numerical simulation of a straight backward facing flow large eddy simulations with moving boundaries are under consideration.
We investigate both a moving upstream boundary in front of the step (lateral velocity v_u) and a moving boundary behind the step in the downstream region of the bottom of the channel (lateral velocity v_d, see fig. 2). The simulations are done for a wide range of lateral boundary velocities, i.e. from $v_{lateral} = 0.5\,u_0$ to $v_{lateral} = 2.0\,u_0$ with u_0 as the inflow profile velocity.

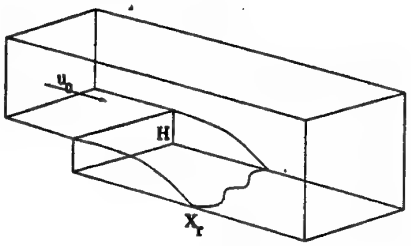

Figure 1: channel situation

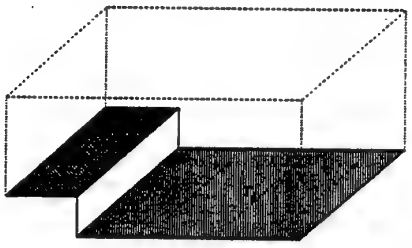

Figure 2: Γ_u and Γ_d as a moving boundaries

In fig. 3 the mean wall shear stress velocity u_τ of the case $v_u = 2\,u_0$ and $v_d = 0$ is shown compared to those of the neutral case $v_u = 0\,u_0$ and $v_d = 0$ in fig. 4.

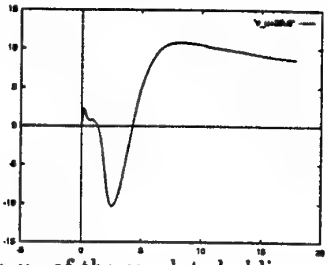

Figure 3: u_τ of the emulated oblique step flow

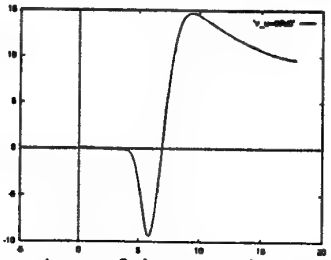

Figure 4: u_τ of the neutral step flow

The numerical simulations are done with a finite volume method on staggered grids which is parallelized on a Cray T3D/T3E using fast Cray-specific shared memory transfer utilities or the platform independend MPI library ([4]). The method is of second order in space and time. The mass conservation per time step was realized by a pressure-velocity iteration method.
The parallelized numerical model (DNS/LES) was validated by comparisons of the numerical DNS/LES results of [5] and the experimental data of [1] and [6]. The following figures 5-8 show the result of comparison for the mean velocities and the rms-values. For these comparisons a neutral, non-manipulated backward facing step flow for the transitional Reynolds number 3000 was considered. The experimental results were produced by LDA-measurements.

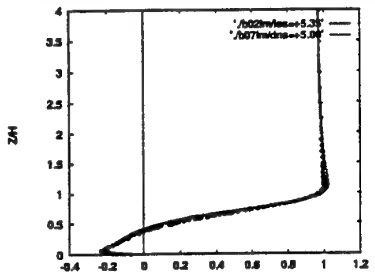

Figure 5: u_{mean} at $x = 5H$

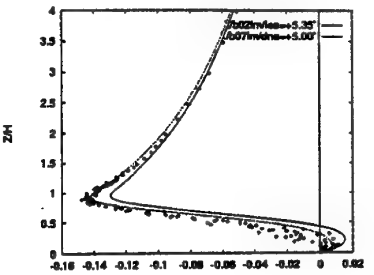

Figure 6: v_{mean} at $x = 5H$

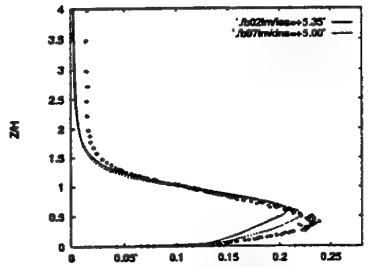

Figure 7: u_{rms} at $x = 5H$

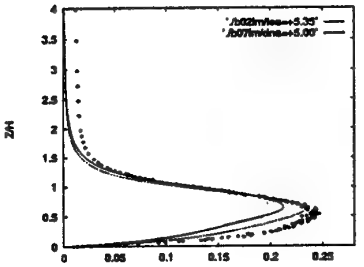

Figure 8: u_{rms} at $x = 5H$

The performance of the parallelized code ($1.3 * 10^7$ gridpoints, 100 timesteps, 25 pressure-velocity iterations) on different mpp systems is shown in the table 1.

system	#procs		time t [sec]	mflops	t_{C90}/t	$S_p = t_{J90(1)}/t$
J90	1		16428	92	0.27	1.00
J90	4		4173	357	1.03	3.94
J90	8		2244	673	1.95	7.32
J90	16		1390	1087	3.15	11.81
C90	1		4380	338	1.00	
system	#procs	$proc_X * proc_Y$	time t [sec]	mflops	t_{C90}/t	$S_p = t_{T3D(32)}/t$
T3D	32	8 * 4	3329	443	1.31	1.00
T3D	64	8 * 8	1671	886	2.62	1.99
T3D	128	16 * 8	871	1700	5.03	3.82
T3D	256	16 *16	437	3387	10.02	7.61

Table 1: *Performance of the FV code on different mpp systems*

The results of the reattachment lenght reduction in the case of the moving upstream boundary in front of the step show a good agreement with the known experimental measurements. The large eddy simulations with the moving boundary behind the step are in the beginning and the first analysis

shows no remarkable influences of the lateral boundary velocity v_d to the position of the reattachment point X_r. A significant reduction of the reattachment lenght was not found. The comparison of the numerical results and the experiments of such a channel flow with a moving channel bottom behind the step, which are done now, will be discussed.

References

[1] Huppertz A. & Janke, G. *Ergebnisse der Strömung hinter einer rückwärtsgewandten Stufe durch dreidimensionale Anregung, private communication 1997/1998*

[2] Bärwolff, G., Wengle, H. & Jeggle, H. *Direct Numer. Solution of Transitional bfs Flow Manipulated by Oscillating Blowing/Suction. H.W. Rodi (ed.): Proc. of the 3rd Int. Symp. on Eng. Turbulence Modelling and Measurements, May 27-29, 1996, Crete, Greece, Elsivier Science, Amsterdam, 1996*

[3] Akselvoll, K. & Moin, P. *Large eddy simulation of turbulent flow over a backward facing step. Report No. TF-63, Stanford University, Febr. 1995*

[4] Bärwolff, G. & Schwandt, H. *A Parallel Domain Decomp. Algorithm in 3D Turbulence Modeling. Proc. of the Int. Conf. on Parallel and Distr. Processing Techn. and Appl. (PDPTA'96), Aug. 8-11, 1996, Sunnyvale/Ca. USA (Ed. H. Arabnia)*

[5] Bärwolff, G. *DNS und LES einer transitionellen Strömung über eine rückwärtsgewandte Stufe mit und ohne Grenzschichtmanipulation, Preprint, FB Mathematik, TU Berlin, 1997*

[6] Huppertz A. *Beeinflussung der Strömung hinter einer rückwärtsgewandten Stufe durch dreidimensionale Anregung, Diplomarbeit, TU Berlin, 1994*

Dr. Günter Bärwolff
Technische Universität Berlin - FB Mathematik
Str. des 17. Juni 136, Sekr. MA 6-3
D-10623 Berlin, Germany

email: baerwolf@math.tu-berlin.de

Workshop on
Industrial and Environmental Applications of Direct and Large Eddy Simulation
5.—7. August 1998 in Istanbul

Aircraft–Wake Vortices in the Atmosphere

Thomas Gerz, Andreas Dörnbrack, Michael Frech, Thomas Hofbauer, Frank Holzäpfel
Institute of Atmospheric Physics
DLR — Oberpfaffenhofen
Germany

People became concerned about a possible impact of aircraft emissions upon the atmosphere and the climate. The concern is based on the facts that the world–wide commercial air traffic grows strongly (and is predicted to grow strongly in the next decade) and it is the only direct anthropogenic emission source at cruising altitudes where the background concentration of the trace gases is low and, hence, an efficacy is possibly large. To assess the impact of aircraft emissions upon the atmospheric state at a global scale it is prerequisite to know how the emissions get mixed and dispersed in the immediate wake of the aircraft, since chemical species transformations and physical phase changes of the exhaust often evolve nonlinearly and, thus, may depend heavily on the mixing properties in the wake. Mixing, in turn, is controlled by the dynamics of the wake flow. The objective of the work, therefore, is to provide a detailed, quantitative, and validated description of the wake dynamics and its effect on mixing and diffusion of the exhaust from the scale of the airplane to the range of atmospheric mesoscale flow. Large–eddy simulations are performed to calculate the wake flow embedded in a stably stratified and turbulent atmosphere. The numerical simulation data will be compared to data collected in-situ and remotely during various measurement campaigns.

The prime result is that the atmospheric eddies disturb the parallel vortex tubes by advection. Once distorted at that scale, the vortex induced velocities amplify the disturbance according to Crow's instability. The vortex tubes link after about 1.5 minutes and form rings; the continuous trail of exhaust is reorganized in a row of single puffs. Without any atmospheric turbulence, the wake does not experience a sinusoidal instability but the parallel vortex tubes approach and start to dissolve after 2 minutes when they touch. The dissolution is triggered by the small-scale turbulent friction owing to the boundary–layer turbulence of the aircraft. The exhaust trail remains aligned along the flight track. For both calm and turbulent situations the entrainment rate drops in the interval between 20 s and 100 s by 2 to 2.5 orders of magnitude and increases again when the vortices collapse.

Another problem rises in view of the expected growth of air traffic: Increasing demands on the capacity and safety of large airports have to be faced, since aircraft wake vortices (WV) may exert a serious danger on following aircraft if the separation between leading and following aircraft is not sufficient. Among others these demands require new ways to develop dynamic spacing criteria for approach and landing. Since at many airports aircraft have to join the glide slope already several miles before landing, the area which has to be controlled is quite large. That is, we need to know where and how long WV can exist along the glide path. Preferably, we would like to identify the atmospheric conditions for which WV do not exert any danger to following aircraft. Therefore the questions whether and under which atmospheric conditions WV can stop their descent or even rise again are of primary interest.

A wake vortex warning system (WVWS) was developed for the airport in Frankfurt in order to run the closely spaced parallel runways separately at appropriate meteorological conditions. The WVWS predicts the propagation and lifespan of wake vortices in a safety area of 80m height based on statistical methods. This particular height of 80m was chosen since measurement campaigns had shown that WS do not reach this height due to the rebound caused by the interaction of wake vortices with the ground. Pilot associations recently argued that also the updrafts of thermals in a convective atmospheric boundary layer (CBL) could cause WS to stall or even to rise again to the glide slope during the final approach. We have performed LES of the evolving CBL where the wake vortices of an aircraft were superimposed on the windfield. The results indicate that WV actually may rise in the CBL when the velocity of the updraft exceeds the induced descent speed of the WV. But at the same time they are strongly deformed by the large–scale velocity field of the CBL. Moreover, the decay of the WV is considerably accelerated due to the increased turbulence levels in the thermals. To quantify these qualitative results a comparison of the rolling moment being exerted on an aircraft crossing the domain on various paths will be presented for the CBL, a weakly turbulent, and a stable atmosphere.

Usually, the pair of aircraft wake vortices sinks by mutual velocity induction. However, close to the ground they may rise again due to the interaction of one vortex with the friction layer of the bottom. It has recently be found that layers of wind shear may have a similar effect. Again, these rising vortices may be hazardous to following aircraft. We will furthermore present LES results on the impact of shear layers (e.g. low–level jets) upon the bouncing properties of wake vortices when they pass through such a layer.

USA: http://www.volpe.dot.gov/wv/

Europe: www.cerfas.fr/wakenet/

DLR: www.pa.op.dlr.de/wirbelschleppe/wake_vortex.html

Abstract for Istanbul Workshop, August 5–7, 1998
Industrial and Environmental Applications
of Direct and Large Eddy Simulation

Reducing Numerical Uncertainty: A Posteriori Finite Element Bounds for Engineering Outputs of General Partial Differential Equations

A. T. Patera, L. Machiels, and J. Peraire
Massachusetts Institute of Technology

patera@mit.edu

in collaboration with
Y. Maday (Paris VI),
J. Sarrate (M.I.T.), J. Teichman (M.I.T.),
M. Paraschiovoiu (U. Toronto), R. M. Lewis (ICASE)

In the simulation–based design process the engineer must make numerous appeals to the underlying numerical simulation in order to calculate the *outputs* — the system performance metrics of interest, such as lift, drag, or contaminant dispersion — for different values of the design variables. The requirements on the numerical approximation are thus twofold: the approximation must be sufficiently coarse — and hence inexpensive — so as to permit repeated evaluation; the approximation must be sufficiently fine so that the numerical prediction of the desired outputs is representative of the true performance of the system.

A posteriori error control offers great promise in reconciling these often conflicting requirements. *A posteriori* analysis is composed of two critical ingredients: an estimation procedure which inexpensively assesses the error in a particular numerical solution; and an adaptive refinement procedure which exploits this error information to optimally improve the numerical solution. The objectives of a *posteriori* error control are twofold: to eliminate numerical uncertainty — arguably the single largest impediment to widespread adoption of simulation–based design; and to improve numerical efficiency — thus permitting much more extensive design exploration. In fact, greater certainty is a prerequisite for greater efficiency: we may consider a less expensive (or even *the* least expensive) discretization only if the associated error can be quantified, and hence constrained and controlled; we are no longer compelled to choose *either* certainty or efficiency — both can

be achieved.

Unfortunately, in all earlier *a posteriori* error analysis techniques, either — in implicit approaches [5,2,1] — the measure of the error is *not related to the actual engineering outputs of interest*, or — in explicit approaches [3,4,16] — the error estimates for the engineering outputs of interest involve *numerous undetermined or uncertain constants or functions*; in both cases, quantitative confirmation — and hence both certainty and efficiency — is seriously compromised, and the relevance to engineering design greatly reduced.

The *a posteriori* error control method that we are developing [10,12,13,8] is certainly indebted to these earlier techniques — in particular, implicit Neumann–subproblem approaches [5,2,1] — for several important conceptual and mathematical ingredients, especially duality and hybridization. However, our method considerably generalizes these techniques, thereby providing a new and critical "enabling technology": the ability to obtain inexpensive, sharp, rigorous, and quantitative ("constant–free") *bounds* for the numerical error in the *engineering outputs of interest*. Our method is thus directly relevant to the design process, and should lay the foundation for systemic application of *a posteriori* error control within the engineering context.

Our initial formulation focused on symmetric coercive problems (e.g., Poisson and Linear Elasticity [10,12,13]), and nonsymmetric coercive problems (e.g., Convection–Diffusion [10,12,8]), as well as certain constrained problems (the Stokes equations [11], central to hydrodynamics). However, we have recently proposed a more general formulation that greatly expands the types of equations and outputs amenable to our approach. In particular, both *noncoercive* and *nonlinear* elliptic [9] (and stabilized hyperbolic [7]) problems can now be addressed, with only a minor loss in certainty relative to the coercive case. More precisely, for noncoercive equations we must require an additional, rather weak, hypothesis related to the relative convergence rates and magnitudes of the L^2 and H^1 errors; strictly speaking, we therefore provide only *asymptotic* bounds, although in practice uniform bounds are almost always obtained.

We have now demonstrated, both theoretically and empirically, that our bound (and associated adaptive refinement) procedure — rigorous, quantitative, and directly relevant to engineering design — can very effectively treat this larger class of noncoercive and nonlinear equations. Problems addressed to date include noncoercive systems arising from frequency–domain treatment of propagation phenomena (the Helmholtz equation [14,15]); gen-

eralized eigenvalue problems [9]; and the Burgers equation [14,7]. In addition, we can now compute bounds not only for the engineering outputs, but also for the sensitivity derivatives of these outputs with respect to selected design variables [6].

Most recently we have extended the formulation to the full steady incompressible Navier–Stokes equations. The theoretical development follows from the Stokes and Burgers treatment, however the difficulties of incompressibility and nonlinearity are compounded, and care must be exercised in order to obtain the desired (asymptotic) bounding property. We present simple but illustrative results for natural convection in an enclosure at low to moderate Grashof number. We conclude with several remarks related to further extension of the technique, for example to the unsteady Navier–Stokes equations.

References

[1] M. Ainsworth and J.T. Oden, *A unified approach to* a posteriori *error estimation using element residual methods*, Numer. Math., **65** (1993), pp. 23-50.

[2] R.E. Bank and A. Weiser, *Some* a posteriori *error estimators for elliptic partial differential equations*, Math. Comp., **44**:170 (1985), pp. 283–301.

[3] R. Becker and R. Rannacher, *Weighted* a posteriori *error control in finite element methods*, IWR Preprint 96–1 (SFB 359), Heidelberg, 1996.

[4] R. Becker and R. Rannacher, *A feedback approach to error control in finite element methods: basic analysis and examples*, IWR Preprint 96–52 (SFB 359), Heidelberg, 1996.

[5] P. Ladeveze and D. Leguillon, *Error estimation procedures in the finite element method and applications*, SIAM J. Numer. Anal., **20** (1983), pp. 485–509.

[6] R.M. Lewis, A.T. Patera, and J. Peraire, A posteriori *finite element bounds for sensitivity derivatives of partial-differential-equation outputs*, Finite Elements in Design, submitted.

[7] L. Machiels, A. T. Patera, J. Peraire, and Y. Maday, *A general framework for finite element* a posteriori *error control: Application to lin-*

ear and nonlinear convection–dominated problems, in Proc ICFD Conf. Num. Meth. for Fluid Dyn., Oxford, England, 31 March - 3 April, 1998.

[8] Y. Maday and A.T. Patera, *Numerical analysis of* a posteriori *finite element bounds for linear–functional outputs*, Mathematical Models and Methods in Applied Science, to appear.

[9] Y. Maday, A. T. Patera, and J. Peraire, *A general formulation for* a posteriori *bounds for output functionals of partial differential equations; application to the eigenvalue problem*, C. R. Acad. Sci. Paris A, to appear.

[10] M. Paraschivoiu and A.T. Patera, *A hierarchical duality approach to bounds for the outputs of partial differential equations*, Comp. Meth. Appl. Mech. Engrg., **158** 1998, pp. 389–407.

[11] M. Paraschivoiu and A.T. Patera, A posteriori *bounds for linear–functional outputs of Crouzeix–Raviart finite element discretizations of the incompressible Stokes problem*, Int. J. Num. Methods Fluids, submitted.

[12] M. Paraschivoiu, J. Peraire, and A.T. Patera, A posteriori *finite element bounds for linear–functional outputs of elliptic partial differential equations*, Comp. Meth. Appl. Mech. Engrg., **150** (1997), pp. 289–312.

[13] J. Peraire and A.T. Patera, *Bounds for linear–functional outputs of coercive partial differential equations: local indicators and adaptive refinement*, in Proceedings of the Workshop on New Advances in Adaptive Computational Methods in Mechanics, Cachan, France, eds. P. Ladeveze and J.T. Oden, Elsevier, 1997.

[14] J. Peraire and A.T. Patera, *Asymptotic* a posteriori *finite element bounds for the outputs of noncoercive problems: the Helmholtz and Burgers equations*, Comp. Meth. Appl. Mech. Engrg., to appear.

[15] J. Sarrate, J. Peraire, and A.T. Patera, A posteriori *finite element bounds for nonlinear outputs of the Helmholtz equation in two space dimensions*, J. Num. Methods in Fluids, to appear.

[16] R. Rannacher and F.-T. Suttmeier, *A feedback approach to error control in finite element methods: application to linear elasticity*, Preprint 96–42 (SFB 359), Heidelberg, 1996.

LES of Incompressible and Subsonic Shear Flows

M. Lesieur

L.E.G.I./INPG-UJF-CNRS
B.P. 53, 38041 Grenoble Cedex09, France

1 Spectral Eddy-Viscosity and Diffusivity

For a recent review on LES, the reader is referred to [1]. Most of large-eddy simulation studies have been developed in physical space. They are associated to a low-pass filter of width Δx, which is applied to the flow so as to eliminate fluctuations in the motions of smaller wavelength. Then, a subgridscale-tensor appears, which is generally evaluated in terms of an eddy-viscosity function, such as Smagorinsky's model. To me, the major drawback of the eddy-viscosity assumption is that it assumes a spectral gap between the resolved and subgrid scales, assumption which is never fulfilled. In this respect, the spectral eddy-viscosity idea is preferable, provided one can work in Fourier space, which applies however only to simple geometries, as will be seen.

We assume that Navier-Stokes is written in Fourier space[1]. Let $\hat{u}_i(\boldsymbol{k},t)$ be the spatial Fourier transforms of the velocity field. We consider the cutoff wave number $k_C = \pi \Delta x^{-1}$, and define a sharp low-pass filter by setting equal to zero the amplitudes at wave vectors $\boldsymbol{k}$ such that $|\boldsymbol{k}| > k_C$. The formalism of spectral eddy viscosity is due to Kraichnan ([3], see also [4]). One writes the evolution equation for the subgrid modes $\boldsymbol{k}$, and associate a spectral eddy viscosity to nonlinear triadic interactions $(\boldsymbol{k},\boldsymbol{p},\boldsymbol{q})$ such that at least p or q is larger than k_C. In fact, this eddy viscosity is determined at the level of the kinetic-energy spectrum evolution equation given by a two-point closure of isotropic turbulence, the EDQNM theory (see [5]). It is found for 3D isotropic turbulence in the case of a Kolmogorov subgridscale spectrum:

$$\nu_t(k|k_C) = 0.441\, C_K{}^{-3/2} X(k/k_C) \left[\frac{E(k_C)}{k_C}\right]^{1/2} \qquad (1)$$

where C_K is the Kolmogorov constant, $E(k_C)$ the kinetic-energy spectrum at k_C, and $X(k/k_C)$ a non-dimensional function equal to 1 up to about $k/k_C = 1/3$, and sharply rising above ("plateau-peak" behaviour). In the same way, an eddy-diffusivity may be introduced for a passive scalar, with the corresponding turbulent Prandtl number. Within the EDQNM theory, both eddy coefficients have a plateau-peak behaviour: it is clear that

[1] At this level, this requires periodicity in the three spatial directions. We will see below how to get rid of this assumption.

the plateau part corresponds to the usual eddy-coefficients assumption when one goes back to physical space, so that the "peak" (Kraichnan called it "cusp") part goes beyond the scale-separation assumption inherent to the classical eddy-viscosity and diffusivity concepts. We have carried out spectral LES of decaying isotropic turbulence[6][7], where a double filtering in Fourier space across k_C and $k'_C = k_C/2$,

is performed. We find that the subgrid energy transfers[2] across k'_C are equal to the subgrid transfers across k_C plus "resolved" subgrid transfers across k'_C corresponding to the low-pass field with respect to k_C. This is, at an energetic level, a sort of Germano's identity[2] in spectral space. These calculations show that the resolved eddy viscosity does possess the EDQNM plateau-peak shape, but not the eddy diffusivity.

Let us show now an adaptation of the plateau-peak model to kinetic-energy spectra $\propto k^{-m}$ for $k > k_C$, when the exponent m is not necessarily equal to 5/3. The spectral eddy viscosity is now

$$\nu_t(k|k_C) = 0.31 C_K^{-3/2} \sqrt{3-m} \; \frac{5-m}{m+1} X(k/k_C) \left[E(k_C)/k_C\right]^{1/2} , \tag{2}$$

for $m \leq 3$. This expression is exact for $k << k_C$ within the EDQNM theory, as shown in [7]. We retain the peak shape through $X(k/k_C)$ in order to be consistant with the Kolmogorov spectrum expression of the eddy viscosity. For $m > 3$, the scaling is no more valid, and the eddy viscosity will be set equal to zero. In the spectral-dynamic model, the exponent m is determined through the LES with the aid of least-squares fits of the kinetic-energy spectrum close to the cutoff, and the turbulent Prandtl number is

$$P_r^t = 0.18(5-m) \tag{3}$$

(see [5]).

We have applied the spectral-dynamic model to the temporal mixing layer in the case of an initial 3D white-noise perturbation, with statistical data concerning velocity, rms velocity fluctuations and Reynolds stresses in very good agreement with the experiments of unforced mixing layers carried out in Stanford.

1.1 Plane Poiseuille Flow

We present now spectral-dynamic model results for a periodic channel. We use a mixed spectral-compact code, the compact scheme being employed in the transverse direction, while pseudo-spectral methods are used in the longitudinal and spanwise directions which are periodic. The channel has a width $2h$, and we define the macroscopic Reynolds number by $R_e = 2hU_m/\nu$, where U_m is the bulk velocity. The kinetic-energy spectrum allowing to determine

of momentum, or scalar

the eddy-viscosity is calculated at each time step by averaging in planes parallels to the walls, and is thus a function of (y,t). We show now a LES at $R_e = 14000$ ($h^+ = 389$). There is a grid refinement close to the wall, in order to simulate accurately the viscous sublayer (first point at $y^+ = 1$). We have compared the calculation with a DNS at $h^+ = 395$ carried out by [8]. Figure 1 shows the mean velocity and the rms velocity components. The agreement is very good, which is a severe challenge for the model. Notice that the LES allows to reduce the computational cost by a factor of the order of 100, which is huge. We stress also that we have applied the spectral-dynamic model to

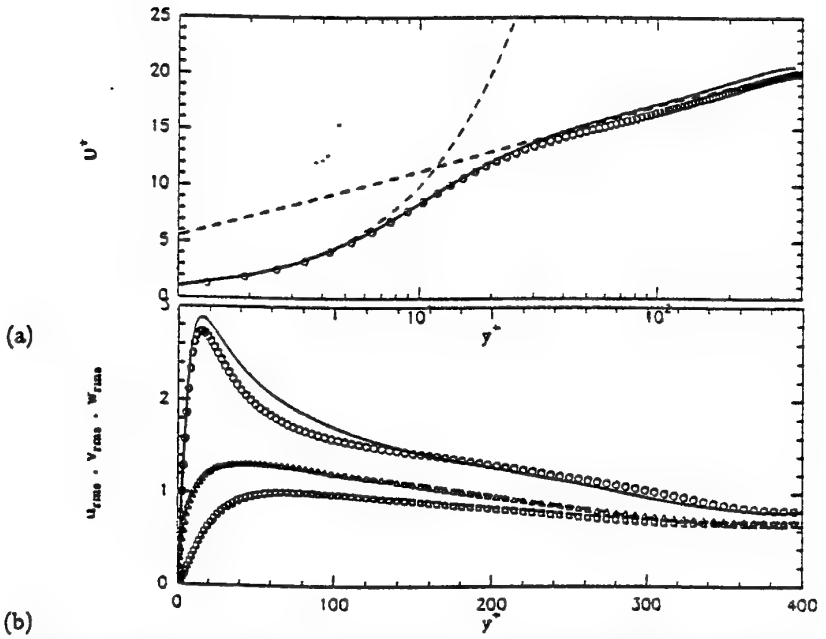

Fig. 1. turbulent channel flow, comparisons of the spectral-dynamic model (straight lines, $h = 389$) with the DNS of Kim ([8], symbols, $h = 395$); a) mean velocity, b) rms velocity components(courtesy E. Lamballais).

the rotating channel, with good results concerning in particular the linear velocity profile on the anticyclonic side.

2 Return to Physical Space

Now, let us consider the EDQNM eddy viscosity (still scaling on $\sqrt{E(k_C)/k_C}$) with no cusp, and adjust the constant by subgrid-energy conservation argu-

ments. We assume that $E(k_C, x)$ is a local kinetic-energy spectrum, calculated in terms of the local second-order velocity structure function of the filtered field

$$F_2(x, \Delta x) = \left\langle \|\overline{u}(x,t) - \overline{u}(x+r,t)\|^2 \right\rangle_{\|r\|=\Delta x} \tag{4}$$

as if the turbulence is three-dimensionally isotropic. This yields for a Kolmogorov spectrum

$$\nu_t^{SF}(x, \Delta x) = 0.105\, C_K^{-3/2}\, \Delta x\, [F_2(x, \Delta x)]^{1/2} \quad . \tag{5}$$

F_2 is calculated with a local statistical average of square-velocity differences between x and the six closest points surrounding x on the computational grid. In some cases, the average may be taken over four points parallel to a given plane. Notice also that if the computational grid is not regular (but still orthogonal), interpolations of (5) have been proposed by [1]. Such a structure-function model (SF) works very well for decaying isotropic turbulence, where it yields a fairly good Kolmogorov spectrum ([7]), better than Smagorinsky's model (with $C_S = 0.2$) and the plateau-peak models (simple or dynamic). However, it does not work for transition in a boundary layer at low Mach (or incompressible) where, like Smagorinsky, it is too dissipative and prevents secondary instabilities of TS waves to develop. To overcome this difficulty, two improved versions of the SF model have been developed. In the selective structure-function model (SSF), the eddy viscosity is set equal to zero if the angle between the local vorticity vector and the average next-neighbour's vorticity is smaller than the value of 20^0, found as the most probable one in equivalent LES of isotropic turbulence. Results concerning the coherent vortices in an incompressible backstep at Reynolds 5100 will be given at the conference. We show that the Kelvin-Helmholtz like vortices shed behind the step undergo helical pairing, and transform into big staggered Λ vortices which impinge the bottom wall and are carried away downstream. We determine the pressure spectra in terms of the Strouhal numbers[3] at various locations downstream of the step. It turns out that three characteristic Strouhal numbers are important: the harmonic 0.23, the subharmonic, and the flapping frequency of the recirculating bubble 0.07.

In the filtered structure-function model (FSF)[10], the filtered field $\bar{u}_i$ is submitted to a high-pass filter in order to get rid of low-frequency oscillations which affect $E_{\overline{u}}(k_C)$ in the SF model. The high-pass filter is a Laplacian discretized by second-order centered finite differences and iterated three times. It is found

$$\nu_t^{FSF}(x, \Delta x) = 0.0014\, C_K^{-3/2}\, \Delta x\, [\tilde{F}_2(x, \Delta x)]^{1/2} \quad . \tag{6}$$

[3] non-dimensionalized by the incoming velocity and the step height

3 Compressible Boundary Layer

We present here some recent results obtained in Grenoble concerning LES of transition to turbulence in a boundary layer above an adiabatic flat plate in an ideal gas at $M_\infty = 0.3$. We have developed a formalism using density-weighted Favre averages[9]. One introduces a "macro-temperature" and a "macro-pressure" which are related by the equation of state

$$\varpi \simeq \overline{\rho} R \vartheta \quad . \tag{7}$$

provided the condition

$$\frac{3\gamma - 5}{6} \gamma M_{sgs}^2 \ll 1$$

is satisfied. For the air, it improves the condition $\gamma M_{sgs}^2 \ll 1$ proposed usually. With the classical eddy assumptions done for the momentum and heat subgrid stresses, it permits to reduce the problem to the resolution of compressible Navier-Stokes equations, where the molecular-diffusion coefficients for momentum and heat are supplemented by incompressible eddy counterparts. Here, the resolution at the wall is $y^+ = 1$ or 2, and the Mach number

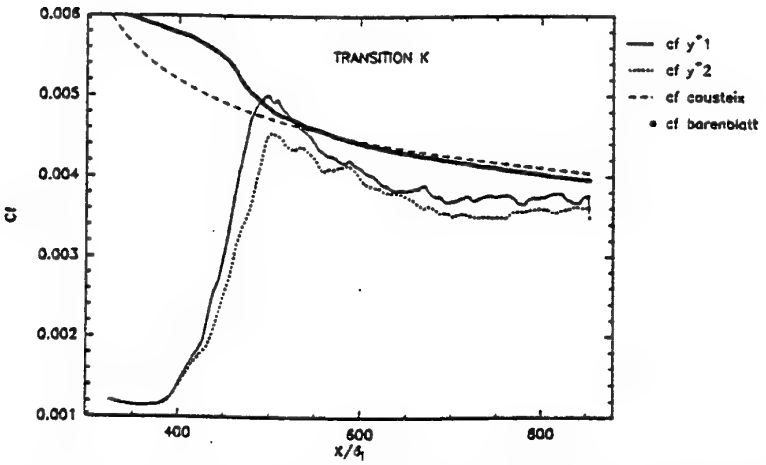

Fig. 2. LES of a spatial boundary layer at Mach 0.3: friction coefficients against downstream distance, compared with theoretical predictions of Cousteix and Barenblatt (courtesy E. Briand).

0.3. Upstream conditions (harmonic K-mode or subharmonic H-mode) are obtained with the aid of nonlinear PSE calculations[11] using the ONERA code[12]. To this upstream state (with still $R_\delta = 1000$), one superposes a 3D white-noise of amplitude 0.2 the amplitude of the PSE perturbation. The simulations involve up to five millions of grid points. Figure 2 shows for the

K-case the downstream evolution of the friction coefficient at the wall, with comparison against the theoretical predictions of Van Driest and Barenblatt. One sees a good agreement of the LES with these predictions, with an improvement with a resolution of $y^+ = 1$. It is even better in the H-case.

3.1 Boundary Layer upon a Groove

We give here results concerning a turbulent boundary layer on a flat plate at $R_\delta \approx 1000$ passing over a square 2D groove. The Mach number is 0.5, and the flow upstream is calculated through an iterative procedure developed by [13]. The cavity has a depth equal to the upstream boundary-layer thickness δ. We have looked at the vorticity modulus map conditioned by

the "Q-criterion"[14], which selects regions where the second invariant of the velocity-gradient tensor is positive. The calculation shows how boundary-layer hairpins shed downstream of the backward step are lifted above the recirculation zone within the cavity, and impinge the upward step to form both smaller-scale turbulence (in a sort of ultraviolet kinetic-energy cascade) and big inclined arch-like vortices which travel downstream of the cavity. One can check also that the characteristic spanwise wavelengths of the velocity streaks decrease after the cavity.

References

1. Lesieur, M. & Métais, O., *Ann. Rev. Fluid Mech.* 28 (1996) 45-82.
2. Germano, M., U. Piomelli, P. Moin & W. Cabot, *Phys. Fluids A.* 3 (1991) 1760-1765.
3. Kraichnan, R.H., *J. Atmos. Sci.* 33 (1976) 1521-1536.
4. Chollet, J.P. & Lesieur, M., *J. Atmos. Sci.* 38 (1981) 2747-2757.
5. Lesieur, M. *Turbulence in fluids, 3rd edition*, Kluwer Academic Publishers (1997).
6. Lesieur, M. & Rogallo, R., *Phys. Fluids A* 1 (1989) 718-722.
7. Métais, O. & Lesieur, M. *J. Fluid Mech.* 239 (1992) 157-194.
8. Antonia, R.A., Teitel, M., Kim, J. & and Browne, L.W.B, *J. Fluid Mech.* 236 (1992) 579–605.
9. Favre, A., *J. Mécanique*, 4 (1965) 361.
10. Ducros, F., Comte, P. & Lesieur, M., *J. Fluid Mech.* 326 (1996) 1-36.
11. Bertolotti, P. & Herbert, T., *Theoret. and Comp. Fluids Dynamics*, 3 (1991) 117-124.
12. Airiau, C., PhD, Toulouse University (1994).
13. Lund, T.S., Wu, X. & Suires, K. D.. *Ann. Res. Briefs*, Stanford (1996) 287-295.
14. Hunt, J., Wray, A. and Moin, P., *CTR Rep. S-88* (1988) 193.

Dynamic DNS of Turbulent Flows: Applications to Flow-Structure Interaction Problems

George Em Karniadakis
Center for Fluid Mechanics
Division of Applied Mathematics
Brown University
http://www.cfm.brown.edu/CRUNCH

Summary

Spectral methods have been used with great success in direct numerical simulations of turbulent flows in simple computational domains. In this talk we will present the next generation of spectral methods on unstructured and polymorphic domains suitable for addressing the geometric complexity of industrial applications. These new methods are hierarchical and are well suited for computational steering and dynamic direct numerical simulation (dDNS). We will present several dDNS examples of both internal and open transitional and turbulent flows to demonstrate this new methodology and compare it with low-order methods.

In particular, we will present a detailed study of flow past a flexible cylinder subject to vortex induced vibrations (VIV). The question of what flow pattern prevails in the wake of a long flexible structure subject to uniform or shear flow is of fundamental importance as it dictates the magnitude of the forces on the structure. What conditions produce a stable standing wave response or a travelling wave response? We have obtained simulation results and models from this ongoing investigation using three-dimensional simulations of flow past a flexible cable. Different initial conditions and different spans of the cable were used to classify the responses. Travelling waves appear in long cables and produce oblique shedding with a wake similar to the two-dimensional von Karman street across the entire span. In contrast, standing waves appear in shorter cables and produce parallel shedding with a wake structure varying continuously across the span, from a von Karman street at the anti-nodes to anti-symmetric shedding at the nodes. Chevron-like shedding is produced in the presence of shear along the cable.

Another important question for VIV is the wake transition process. Transition to turbulence in the wake of a fixed cylinder occurs at Reynolds number between 250 and 400, as has been established by experimental results and our previous simulation studies. However, the transition process changes fundamentally if the cylinder is flexible and vibrates freely. In this numerical study, we considered flow past flexible beams and cables undergoing free oscillations subject to near lockin excitation. We investigated different vibrating conditions, corresponding to varying the bending stiffness (beams), tension (cables) and the mass ratio parameter, in order to determine the new transition mechanisms. In general, cables tend to promote wake transition whereas beams tend to delay transition compared to the fixed cylinder behavior.

Large Eddy Simulation of the flow over a matrix of surface mounted cubes

Fabrice Mathey, Jochen Fröhlich, and Wolfgang Rodi

Institute for Hydromechanics
Kaiserstrasse 12, University of Karlsruhe
D-76128 Karlsruhe, Germany

Abstract. A Large Eddy Simulation of the flow over a matrix of surface mounted cubes is presented. Computations employing different sub-grid scales models and different domain sizes are performed. Mean velocity and Reynolds stresses profiles are evaluated and compared with experiment and with previous single-cube LES computations. The influence of the periodic boundary conditions is discussed by doubling the size of the sub-channel domain considered for the simulation.

1 Introduction

The turbulent flow around bluff bodies is characterized by complex interactions between different phenomena such as boundary layers, shear layers, separation and reattachment. Such flows are relevant for many environmental and industrial applications. Although statistical turbulence models have been applied successfully in many practical computations, the Large Eddy Simulation technique shown proved its better potential in calculating flows characterized by large unsteady vortical structures. In particular when the mixing of a scalar such as temperature is of concern, the unsteady flow has to be determined with high accuracy. It then allows to detect for example local overheating of the surface and may furnish relevant information for the design of cooling devices, burners, etc. In the present study, a Large Eddy Simulation of a flow over an array of surface-mounted cubical obstacles is considered. This flow is an example of a bluff body flow where large scale structures dominate the turbulent transport, and for which detailed experimental results [1] are available.

2 Numerical Method

The Large Eddy Simulation code LESOCC developed at the Institute for Hydromechanics [2,3] is based on a Finite-Volume method for solving the incompressible Navier-Stokes equations on general body-fitted, curvilinear grids (LESOCC = Large Eddy Simulation On Curvilinear Coordinates). A non-staggered, cell-centered grid arrangement is used. Both convective and

viscous fluxes are approximated by central differences of second order accuracy. The temporal discretization consists of an explicit low-storage Runge-Kutta method (second order in time). The conservation of mass is achieved by a standard pressure correction algorithm (SIMPLE). The Poisson equation for the pressure correction variable is solved by the strongly implicit procedure of Stone [4], and in order to avoid decoupling of pressure and velocity on the non-staggered grid the momentum interpolation proposed by Rhie and Chow [5] is applied. The code is highly vectorized and has been validated extensively, also for the case of a single surface mounted cube at two Reynolds numbers [3,6]. Different subgrid-scale models are implemented: the Smagorinsky model with van Driest damping near solid walls, and the dynamic model with the least-squares approach of Lilly. Different wall function models are also implemented but are not employed in the present computations because the Reynolds number is fairly low. Recently the code has been extended to block-structured grids for parallel execution on distributed memory machines.

3 Details of the test-case calculations

An experimental situation is simulated in which a matrix of cubes of height H is placed on one of the walls of a two-dimensional channel of height $3.4H$ as sketched in Figure 1. The Reynolds number based on the height of the channel and the bulk velocity is $Re = 13000$. Due to the large number of equispaced cubes with distance $S = 4H$, the mean flow is periodic with a period equal to $4H$ in the x- and z-direction [1]. A sub-channel of size $4H \times 3.4H \times 4H$ (in x-, y- and z-direction respectively) is considered in the simulation, using periodic boundary conditions in the streamwise and in the spanwise direction.

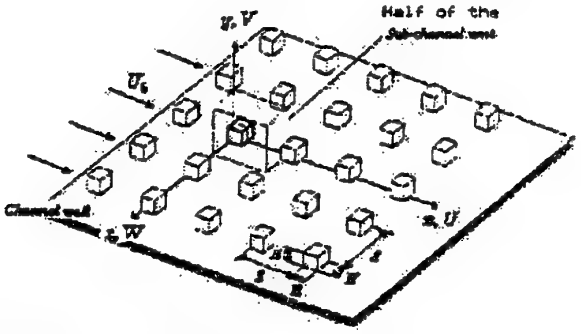

Fig. 1. Sketch of the matrix configuration of cubes on the channel wall (from[1])

To assess the influence of the periodic boundary conditions in the streamwise direction, a computation was performed by doubling the size of this sub-channel domain. All the computations were performed on a stretched grid with $100 \times 100 \times 100$ and $200 \times 100 \times 100$ grid points for the x-, y- and z- direction, for the standard and doubled domain respectively. For the parallel execution, the standard domain was divided into 4 blocks, with 2 blocks in both x- and z-direction, and the second one was divided into 8 blocks. In this paper four different computations are presented. Three computations were performed with the standard domain, employing the Smagorinsky model (SRUN4), the dynamic model (DRUN4), and no sub-grid model (NRUN4). One computation (DRUN8) was performed employing the doubled domain size and the dynamic model.

Table 1. Simulations

RUN Model	Comp. Domain	Grid size
NRUN4	$4H \times 3.4H \times 4H$	No SGS Model
SRUN4	$4H \times 3.4H \times 4H$	Smagorinsky
DRUN4	$4H \times 3.4H \times 4H$	Dynamic
DRUN8	$8H \times 3.4H \times 4H$	Dynamic

4 Results of the simulation

4.1 Description of the general flow structure

From visualization studies and detailed measurements, Meinders et al. [1] devised a sketch of the three-dimensional flow pattern around the cube for one spatial period in the matrix. In this part we will discuss the comparison between these experimental results, the numerical simulation and the previous experiment [3,6] and simulations of the flow around a single cube.

The flow is characterized by the presence of distinct vortex structures in the vicinaty of the obstacles. As shown in Figure 2, the mean flow separates in front of the cube, generating a primary and a secondary vortex. The primary vortex is bent as a horseshoe vortex around the cube into the wake. The flow separates also at the front corners of the cube on the roof and side walls. A large separation region develops behind the cube, with the development of an arch vortex interacting with the horseshoe vortex. This global structure

is close to the one observed for a single cube, however due to the confinement of the flow in the spanwise direction, and due to the interaction in the streamwise periodic direction between neighboring horseshoe type vortices, the reattachment on the roof and on the side walls occurs at a different position. In the matrix case, the reattachment length on the roof and on the side walls is approximately $0.3H$, whereas the single-cube calculations showed no reattachment on the roof. Nevertheless the reattachment length behind the cube is very similar in both the single and matrix cube case (approximately 1.5 cube heights from the leeward face).

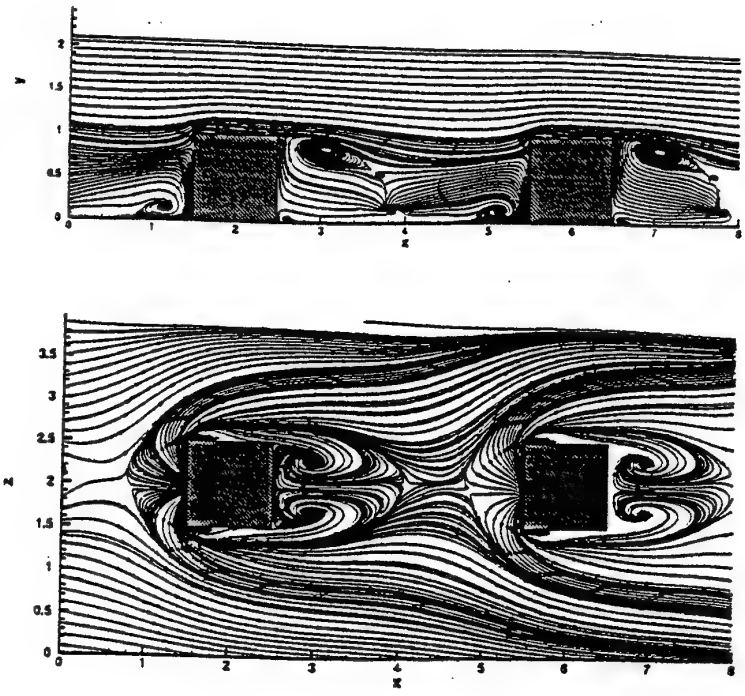

Fig. 2. Streamlines of the time-averaged flow: in the symmetry plane and on the floor of the channel (data from SRUN4 duplicated in the streamwise direction)

4.2 Vortex shedding

As for the single-cube configuration, the experiment showed a predominant fluctuation frequency sideways behind the cube, corresponding to vortex shedding as the flow passes the side walls. These coherent structures were detected from power density spectra of the time series of the spanwise velocity component. The dominant characteristic frequency derived from the location in the spectrum which corresponded to the maximum energy around $27Hz$, leading to a Strouhal number $St = \frac{Hf}{u_B} = 0.109$. The same procedure applied to the Large Eddy Simulation gives a Strouhal number $St = 0.12$ which is close to this value.

4.3 First and second order moments

Detailed comparison between experimental and numerical mean velocities and Reynolds Stresses at different locations were the subject of a recent Workshop [7]. A set of these profiles is given in Figure 3. While streamwise fluctuations $\overline{u'^2}$ become largest in the shear layer and in front of the cube ($x/h = 3.7$), the spanwise fluctuations become maximum close to the reattachment point ($x/h = 2.3$). The overall agreement between the experiment and the simulation is fairly good, despite a slight discrepancy in the wake for the normal Reynolds Stress $\overline{w^2}$ which has been also observed in similar computations [8]. The different sub-grid scale models give almost the same results, with slightly better results for SRUN4. They do not significantly improve the results obtained with NRUN4 (without sub-grid model). The simulation conducted with two cubes included in the computational domain does not show significant difference with the other simulations. Hence interactions between consecutive horseshoe vortices have only very little influence on first and second order moments.

5 Computing times

All computations were performed on the Vector Parallel mainframe Fujitsu VPP 300 installed at the Computer Center of the University of Karlsruhe. It has 16 processors each having a peak performance of 2.2 Gflops and a core memory of 2 Gbytes. Typical CPU times per time step and grid point, and speed-up during parallel computations are given Table 1. The result of a computation using only one block (DRUN1) is also included in the table. The presented results were obtained with a time step $\Delta t = 2.2 \times 10^{-3}$. 15000 steps were computed for the startup phase and statistics were acumulated during 90000 time steps. The whole runs took about 50 hours of CPU time per processors.

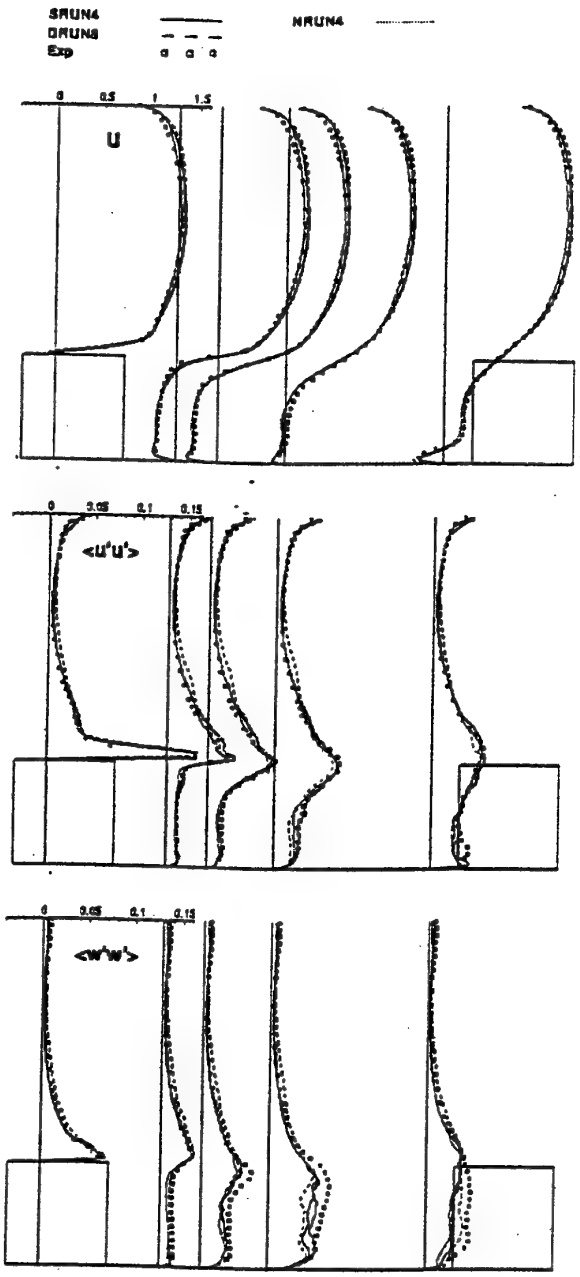

Fig. 3. Mean velocities and Reynolds stress profiles at different positions in the streamwise direction: $x/H = 0.3$; $x/H = 1.3$; $x/H = 1.7$; $x/H = 2.3$; $x/H = 2.7$; $x/H = 3.7$

Table 2. Computation times

RUN	Nb of points	Nb of PE	CPU/time step/grid points	Speed-up
DRUN1	1.10^6	1	$9.\ 10^{-6}$	—
DRUN4	1.10^6	4	$2.39\ 10^{-6}$	3.7
DRUN8	2.10^6	8	$1.21\ 10^{-6}$	7.4

References

1. E.R. Meinders, K. Hanjalic (1998) vortex strucuture and heat transfer in turbulent flow over a wall-mounted matrix of cubes, preprint, Turbulent heat transfer II conference Manchester.
2. M. Breuer, W. Rodi (1994) Large eddy simulation of turbulent flow through a straight square duct and a 180^0 bend. In P.R Voke, R. Kleiser, and J.P. Chollet, editors, *Fluid Mech. and its Appl.*, Volume 26. Kluwer Acad. publ.
3. M. Breuer, W. Rodi (1996) Large eddy simulation of complex turbulent flows of practical interest. In E.H. Hirschel, editor, *Flow simulation with high performance computers II*, Volume 52 of *Notes on Numerical Fluid Mechanics*, pages 258-274. Vieweg, Braunschweig.
4. H.L. Stone, 1968, "Iterative solution of implicit approximations of multidimensional partial differential equations", SIAM *J. on Num. Anal.* Volume 21, pages 530-558.
5. C.M. Rhie, W.L. Chow (1983) A numerical study of the turbulent flow past an isolated airfoil with trailing edge separation. *AIAA Journal*, Volume 21, pages 1225-1532.
6. W. Rodi, J. H. Ferziger, M. Breuer, M. Pourquié, 1997, Status of Large Eddy Simulation: Results of a Workshop. *J. Fluids Eng.*, Volume 119, pages 248-262.
7. F. Mathey, J. Fröhlich, W. Rodi, 7th ERCOFTAC/IAHR Workshop on Refined Turbulence Modelling, UMIST.
8. R.W.C.P. Verstappen, A.E.P. Veldman, 1997, Direct numerical simulation of a flow in a channel with surface mounted cubical obstacles, proceedings of the 6th ERCOFTAC/IAHR/COST Workshop on Refined Flow Modelling, Delft.

Abstract for oral presentation submitted to the Workshop On Industrial and
Environmental Applications of Direct and Large Eddy Simulation
August 5-7, 1998 , Istanbul, Turkey

A study of built-in filter for some eddy viscosity models in Large-Eddy Simulation (LES)

J.-C. MAGNIENT†, P. SAGAUT†, M. DEVILLE‡
email : magnient@onera.fr
† ONERA, 29 av. de la Division Leclerc, 92322 CHÂTILLON cedex, FRANCE
‡ EPFL, CH - 1015 Lausanne

Traditional Large-Eddy Simulation (LES) provides good results on standard benchmark turbulent flows, but engineering applications of more complex geometries are restricted. This is mainly due to the physical hypothesis of homogeneity, isotropy, or local equilibrium of the subgrid scale models, which are hazardous in more realistic configurations. In an attempt to overcome these problems, the recent notion of Very Large-Eddy Simulation (VLES) has been developed. LES relies on an equation filtering theory, actually governed by the modeling terms whose influence on the flow dynamics is not well described. It appears essential to qualify these built-in filters of LES models before performing computations on coarse mesh/high Reynolds number. This work is an assessment of previous theoretical studies on LES filters and kinetic energy spectrums.

In the present study, computations have been carried out on homogeneous isotropic turbulent , and freely decaying flow. The initial random field has a gaussian kinetic energy spectrum centered on a wavenumber $k_0 = 2$. The discretization is $(66)^3$ points in a periodic cube of side 2π.
The PEGASE code, developed at ONERA, solves the full unsteady compressible Navier-Stokes equations using conservative variables (ρ, ρu_i, ρE_T) with a finite difference scheme on structured uniform grids. Convection terms are written in skew-symmetric form and along with diffusion terms, are discretized using a fourth-order centered scheme. Time integration is performed with a third-order low-storage Runge-Kutta scheme. The well-known Smagorinsky model [6], and the Schumann model [5] (a subfilter viscosity depending on the subfilter kinetic energy plus a transport equation based on Prandtl-Kolmogorov equation) have been used. Mach number is chosen 0.1, so compressiblity has no significant effect, and molecular viscosity is null ($Re = \infty$).

A similarity theory of Smagorinsky-type LES, has been proposed by Muschinsky [4]. With $\overline{\Delta}$ being the filter length and Δ the mesh width we define the dimensionless ratio $r = \overline{\Delta}/\Delta$ and the filter cut-off wave number $k_c = \pi/\overline{\Delta}$. Then the turbulent kinetic energy (TKE) spectrum generated by a 'Smagorinsky fluid' may be written:

$$E(k) = K_{0_{LES}}(r)\epsilon^{2/3}k^{-5/3}f_{LES}(k/k_c, r)$$

where ϵ is the dissipation, k the wave number and f_{LES} is a damping function. The filter is mathematically defined in the physical space as a convolution integral similar to a multiplication in the spectral space. Thus, in a filtering viewpoint, we can identify f_{LES} as the square transfer function $\widehat{G}^2$.

The subfilter viscosity of the Smagorinsky model is $\nu_{LES} = (C_S\overline{\Delta})^2|\overline{S}|$ where $|\overline{S}|$ is the modulus of the deformation tensor, the Smagorinsky constant being $C_S = 0.18$. Whatever the form of $E(k)$ it is shown that the dissipation length for a 'Smagorinsky fluid' is $\eta_{LES} = (\nu_{LES}^3/\epsilon)^{1/4} = C_S\overline{\Delta}$. A series of simulations have been carried out using values of r ranged from 1, the usual value in LES, to 4. For a given mesh size this corresponds to a change of the subfilter scale (fig. 1). It is shown that (fig. 2 left):

- We find that for large ratio r the damping function best match the Heisenberg [1] function:

$$f_H(x) = (1 + x^4)^{-4/3}, \quad x = k/k_c$$

and that the length $\overline{\Delta}$ controls the filter cut-off wavenumber. But for $r = 1$, the filter is a sharp cut-off filter and $f_{LES}(x) = H(1 - x)$ (H is the Heaviside function).

Simulations on a $(126)^3$ grid, with different initial conditions, or with a statistically steady forced turbulence provide similar results.

Simulations have also been performed for the Schumann model, an other eddy-viscosity model:

$$\nu_{LES} = C\overline{\Delta}\sqrt{q^2_{SF}}, \quad C = 0.09$$

$$\frac{dq^2_{SF}}{dt} = \tau_{LES}:\overline{\mathbf{S}} - C_1\frac{q^{2\ 3/2}_{SF}}{\overline{\Delta}} + C_2\nabla.(\overline{\Delta}\sqrt{q^2_{SF}}\nabla q^2_{SF}) + \nu\Delta q^2_{SF} \quad C_1 = 1,\ C_2 = 0.1$$

where q^2_{SF} is the subfilter kinetic energy, and τ_{LES} is the Reynolds stress tensor. In this case the damping function has an exponential form (fig.1 right), and the slope of $ln(E(k))$ depends linearly on the ratio r. In terms of dimensionless parameters the damping function is

$$f_{LES} = e^{\alpha(r)+\beta(r)x}, \quad x = k/k_c, \quad \beta(r) = \frac{3.4}{r} - 4.5$$

A similar exponential form of the energy spectrum in the near-dissipation range has been found by previous direct numerical simulations [2].

For the Smagorinsky model the Kolmogorov 'constant' $K_0(r)$ is determined by ploting $E(k)\epsilon^{-2/3}k^{5/3}f^{-1}_{LES}$ (fig.2 left). From these simulations we conclude that:

- $K_{0_{LES}}$ depends on r as predicted [4], considering the given resolution, and the related turbulent Reynolds number $Re_{LES} = (N/\overline{\Delta})^{4/3}$ (fig.2 right).

References

[1] W. HEISENBERG, *Zur statistischen theorie der turbulenz*, Z. Phys., 124 (1948), pp. 628–657.

[2] D. O. MARTINEZ ET AL., *Energy spectrum in the dissipation range of fluid turbulence*, ICASE Report, (May 1996).

[3] P. MASON AND N. CALLEN, *On the magnitude of the subgrid-scale eddy coefficient in large-eddy simulations of turbulent channel flow*, J. Fluid Mech., 162 (1986), pp. 439–462.

[4] A. MUSCHINSKY, *A similarity theory of locally homogeneous and isotropic turbulence generated by a Smagorinsky-type LES*, J. Fluid Mech., 325 (1996), pp. 239–260.

[5] U. SCHUMANN, *Subgrid-scale model for finite difference simulations of turbulent flows in plane channels and annuli*, J. Comp. Phys., 18 (1975), pp. 376–404.

[6] J. SMAGORINSKY, *General circulation experiments with the primitive equations*, Month. Weath. Rev., 93 (1963), pp. 99–165.

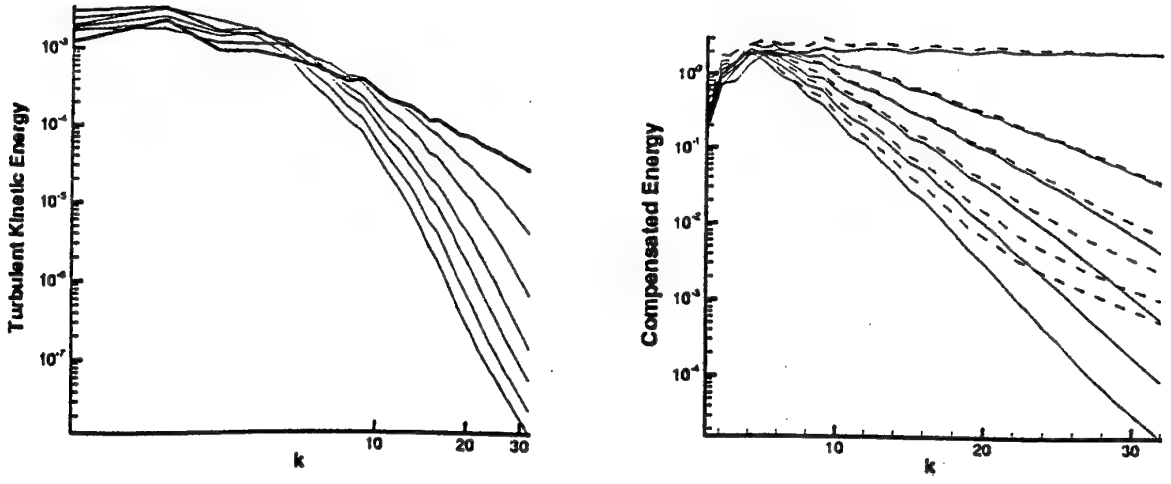

Figure 1: **Left:** TKE spectrum of Smagorinsky-LES for ratio $r = 1$ (bold line), 1.5, 2, 2.5, 3, 3.5, and 4. **Right:** Compensated energy spectrum $E(k)\epsilon^{-2/3}k^{5/3}$ for the Smagorinsky (dashed line) and the Schumann (bold line) models for $r = 1, 2, 2.5, 3, 3.5, 4$.

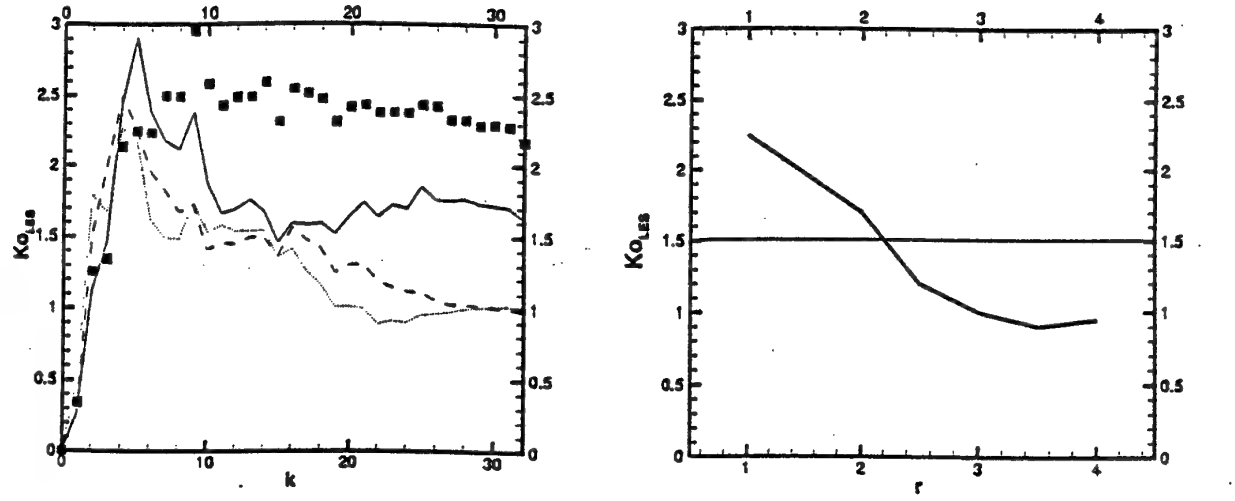

Figure 2: **Left:** Spectrum of $E(k)\epsilon^{-2/3}k^{5/3}f_H^{-1}$ for $r = 2$ (solid line), $r = 3$ (dashes), $r = 4$ (dots), and compensated energy for $r = 1$ (symbols). **Right:** Kolmogorov constant vs. ratio r computed from freely decaying homogeneous and isotropic turbulence of a 'Smagorinsky fluid'.

Workshop on Industrial and Environmental Applications of
Direct and Large Eddy Simulation
August 5–7, 1998, Boğaziçi University, Istanbul, Turkey

LARGE EDDY SIMULATION OF HIGH REYNOLDS NUMBER CIRCULAR CYLINDER FLOW

Michael Breuer
Institute of Fluid Mechanics
University of Erlangen–Nürnberg
D–91058 Erlangen, Germany
breuer@lstm.uni-erlangen.de

ABSTRACT

What are the key issues for successful applications of the large eddy simulation (LES) technique to practically relevant flow problems ?

- First, technical applications are in general concerned with complex geometries which can either be tackled by unstructured grids or by block–structured curvilinear body–fitted grids. All numerical methods based on Cartesian co-ordinates or with specific restrictions such as periodicity in a certain direction (e.g. FFT) fail in this context.

- Second, industrial applications are in most cases high Reynolds number flows. As known from the considerations of Kolmogorov, the ratio of the largest to the smallest length scales (L/l_k) strongly increases with the Reynolds number leading to a broader spectrum of turbulent eddies. Consequently, LES of high Reynolds number flows make special demands with respect to the applied numerical methods and the subgrid scale (SGS) models. Assuming that the size of the computational grid cannot be enlarged according to $Re^{9/4}$, the SGS model has to take a wider spectrum of turbulent vortices into account. Another topic of rising complexity for higher Reynolds numbers is the formulation of appropriate boundary conditions especially at solid walls.

- Third, because it is well-known that LES is not a cheap tool for computing turbulent flows, its application should be restricted to flow problems for which an appropriate description by Reynolds–averaged Navier–Stokes equations (RANS) combined with statistical turbulence models is difficult to achieve. An illustrative example represents the flow past bluff bodies which is in general very complicated, including complex phenomena such as separation, reattachment or vortex shedding.

The long–term objective of the work reported here is to develop a LES technique which is able to simulate high Reynolds number flows of practical relevance, especially bluff body flows. With respect to the considerations above, the developed code ($\mathcal{LESOCC}$ = $\mathcal{L}$arge $\mathcal{E}$ddy $\mathcal{S}$imulation $\mathcal{O}$n $\mathcal{C}$urvilinear $\mathcal{C}$oordinates) is based on a 3–D finite–volume method for arbitrary non–orthogonal and non–staggered grids. Details about the temporal/spatial

discretization and the implemented SGS models (Smagorinsky and dynamic model) can be found in [1, 3, 4, 6]. Recently *LESOCC* has been extended by a multi–block structure strongly improving the possibility to resolve complex geometries. Furthermore the multi–block implementation was also the basis for parallelization by domain decomposition and message passing (MPI). *LESOCC* is highly vectorized (vectorization rate > 99.8%) allowing to perform efficient computations on vector–parallel machines such as NEC SX–4 or Fujitsu VPP 300/700. The simulations presented in this abstract have been performed mainly on a VPP 300 using 4 processors.

Before *LESOCC* was applied to the flow problem of the present investigation, it was extensively tested and verified by LES computations of a variety of different test cases. This included plane channel flow, flows through a straight square duct and a 180° bend [1], flow around a surface–mounted cubic obstacle placed in a plane channel [2, 4, 8] and flow past a long square cylinder [3, 8]. In the course of this validation process detailed investigations on different numerical and modeling aspects influencing the quality of the LES solution have been performed for the flow past a long circular cylinder at a low, subcritical Reynolds number of $Re = 3900$ [5, 6]. In contrast to its square counterpart, this flow configuration requires curvilinear body–fitted grids. Vortex shedding past a circular cylinder is also physically more challenging than the square cylinder test case because the separation point on the surface of the cylinder is not fixed by the geometry. These characteristics of the circular cylinder flow combined with the enormous number of experimental studies on the vortex dynamics of cylinder wakes (see, e.g., review by Williamson [9]) reveals this flow to be an excellent test case for the intended investigations on LES of bluff body aerodynamics. Figure 1 shows the instantaneous von Kármán vortex street past the cylinder visualized by streaklines and the time–averaged streamlines. For this low Reynolds number case ($Re = 3900$) good agreement was found with experimental measurements available. For details see [6].

Concerning the considerations mentioned above, these investigation were now extended to the more challenging test case of circular cylinder flow at $Re = 1.4 * 10^5$ which has been studied experimentally by Cantwell and Coles [7]. At this higher Reynolds number the flow is still subcritical so that transition takes place in the free shear layers. Two different curvilinear, O–type grids have been generated. The first consists of 165 × 165 control volumes (CV) in the cross–sectional plane and 64 computational cells in the spanwise direction. The second is refined in the cross–sectional plane using 325 × 325 CV while the spanwise resolution is kept constant (total of 6.76 Mill. CV). The points are clustered in the vicinity of the cylinder in order to resolve the extremely thin boundary layer at the cylinder and to apply no–slip wall boundary conditions. Additionally, clustering of grid points is performed for the wake region. The entire integration domain has a radial extension of $15D$ in the cross–section (D = cylinder diameter). Three different spanwise extensions (πD, $2D$, D) have been investigated. In this direction of the cylinder periodicity of the flow is assumed. At the inflow plane constant velocity is imposed. A convective boundary condition is used at the outflow boundary. Statistics are compiled over several vortex shedding cycles and in the spanwise direction.

Figure 2 shows first qualitative results of the predicted flow past a circular cylinder at $Re = 1.4 * 10^5$. In comparison with the low Reynolds number case the recirculation region

behind the cylinder (see Fig. 2 (a): time–averaged streamlines) is much smaller which is in good agreement with experiments [7]. Figs. 2 (b) and (c) show contours of the total resolved Reynolds stresses $\overline{u'u'}$ and $\overline{u'v'}$. In the paper these quantities will be compared with the experimental values [7]. Finally, the time histories of the drag and lift coefficient (C_d and C_l) are plotted in Fig. 2 (d). Apart from cyclic oscillations due to the vortex shedding phenomenon and high–frequency turbulent fluctuations, the signals clearly have a low–frequency component which modulates the time histories of C_d and C_l. However, in comparison with the low Reynolds number case (not shown here) the modulation of the signals is much weaker for $Re = 1.4 * 10^5$.

A more detailed description of all aspects which have been investigated and which play a dominant role for the quality of LES predictions will be presented and discussed in the full paper. This will include a quantitative comparison of mean values as well as turbulence quantities. Experimental data available [7] will be used for verifying the computed results and supporting the investigations.

REFERENCES

[1] Breuer, M., Rodi, W.: *Large–Eddy Simulation of Turbulent Flow through a Straight Square Duct and a 180° Bend*, Fluid Mechanics and its Applications, vol. **26**, Direct and Large–Eddy Simulation I, Selected papers from the First ERCOFTAC Workshop on Direct and Large–Eddy Simulation, Guildford, Surrey, U.K., 27–30 March 1994, eds. Voke, Kleiser & Chollet, Kluwer Academic publishers, (1994).

[2] Breuer, M., Lakehal, D., Rodi, W.: *Flow around a Surface Mounted Cubical Obstacle: Comparison of LES and RANS–Results*, IMACS–COST Conference on Computational Fluid Dynamics, Three–Dimensional Complex Flows, Lausanne, Switzerland, Sept. 13–15, (1995), In: 'Computation of 3D Complex Flows', eds. M. Deville, S. Gavrilakis and I.L. Rhyming, Notes on Numerical Fluid Mechanics, vol. **53**, pp. 22–30, Vieweg Verlag, Braunschweig, (1996).

[3] Breuer, M., Pourquie, M.: *First Experiences with LES of Flows past Bluff Bodies*, Proc. of the 3rd Intern. Symposium of Engineering Turbulence Modelling and Measurements, Heraklion–Crete, Greece, May 27–29, 1996, Engineering Turbulence Modelling and Experiments **3**, pp. 177–186, W. Rodi and G. Bergeles (eds.), Elsevier Science B.V., (1996).

[4] Breuer, M., Rodi, W.: *Large–Eddy Simulation of Complex Turbulent Flows of Practical Interest*, In: 'Flow Simulation with High–Performance Computers II', ed. E.H. Hirschel, Notes on Numerical Fluid Mechanics, vol. **52**, pp. 258–274, Vieweg Verlag, Braunschweig, (1996).

[5] Breuer, M.: *Numerical and modeling influences on large eddy simulations for the flow past a circular cylinder*, Proc. of the 11th Symposium on Turbulent Shear Flows, vol. **3**, pp. 26:7–26:12, September 8–11, 1997, Grenoble, France, (1997), Int. J. of Heat and Fluid Flow, accepted for publication, (1998).

[6] Breuer, M.: *Large Eddy Simulation of the Sub–Critical Flow Past a Circular Cylinder: Numerical and Modeling Aspects*, Int. J. for Numerical Methods in Fluids, John Wiley & Sons Limited, accepted for publication, (1998).

[7] Cantwell, B., Coles, D.: *An experimental study on entrainment and transport in the turbulent near wake of a circular cylinder*, J. Fluid Mech., vol. **136**, pp. 321–374, (1983).

[8] Rodi, W., Ferziger, J.H., Breuer, M., Pourquié, M.: *Status of Large Eddy Simulation: Results of a Workshop*, Workshop on LES of Flows past Bluff Bodies, Rottach–Egern, Tegernsee, Germany, June 26–28, 1995, Journal of Fluids Engineering, vol. **119**, no. **2**, pp. 248–262, (1997).

[9] Williamson, C.H.K.: *Vortex Dynamics in the Cylinder Wake*, Annu. Rev. Fluid Mech., vol. **28**, pp. 477–539, (1996).

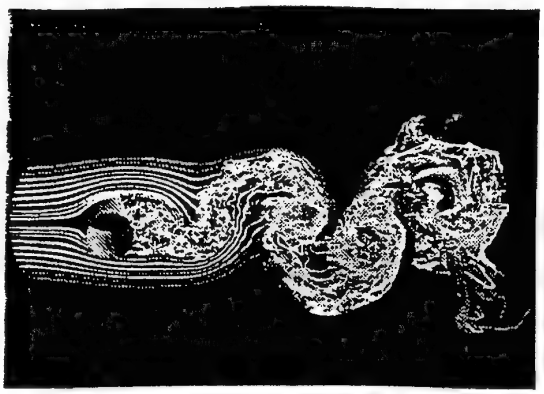

(a) Streaklines.

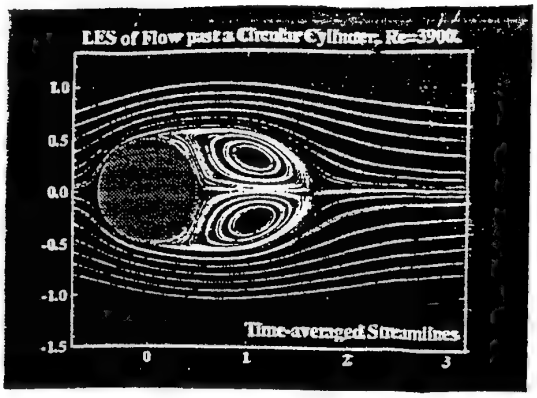

(b) Time–averaged streamlines.

Figure 1: Large eddy simulation of the flow past a circular cylinder at $Re = 3900$.

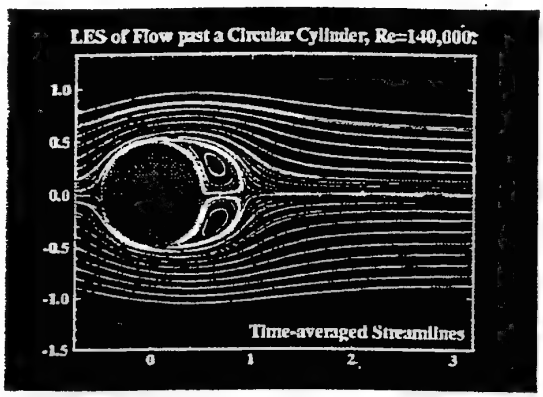

(a) Time–averaged streamlines.

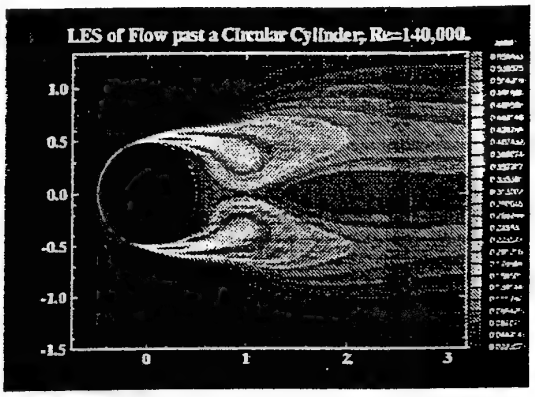

(b) Contours of $\overline{u'u'}$

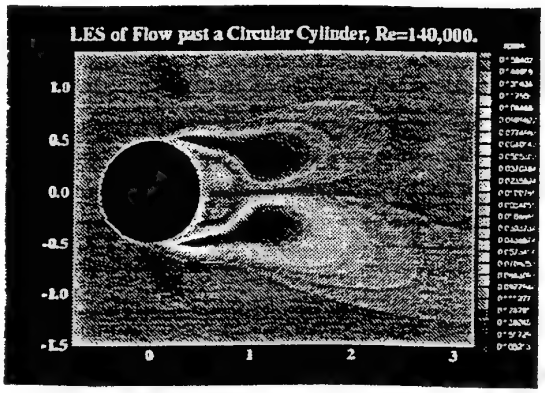

(c) Contours of $\overline{u'v'}$

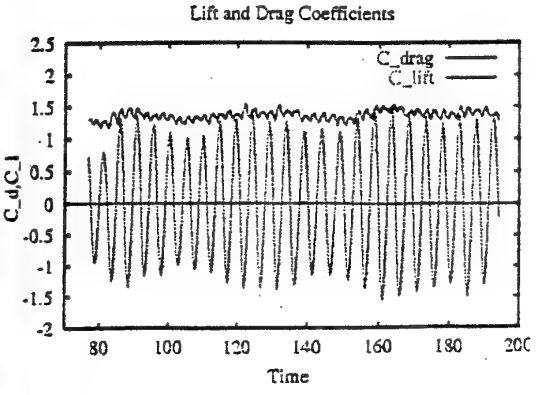

(d) Time history of C_d and C_l.

Figure 2: Large eddy simulation of the flow past a circular cylinder at $Re = 1.4 * 10^5$.

Numerical Simulation of Atmospheric Turbulence

F.T.M. Nieuwstadt and B.A. van Haarlem
J.M. Burgers Centre, Delft University of Technology
2628 AL Delft, the Netherlands.

Numerical simulation of turbulence has its roots in the atmospheric sciences and in particular in Numerical Weather Forecasting (NWP). Although the first ideas on NWP were formulated by Richardson in 1922, serious progress in NWP was only possible after the advent of electronic computers just after the second world war. As a spin off from NWP the first numerical simulations of turbulent convection were performed first in two dimensions by Lilly and somewhat later in three dimension by Deardorff. Especially, the work of Deardorff has become widely known and it has inspired the use of numerical simulation in other areas of turbulence research. Many of the techniques that Deardorff introduced and the results that he obtained, are still relevant today. As example we may mention here the Smagorinsky model which was originally developed as a model to parameterize the small scale motions in large-scale meteorological models. With respect to the atmospheric boundary layer Deardorff performed in the early 1970's the first LES of the so-called convective boundary layer. This is the turbulent layer which develops over a land surface and in which turbulence is generated as a result of natural convection due to solar heating. Since then LES computations of the convective boundary layer have been repeated many times and one could say that our general knowledge of this type of boundary layer is mainly due to LES.

As mentioned above, the use of LES has been in particular successful for the convective boundary layer. The results of LES have led here to the formulation of so-called mixed-layer scaling. In this scaling approach the variables in the convective boundary when scaled in terms of a limited number of characteristic parameters, collapse to universally valid scaling relationships. After mixed-layer scaling was derived based on LES data, it was also confirmed by laboratory and atmospheric experiments. A second

useful application of LES in the atmosphere is the neutral boundary layer. In this type of boundary layer temperature effects are absent. This is an exception in the real atmosphere and therefore it is difficult to observe a neutral boundary layer. In this case LES is the only alternative.

Experiments in the atmospheric boundary layer are very expensive and also very time consuming. Moreover, a completely reproducible and controlled experiment in the atmosphere is impossible by definition because of the natural variability of the atmosphere. Therefore LES seems an attractive alternative. Considering the successes of LES in the atmosphere as mentioned above, it seems tempting the use LES as an alternative for experiments. However, despite its successes LES also knows some failures. Examples are the behaviour of the horizontal velocity fluctuations and the near-surface skewness, both in the convective boundary layer. In these two cases LES results are in conflict with available experimental data. Therefore, an experimental verification of the numerical LES results is mandatory before LES can be fully trusted as substitute for experiments.

Mixing by Nonvertical Shear in the Stably Stratified Ocean

Sutanu Sarkar and Frank G. Jacobitz

University of California at San Diego, La Jolla, CA 92093

1 Introduction

Mixing of water masses of different densities, natural or man-made discharges into the ocean, life-supporting nutrients, as well as temperature and density contrasts is an important determinant of local and global features of the ocean climate and ecosystem. The additional effect of stratification induced by temperature and salinity gradients, as well as that of earth's rotation must be considered when mixing is studied in the context of geophysical and environmental flows. At scales of hundred meters or less, the effects of earth's rotation may often be neglected. The microstructure at these scales is thought to be related to a variety of mechanisms that include nonlinearly breaking internal waves, shear layer instabilities, convective instabilities and boundary layer turbulence. Although diverse in their origin, mixing processes in the ocean often involve a competition between shear and stable stratification. Therefore, the role of stably-stratified shear flow in maintaining the ocean microstructure requires study. Flows with vertical shear, $d\overline{U}/dz$, have been the subject of numerous studies; however, the horizontal shear component $d\overline{U}/dy$ has received little to no systematic investigation. The influence of horizontal shear, $d\overline{U}/dy$, with emphasis on its comparison with the oft-studied case of vertical shear is the subject of this work.

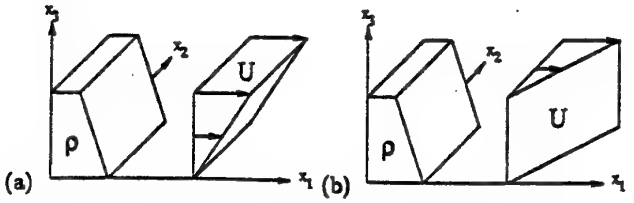

Fig. 1. Sketch of (a) vertically sheared flow and (b) horizontally sheared flow. There is a stable vertical density stratification in both cases

It should be noted that, despite the preponderance of vertical shear in the open ocean, there are field measurements, for example, in coastal fronts [1] and straits [2] that indicate a significant $d\overline{U}/dy$ component. Flows over seamounts where greatly increased dissipation rates have been measured [3] as well as

side- and bottom-boundary flows, most likely, have substantial horizontal shear components. To the best of our knowledge, there have been no theoretical or laboratory studies focussed on horizontally sheared, vertically stratified flow. However, laboratory experiments relevant by virtue of the presence of horizontal shear include the study of a front in a rotating, stratified fluid [4], the stratified wake of a sphere [5], and the stratified jet [6].

Figures 1(a)-(b) show schematics of the case with uniform vertical mean shear, $d\overline{U}_1/dx_3$ and uniform horizontal mean shear, $d\overline{U}_1/dx_2$, respectively. In both cases, the uniform mean stratification is vertical and stable.

2 Approach

Since little is known from existing studies about the influence of horizontal shear on mixing in a vertically stratified fluid, direct numerical simulation (DNS) is an attractive approach that avoids the uncertain influence of turbulence models on the conclusions. In DNS, all dynamically important scales of motion are resolved which, given current computer hardware capabilities, limits the simulations to moderate Reynolds number. In the case of uniformly distorted flow, the appropriate Reynolds number $Re_\lambda = q\lambda/\nu$ is based on the rms velocity, $q = \sqrt{2K}$, and the Taylor microscale, $\lambda = \sqrt{5\nu q^2/\epsilon}$, and is limited to $Re_\lambda < 150$ in parametric investigations. Here K and ϵ denote the turbulent kinetic energy and dissipation rate, respectively.

The unsteady, three-dimensional, Navier-Stokes equations with the Boussinesq approximation are numerically solved. A spectral collocation method is used for the spatial discretization and a third-order, low-storage, Runge-Kutta scheme for the temporal advancement in order to obtain high accuracy. The equations are solved in a reference frame that moves with the mean velocity[7] that, while introducing additional time-dependent terms in the governing equations, allows the use of periodic boundary conditions and thereby Fourier basis functions. Up to $288 \times 144 \times 144$ grid points are used.

A series of simulations with vertical shear and a second series with horizontal shear were performed with the same magnitude of shear S but with different values of the Brunt-Väisälä frequency $N = (-gS_\rho/\rho_0)^{1/2}$ obtained by varying the mean stratification S_ρ. Thus, the generalized Richardson number $Ri = N^2/S^2$ was varied in the range $0 < Ri < 3$.

Although, the focus is on contrasting the limiting cases of either horizontal or vertical shear, the effect of varying the relative magnitude of horizontal mean shear $S_2 = S\cos\theta$ to the vertical mean shear $S_3 = S\sin\theta$ is also ascertained. The relative magnitude was varied by conducting a third series of simulations where the shear inclination angle θ is varied between $\theta = 0$ (vertical shear) and $\theta = \pi/2$ (horizontal shear) while keeping the magnitude of the shear $S = \sqrt{(d\overline{U}_1/dx_3)^2 + (d\overline{U}_1/dx_2)^2}$ constant.

3 Results

The two shear components, dU/dy and dU/dz, result in two additional nondimensional parameters. If two-dimensional linear instabilities in the $(x,\ z)$ plane are considered, the vertical Richardson number $Ri_v = N^2/(dU/dy)^2$ is the *only* relevant nondimensional parameter which would imply that stratification has no effect on the dynamics when the shear is horizontal. DNS shows that stratification has a substantial stabilizing influence even when the shear is horizontal; it is clear that three-dimensional fluctuations must be considered.

The energetics of the fluctuations can be studied through the transport equation for turbulent kinetic energy, K, wherein the ratio of the buoyancy flux B to the production term P in the turbulence can be written as

$$\frac{B}{P} = \left(\frac{\alpha_t}{\nu_v}\right)\left(\frac{1}{\sin^2\theta + \nu_h/\nu_v \cos^2\theta}\right)\left(\frac{N^2}{S^2}\right) \tag{1}$$

after introducing the vertical and horizontal momentum transport coefficients ν_v and ν_h, respectively, as well as the mass transport coefficient, α_t. Equation (1) is exact and implies that, two nondimensional parameters: first, the generalized Richardson number $Ri = N^2/S^2$ based on the *magnitude* of the shear $S = \sqrt{(d\overline{U}_1/dx_3)^2 + (d\overline{U}_1/dx_2)^2}$, and, second, the shear inclination angle θ are required.

In the limiting case of purely horizontal shear, $d\overline{U}/dy$, the relevant stratification-related parameter becomes $Ri = N^2/(d\overline{U}/dy)^2$.

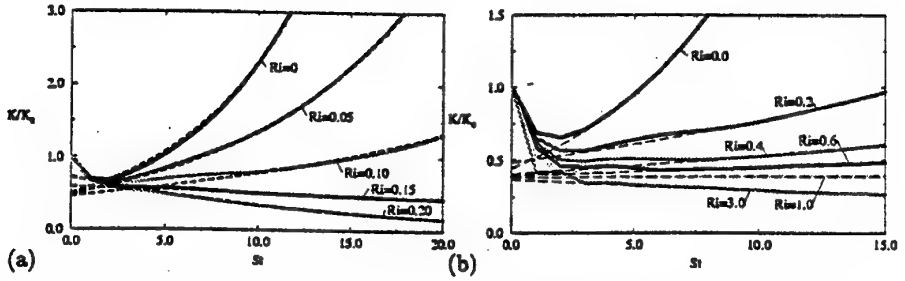

Fig. 2. Evolution of turbulent kinetic energy K for various values of Richardson number Ri in the (a) vertically sheared case, and (b) horizontally sheared case. St is time normalized with mean shear S. Dashed lines are the exponential approximation to the solution.

The dependence of the turbulence evolution on the generalized Richardson number, $Ri = N^2/S^2$, is now discussed. Figure 2 shows that, for the same value of Ri, the the turbulence is much more energetic in the case of horizontal shear. The critical Richardson number, Ri_{cr}, is the value of Ri below which

turbulence shows asymptotic growth and above which turbulence decays. The value of $Ri_{cr} = 1.0$ in the horizontally sheared case is an *order of magnitude* larger than $Ri_{cr} = 0.15$ in the vertically sheared case. The vertical mass transport is also an order of magnitude larger when the shear is horizontal. An explanation for these observations will be given in the full paper. In addition, results on the turbulence mixing coefficients, large- and small-scale anisotropy and visualizations of mixing will be given in the full paper.

Acknowledgements

Support was provided by ONR, PO program through grant ONR N00014-94-1-0223. Supercomputer time was provided by the San Diego Supercomputer Center (SDSC) and the US Army Corps of Engineers Waterways Experiment Station (WES). Helpful discussions with Charles W. Van Atta are acknowledged.

References

1. Johannessen, J. A., Shuchman, R. A., Digranes, G., Lyzenga, D. R., Johannessen, O. M., & Vachon, P. W. (1996) Coastal ocean fronts and eddies imaged with ERS 1 synthetic aperture radar. *J. Geophys. Res.* **101**, C3, 6651-6667.
2. Farmer, D. M., D'Asaro, E. A., Trevorrow, M. V. & Dairiki, G. T. (1995) Three-dimensional structure in a tidal convergence front. *Continental Shelf Research* **15**, 1649-1673.
3. Lueck, R. G. & Mudge, T. D. (1997) Topographically induced mixing around a shallow seamount. *Science* **276**, 1831-1833.
4. Thomas, P. J. & Linden, P. F. (1996) A laboratory simulation of mixing across tidal fronts. *J. Fluid Mech.* **309**, 321-344.
5. Spedding, G. R., Browand, F. K., & Fincham, A. M. (1996) Turbulence, similarity scaling and vortex geometry in the wake of a towed sphere in a stably stratified fluid. *J. Fluid Mech.* **314**, 53-103.
6. Voropayev, S. I., Zhang, X., Boyer, D. L., Fernando, H. J. S., & Wu, P. C. (1997) Horizontal jets in a rotating stratified fluid. *Phys. Fluids* **9**, 115-126.
7. Rogallo, R. S. (19981) Numerical experiments in homogeneous turbulence. *NASA TM 81315.*

Applications of the Non-linear Galerkin Methods to some flow problems

Kunt Atalik and Akin Tezel
Boğaziçi University, Bebek, İstanbul, 80815, Turkey

Abstract

Non-linear Galerkin Methods which have been developed in the context of the long-time integration of dissipative evolution equations have been applied to transition regimes of the plane channel flow and the temporally growing free shear layer problems. Those methods have been proposed in the literature to approximate the 'inertial manifolds' which are finite-dimensional smooth manifolds containing the global attractor, a finite-dimensional manifold of complex structure and attracting all the solutions at an exponential rate in the phase space. These manifolds yield an interaction law between the small and large scale components of the flow and reduce the number of modes needed to describe the flow dynamics. This approach is thought to be promising in the context of direct numerical simulations of Navier-Stokes equations. That work aims to test the convergence and efficiency of different Nonlinear Galerkin schemes with respect to each other and with respect to the classical Galerkin spectral method in the above flow cases.

Direct Numerical Simulation of Intrusion Fronts

Carlos Härtel

Swiss Federal Institute of Technology
Institute of Fluid Dynamics
CH-8092 Zürich, Switzerland

Intrusion fronts of heavy fluid which propagate in an environment of lighter fluid are commonly encountered in numerous geophysical applications (see Simpson, 1997), well-known examples being moving atmospheric cold fronts, thunderstorm outflows, powder-snow avalanches or muddy underflows in lakes or oceans. Their study is also of interest in the engineering sciences because of the important role they play in many problems related to industrial safety and environmental protection (see Fanneløp, 1994). A typical scenario where intrusion fronts may be expected to form is the accidental release of dense (and possibly hazardous) industrial gases which gravity may spread over relatively large distances at an appreciable speed. Extensive theoretical and experimental studies were devoted to intrusion fronts in the past, but very few accurate numerical simulation studies have been presented so far. Most of the numerical studies conducted in this field have employed approximate methods, based e.g. on the shallow-water equations, and often utilize empirical models to account for turbulent transport. Today, direct numerical simulations (DNS) allow to study the physics of intrusion fronts with much greater accuracy. DNS provides the full information on the three-dimensional and time-dependent flow evolution, and it proves to be a very powerful tool to address some of the intricate problems related to the topology and stability characteristics of intrusion fronts.

The talk will present results from a research project in which the DNS technique is applied for the first time to study fundamental physical properties of intrusion fronts. Several prototype flows have been considered, one of these being the mutual intrusion of two fluids of different density in a plane channel. Initially the two fluids are separated by a vertical membrane. After the membrane has been removed a heavy-fluid front and a light-fluid front develop and propagate along the lower and the upper channel wall, respectively. This type of flow has often been studied in experiments (see Gröbelbauer *et al.*, 1993) and is usually referred to as the "lock-exchange problem". Distinct features of lock-exchange flows are the steep velocity and density gradients across the heads of the fronts, the thin boundary layers that form at the walls and the stably stratified interface between the two fluids in the interior of the channel. In Figure 1 the evolution of a lock-exchange flow at a Grashof number of about 10^6 (based on buoyancy velocity and channel half width) is illustrated by means of isocontours of density.

The numerical simulations are based on the Boussinesq equations, where density variations are assumed to be small. For the spatial discretization Fourier expansions are used in the wall-parallel directions together with a spectral-element technique in the normal direction. A third-order Runge-Kutta method is employed for the temporal discretization of the nonlinear terms together with a second-order accurate Crank-Nicolson scheme for the viscous terms and the pressure. To validate the code simulations

of Rayleigh-Bénard convection were conducted and the results were compared with linear stability theory and reference data from the literature. In all cases an excellent agreement could be obtained. A detailed description of the numerical scheme is given in Härtel *et al.* (1997).

Among other things, we will discuss results of an analysis of the pronounced two-dimensional Kelvin-Helmholtz type instability at the interface between light and heavy fluid, and also of the three-dimensional lobe-and-cleft instability commonly observed at the head of propagating intrusion fronts. The three-dimensional simulations had to be restricted to moderate Grashof numbers of the order of 10^6 due to the excessive resolution requirements. However, much higher Grashof numbers can be reached, if strictly two-dimensional (2D) intrusion fronts are considered. We have conducted 2D simulations for Grashof numbers of up to $2 \cdot 10^9$ in order to examine issues like the dependence of the Froude number Fr of the propagating fronts (i.e. the front speed normalized by the respective buoyancy velocity) on viscous forces. In Figure 2 the relation between Fr and Gr is depicted for lock-exchange simulations with no-slip and free-slip conditions, respectively, at the top and bottom boundary. It is readily seen that for no-slip walls the front speed remains sensitive to viscous effects over the whole range examined. Moreover it can be seen that our direct simulations are in good agreement with recent experimental data.

References

FANNELØP, T. K. 1994 *Fluid Mechanics for Industrial Safety and Environmental Protection.* Elsevier Science B.V., Amsterdam.

GRÖBELBAUER, H. P., FANNELØP, T. K. & BRITTER, R. E. 1993 The propagation of intrusion fronts of high density ratios. *J. Fluid Mech.* **250**, 669-687.

HÄRTEL, C., KLEISER, L., MICHAUD, M. & STEIN, C. F. 1997 A direct numerical simulation approach to the study of intrusion fronts. *Journal of Engineering Mathematics* **32**, 103-120.

MÜLLER, J. & FANNELØP, T. K. 1996 *Private Communication.*

SIMPSON, J. E. 1997 *Gravity Currents: in the Environment and the Laboratory.* 2nd. edition, Cambridge University Press, Cambridge.

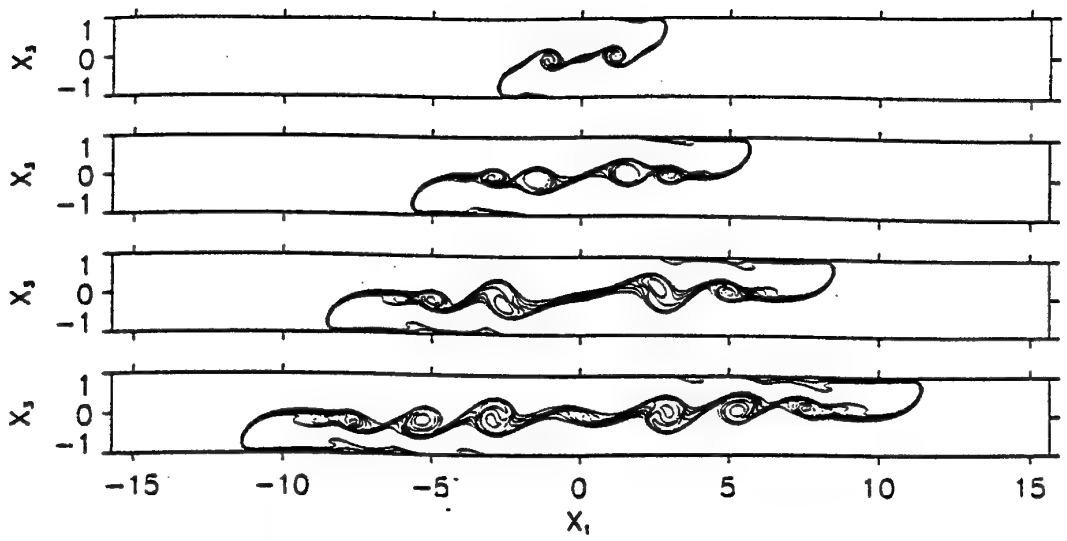

Figure 1: Numerical simulation of two-dimensional lock-exchange flow at a Grashof number of 10^6. Shown are isocontours of density for four successive time instants after the initial release.

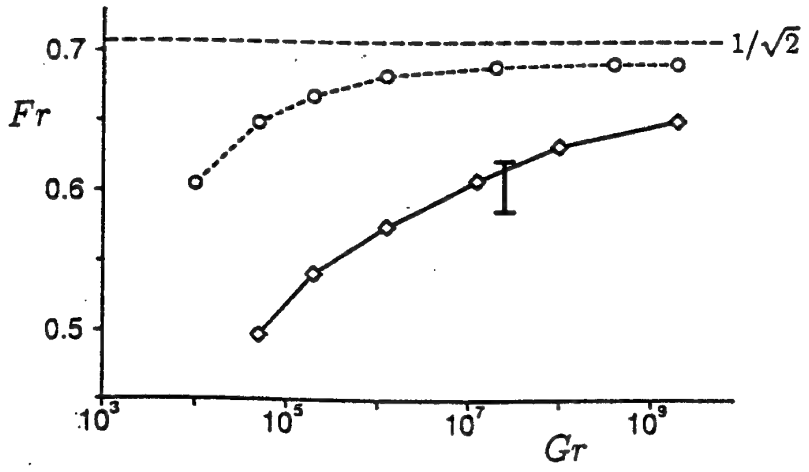

Figure 2: Froude number Fr of the front as a function of Grashof number for lock-exchange flows. Results for no-slip walls (solid line) and slip boundaries. Symbols identify the individual simulations. The vertical bar gives the span of results obtained in recent lock-exchange experiments with Ar and CO_2 (Müller & Fanneløp, 1996).

Nonlinear stability of the compressible attachment-line boundary layer

R.S. Heeg[1] *& B.J. Geurts, Faculty of Mathematical Sciences, University of Twente, P.O. Box 217, 7500 AE Enschede, The Netherlands*

The research presented in this paper is concerned with the stability properties of the compressible attachment-line boundary layer. The instability of flow near the leading edge of e.g. a swept wing is of great practical importance. This kind of instability may lead to growing disturbances which can be convected downstream and thus influence the transition from laminar to turbulent flow around the wing. Thereby this process may influence aerodynamic properties to a large extent.
The attachment-line region consists of the front part of a wing. In figure 1 this region is shown schematically in order to define the coordinate directions. To emphasize the far-field velocity $\mathbf{U}$ is at an angle with respect to the leading edge which is shown as the dotted line. As shown x denotes the chordwise direction, y the direction normal to

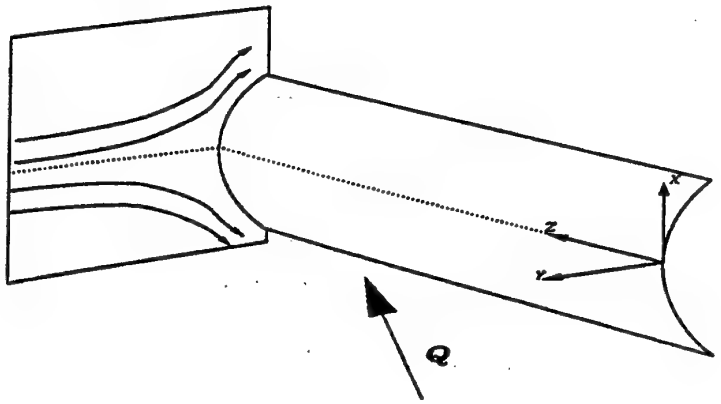

Figure 1: Attachment-line geometry

the wall and z the spanwise direction.

To address the stability problem the flow is decomposed into a perturbation and a basic flow part. The Navier-Stokes equations govern the evolution of the perturbation around the basic flow. The basic flow is the compressible counterpart of the swept Hiemenz flow. The Navier-Stokes equations in disturbance form have been used for the study the nonlinear stability of the attachment-line boundary layer.

As in the incompressible case the linear eigenmodes follow a sequence symmetric (S1), antisymmetric (A1), symmetric (S2) etc. That is, the most unstable mode is symmetric, the next most unstable mode is antisymmetric, then the next unstable mode is symmetric and so on. In order to study the nonlinear evolution of the disturbances, the linear perturbations are used as initial fields in a number of three-dimensional temporal direct numerical simulations (DNS). These simulations employ high-order finite-difference discretization in space and implicit time integration using the Crank

[1]Present address: J. Huizingalaan 233, 1066 AN Amsterdam, The Netherlands.

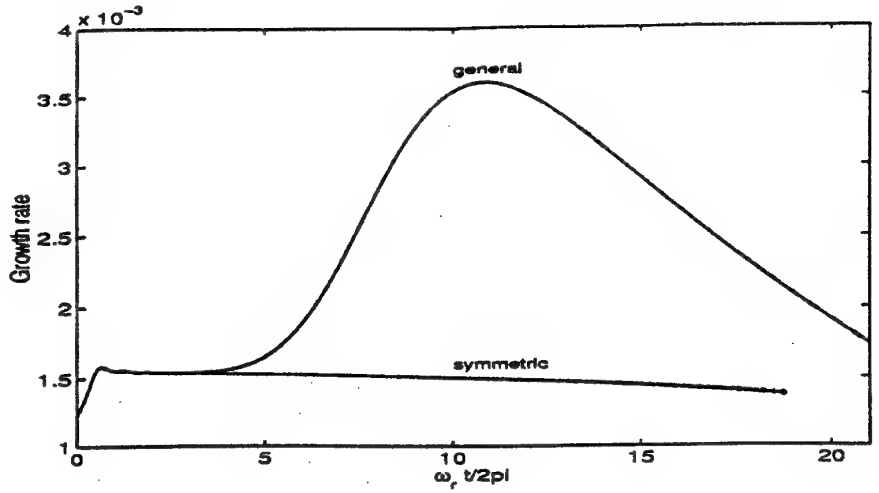

Figure 2: Growth rate as function of time at $R = 800$, $M = 0.2$, symmetric and general simulation.

Nicolson scheme. In the z-direction periodic boundary conditions are prescribed. These nonlinear simulations have been validated using both resolution studies and linear stability theory. The results computed with the implicit time integration scheme have also been compared with results computed with a conventional explicit Runge-Kutta scheme in order to assess the time step used. It was found that the use of the implicit scheme resulted in much lower CPU-times than the use of the explicit scheme without affecting the accuracy of the results.

The perturbations could be restricted to be symmetric with respect to the attachment-line. This is in fact an extension of two-dimensional nonlinear calculations of previous researchers based upon the Görtler-Hämmerlin assumption. A comparison has been made between the evolution of these three-dimensional symmetric disturbances and the case were no restriction on the shape of the perturbations has been made. It has been found that, for general disturbances, the results start to deviate significantly from linear stability theory for disturbance levels of about 1%. At these disturbance levels the growth rate starts to increase to a much higher value, see figure 2. The behaviour of the u- and the T-disturbances seems to be entirely responsible for the deviation from linear theory. However, when only symmetric modes are allowed in the simulations, the sudden increase of the growth rate is absent. Therefore, the interaction between symmetric and antisymmetric modes is likely to be responsible for the sudden increase of the growth rate.

In the past no such nonlinear interactions between symmetric and antisymmetric modes were found for two reasons. A number of researchers used only symmetric modes in their nonlinear simulations, e.g. Hall *et al.* (1986) and Theofilis (1998). Other researchers did use a general model for the perturbations, but used extremely small disturbance amplitudes, e.g. Spalart (1988) and Joslin (1995). Spalart also studied turbulent incompressible attachment-line flow, but the transition to turbulence was not considered by him.

DNS/LES of Turbulent Flow in a Square Duct: A Priori Evaluation of Subgrid Models

Peter L. O'Sullivan and Sedat Biringen,
Department of Aerospace Engineering,
University of Colorado,
Boulder, CO 80309-0429

and

Asmund Huser,
Det Norske Veritas,
Oslo, Norway.

The direct simulation code for incompressible flow in a straight square duct developed by Huser and Biringen [1] has been employed to generate a high-resolution ($101 \times 101 \times 128$) database at $Re_\tau = 600$ consisting of 80 total flow realizations which are decorrelated in time. The data were then post-processed to perform *a priori* testing of two dynamic SGS turbulence models, namely the dynamic Smagorinsky SGS model (DSM) and the dynamic two-parameter mixed model (DTM).

For the duct flow there are two inhomogeneous directions which lead to "non-canonical" overlapping turbulent boundary layers presenting a challenge to more conventional approaches to large-eddy simulation. The duct can be thought of as a testing ground for developing subgrid models capable of capturing turbulent corner flow dynamics. The two point correlation tensor also furnishes us with estimates of the size of large-scale flow features, in particular quasi-streamwise vortices in the corner region of the duct. This information serves as a guideline in the minimum grid-spacing required for large-eddy simulations of corner flows in which the "large eddies" are indeed captured by the computer simulation. The mean diameter of streamwise vortices appears to scale on inner variables in the near-wall region although this fact has not been established rigorously for corner flows of this type. If inner scaling is indeed appropriate then there will be a stringent grid resolution requirement in high Reynolds number duct flows in order to adequately capture the "smallest large scales" which are dynamically significant in the corners.

The individual flow fields were also used to perform *a priori* tests of both the DSM and the DTM. The success of these models for large eddy simulations in corner flows (with secondary flows of the second kind) is as yet unexplored. The mixed models studied recently by Zang, Street and Koseff [2], Liu, Meneveau and Katz [3] and Salvetti and Banerjee [4] have shown better correlation with the true subgrid stresses. The mixed model reduces the magnitude of the Smagorinsky parameter and also generally makes it positive (enhanced effective viscosity) and hence alleviates the drawbacks (*viz.* mathematical inconsistency, negative total viscosity and numerical instability) of the DSM. The main reason for this is the applicability of Bardina's scale similarity model to the cross terms in the subgrid scale stresses. The scale-similar part of the model also permits non-alignment of the principal axes of the SGS stresses with those of the resolved strain rate tensor which is not the case in any of the Smagorinsky-type models.

Our evaluations currently consist of filtering individual DNS realizations in the ensemble in just the streamwise direction of the flow which is treated via periodic boundary conditions in the simulation code. Filtering in the inhomogeneous directions is not well defined since filtering and spatial differentiation do not commute, but rather introduce second order differencing errors whose role is difficult to assess. Hence, we retain the high spatial resolution in the wall-normal directions.

(The extension to non-uniform grid filters and application to wall bounded spatial filtering is under investigation currently.) We base our model tests on individual realizations, the SGS dissipation term, ensemble-average behavior and also on the correlation coefficient of modelled to exact SGS dissipation, $\rho(\varepsilon)$. For the DSM we find that $\rho(\varepsilon) \approx 0.1 - 0.2$ at best in agreement with Clark, Ferziger and Reynolds [5]. The correlation in the corner region is largely similar to that in the wall bisector region. For the DTM we find that $\rho(\varepsilon) \approx 0.8 - 0.9$ indicating the (expected) improvement gained in using a mixed model. The correlation is not diminished in the corner regions of the flow. The accompanying figure illustrates this result.

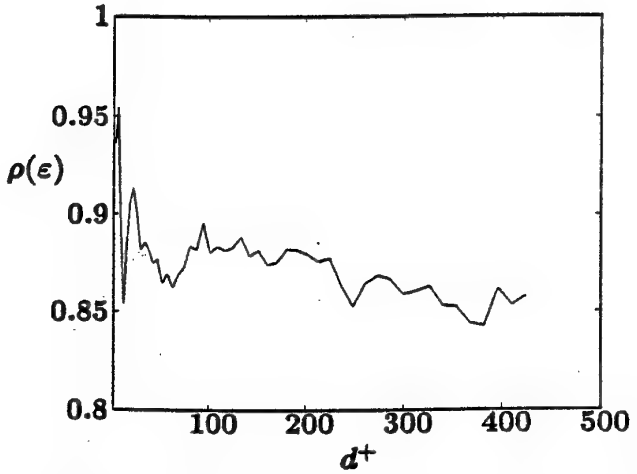

Figure 1: Correlation coefficient for SGS dissipation along the corner bisector for the DTM.

A favorable outcome of *a priori* model testing/evaluation does not necessarily provide a sufficient condition for a successful LES using a given model but it does provide a necessary condition. A model which performs poorly in *a priori* tests stands little chance of providing good temporal fidelity in LES even though it may provide some measure of success in the mean (the success of early LES using the Smagorinsky model are a case in point). The ultimate test of a given model is in its success when utilized in a LES of high Reynolds number turbulence.

We will present results of this work and discuss prospects for successful large eddy simulations in similar complex flows of this kind.

References

[1] A. Huser & S. Biringen. Direct numerical simulation of turbulent flow in a square duct. *Journal of Fluid Mechanics*, **257** pp.65–95, 1993.

[2] Y. Zang, R. L. Street & J. R. Koseff. A dynamic mixed subgrid-scale model and its application to turbulent recirculating flows. *Physics of Fluids* **A**, **5** (12) pp.3186–3196, 1993.

[3] S. Liu, C. Meneveau & J. Katz. On the properties of similarity subgrid-scale models as deduced from measurements in a turbulent jet. *Journal of Fluid Mechanics*, **275** pp.83–119, 1994.

[4] M. V. Salvetti & S. Banerjee. *A priori* tests of a new dynamic subgrid-scale model for finite-difference large-eddy simulations. *Physics of Fluids*, **7** (11) pp.2831–2847, 1995.

[5] R. A. Clark, J. H. Ferziger & W. C. Reynolds. Evaluation of subgrid models using an accurately simulated turbulent flow. *Journal of Fluid Mechanics*, **91** pp.1, 1979.

ACKNOWLEDGEMENT

This work was supported by NSF grant ECS – 9725504 and ONR grant N00014-95-1-0419; computer resources were provided by CEWES MSRC: Vicksburg.

SHALLOW WATER MODEL THE BOSPHORUS CURRENT

HALUK ÖRS

School of Engineering, Boğaziçi University, Bebek, Istanbul, 80815, Turkey

INTRODUCTION

Bosphorus strait is a quite narrow channel with a mean width of about a kilometer and length of about 30 km connecting the Black Sea to the internal sea of Marmara which is considered part of the Mediterranean. The maximum depth is about 110 meter. Since tidal effects are almost non-existent on the Bosphorus, measurements show that tidal elevation is under 4 cm, the flow is driven mainly by the pressure gradient in the Black Sea- Marmara Sea direction. This gives rise to a current with a speed of about 4 km/hour in the upper levels. The gradient of the density due to the salinity differences between the Mediterranean water of the Marmara Sea and the less saline Black Sea water gives rise to a countercurrent in the lower levels of the Bosphorus. The complex geometry gives also rise to local currents of different directions and the true representation of the flow field would certainly necessitate a three dimensional model with a very fine mesh. However, surface currents are dominant and a 2-D shallow water model necessitating no more than a desktop computer can be expected to represent the flow field with reasonable accuracy.

Application of the Galerkin finite element method to the solution of the shallow water equations could be dated back to the works of Taylor and Davis (), Norton, King and Iceman () and Connor and Wang(). These early researchers applied standard Galerkin method to discretize the shallow water equations in space and used Runge-Kutta or predictor-corrector methods to integrate in time the resulting system of ordinary differential equations. Considering then available computer storage capacities they used highly coarse meshes with element sizes of the order of kilometers. The well known stability problems for standard Galerkin methods were circumvented by taking extremely large eddy viscosity coefficients or tuning the bottom friction coefficient for damping. For example in the work of Norton etal the diffusivity coefficient was assumed to take the value of 10000 m^2/s, whereas the accepted value is around 10 m^2/s. One had to wait for the development of upwinding techniques in the context of finite elements for the solution of the convection-diffusion equation without excessive dissipation.

Shortcomings of the shallow water modelling are that the velocities computed represent simply the height averaged values and gradients in the vertical direction are lost. In cases where these gradients are large shallow water solutions are very difficult to compare with measured values. Also it is commonly known that surface waves in coastal seas generate a considerable high velocity current in a direction toward or outward the coast. This difficulty is usually circumvented by considering that the depth is always larger than a minimum value, which in our case is assumed to be 5 meters. This assumption is quite correct in the case of Bosphorus since both coasts can be considered to form a vertically walled channel. In case there is beach special precautions need to be taken as is shown in (Kawahara,1984)

Shallow water equations are a good approximation to Navier-Stokes equations in cases the vertical acceleration of the fluid can be neglected. This helps in circumventing the difficulty associated with the computation of the pressure term in the Navier-Stokes equation since the pressure is now hydrostatic and easily computed. Furthermore the problem is no more three dimensional and the number of operations and storage requirements are at least an order of magnitude smaller. Since the bathymetry is also taken into account, shallow water modeling is actually more than a 2-dimensional model of the flow field and can be classified as a quasi

three dimensional model. Finite element method is the natural choice in the derivation of the discrete system of equations modeling phenomena in complex geometries allowing us to use an unstructured mesh. Inclusion of the viscous effects by the use of lateral eddy viscosity makes the system of equations we use different from the classical shallow water equations where no viscosity term exists and the type of the equation is quasi-hyperbolic. The type of the equation system we will be dealing with is incompletely parabolic (Gustafsson and Sundström) .

It is well-known that the structure of the linear system of equations has long been a dominant issue in the choice of solver routine and usually effort is made that the bandwidth of the final matrix is as small as possible to minimize the storage requirement. However the development of the matrix-free solver routines based on the Generalized Minimal Residual (GMRES) method in recent years (Saad) eliminated this difficulty. The essence of the solver routine consists in writing simply element level matrices and collecting them in a three indices array without assembly. Application of the essential boundary conditions at the element level further reduces the number of the equations to be solved. This information together with the connectivity table is sent to the iterative solver. The advantage of this method is to reduce the memory requirements considerably and therefore give the possibility of attacking large scale problems on a desktop computer . The code is written with consideration of a parallel implementation but the results presented herein were obtained on a single processor workstation.

As to the time-integration, trapezoidal rule of time integration is employed. Trapezoidal rule includes both implicit and explicit time integration schemes but for the flexibility of the choice of the timestep without violating the CFL condition implicit scheme is preferred. The use of the explicit scheme is certainly more efficient computationally but the drawback is that CFL condition restricts the size of the timestep unless a specially designed mesh is used where it is made sure that, based on the surface gravity wave speed $\sqrt{gh}$ for a preassigned time step, CFL condition is not violated. (Kashiyama)

GOVERNING EQUATIONS

Averaging the velocity field in the vertical direction along which fluid acceleration is neglected and therefore pressure is assumed to be simply hydrostatic, Navier-Stokes equations are transformed into the following set of equations,

$$\frac{\partial \zeta}{\partial t} + \{(h+\zeta)u_i\}_{,i} = 0, \tag{1}$$

$$\frac{\partial u_i}{\partial t} + u_j u_{i,j} = -g\zeta_{,i} - \varepsilon\left(u_{i,j} + u_{j,i}\right) + \tau_{si} - \tau_{bi} + f_i \tag{2}$$

$$\frac{\partial C}{\partial t} + u_i C_{,i} - \kappa C_{,ii} = s \tag{3}$$

where ζ represents the free surface elevation from the mean water level, h local mean water depth, u_i vertically averaged horizontal velocity components, C the contaminant concentration, ε eddy viscosity coefficient, g acceleration due to gravity, τ_{si} wind stress component at the free surface, τ_{bi} bottom friction stress component, f_i Coriolis force component and s the contaminant source term. With this formulation the four dependent variables of the initial problem, i.e u_i for i=1,2,3, p are replaced by the three dependent variables u_i for i=1,2, and ζ. The difficulty concerning the time dependent nature of the free surface is taken care of by computing its elevation at every timestep and using it in computing the local pressure gradient in conjunction with the local mean water level h. The surface stress term due to the wind is computed as,

$$\tau_{ts} = \gamma \rho_{air} w_i \sqrt{w_k w_k} \qquad (4)$$

where w_i is the wind velocity component, ρ_{air} air density and γ a friction coefficient with a value of 0.0026 in SI system of units. The bottom friction term is assumed to be given by the formula,

$$\tau_{tb} = \frac{n^2 g}{h^{1/3}} u_i \sqrt{u_k u_k} \qquad (5)$$

where n is the Manning coefficient with a value of 0.030 in the SI system. The contaminant diffusion coefficient κ is assumed to take the value of 5 m^2/s.

As to the mathematical classification of these equations, the continuity equation is a first order hyperbolic equation, whereas the momentum and transport equations are second order., incompletely parabolic.(Gustaffson). Boundary conditions appropriate for the well-posedness of these equations have been subject to a vast literature and according to Abraham et. al.() they are as follows:
For subcritical flow, which corresponds to our case, hyperbolic equation requires 2 inflow and 1 outflow boundary condition, whereas the incompletely parabolic equations require 2 boundary conditions on land boundaries, 3 inflow and 2 outflow boundary conditions at open (sea) boundaries.
We will see below how these conditions translate into the weak formulation.

The simply connected open domain $\Omega \subset R^2$ over which the governing equations are valid is closed by the boundary $\Gamma = \Gamma_1 \cup \Gamma_2$ where Γ_1 denotes the land type boundary and Γ_2 ocean type boundary, with $\Gamma_1 \cap \Gamma_2 = \varnothing$. On land type boundary there is no effluent flux and the boundary condition is reduced to the adherence condition for viscous fluid. However since we are not interested in resolving the boundary layer and our mesh size is extremely large compared to the boundary layer thickness we will relax this condition by cancelling the normal component of the velocity.(Gray)

$$u_i n_j = 0 \text{ on } \Gamma_2 \qquad (6)$$

On ocean type boundary , weak formulation gives rise to a boundary condition of the form

$$t_i = -g\zeta_{,j} + \varepsilon\left(u_{i,j} + u_{j,i}\right)n_j = \bar{t}_i \text{ on } \Gamma_1 \qquad (7)$$

Since usually we have no way of measuring the shear stress term along the open boundary we will enforce this condition after neglecting the viscosity term and setting the tangential component of the velocity at the inlet equal to zero. Therefore on the ocean boundary , the pressure being simply hydrostatic the following condition will be enforced,

$$\zeta = \bar{\zeta} \text{ on } \Gamma_1. \qquad (8)$$
$$u_i n_j = -\bar{u} \text{ on } \Gamma_1 \text{ for the inlet part only.}$$

In the following we prefer to work with the total height $H = h + \zeta$.

FINITE ELEMENT DISCRETIZATION

Flow field being divided into triangular elements, the dependent variables are represented over each element by the linear interpolating functions Φ_i. This is equivalent into discretizing the dependent variables in terms of their nodal values as,

$$H = H_\alpha \Phi_\alpha, \quad u_i = u_{i\alpha} \Phi_\alpha, \text{ and } C = C_\alpha \Phi_\alpha \qquad (9)$$

where repeated indices mean summation unless otherwise stated.

Considering the size of the elements used, side length between about 100 m and 300 m, and the thickness of the boundary layer on the coast it might have been more accurate to use no flux boundary condition along the coast but with the primitive variables formulation of the governing equations this type of boundary condition is difficult to be implemented on a boundary not necessarily aligned with the main axis. Stream function-vorticity formulation is certainly more suitable in this sense but then linear triangular elements are unable to take account of the higher order derivatives originating from the viscous terms. Higher order elements would be needed and for the same mesh size that would at least double the number equations to be solved in each time step. The approach mentioned by Gray ()for the implementation of slip boundary conditions by rotation of the element matrices corresponding to boundary elements is a method operational within the context of linear elements but has not been attempted in this work.

Initially it is assumed that the deviation from the mean water level is zero everywhere except on the boundary at the Black Sea where a constant deviation of 0.30 m, based on measurements between Black Sea and Marmara Sea levels, is assumed and maintained during the computation. This difference in water level creates a gravity travelling along the strait and eventually sets up the velocity field. The time the gravity wave takes to traverse the strait is about 3000 s which corresponds to a wave speed of 10 m/s. This is the wave speed corresponding to a constant depth of approximately 10 m.. The velocity field of interest corresponding to a quasi steady state is obtained after t=3000 s. This velocity distribution could afterwards be used as initial velocity distribution computations with wind loadings and the contaminant transport equation solution. Most common winds in the Bosphorus are northerly with eventual southerly winds in winters. In the computations presented herein the wind speed is taken to be about 20 km/h and the direction is northerly.

ACKNOWLEDGEMENTS

This work was supported by Boğaziçi University Research Fund through grant # 94A0637.

REFERENCES

1. H. Örs , C. Aydın, 'A numerical model of the circulation in Haliç' Antalya V. Milli Mek. Kong. pp. 1993.

2. B. Gustafsson and A. Sundström, 'Incompletely parabolic problems in fluid dynamics', *SIAM J. Appl. Math.* 35. 343-357 (1978).

3. K. Kashiyama, H. Ito, M. Behr and T. Tezduyar, 'Three-step explicit finite element computation of shallow water flows on a massively parallel computer' AHPCRC 94-055 Preprint, 1994.

4. M. Kawahara and K. Kashiyama, 'Selective lumping finite element method for nearshore current',Int. J. for Num. Meths. in Fluids, 4, 71-97, 1984.

5. A.N. Brooks and T.J.R. Hughes, 'Streamline upwind/Petrov-Galerkin formulations for convection dominated flows with particular emphasis on the incompressible Navier-Stokes equations', Comp. Meths. in App. Mech. and Eng., 32,199-259, 1982.
6. O.C. Zienkiewicz and J.C. Heinrich, 'The finite element method and convection problems in Fluid Mechanics',in Finite Elements in Fluids, vol. 3, ed. Gallagher etal, Wiley, 1978
7. C. Taylor and J.M. Davis, 'Tidal propagation and dispersion estuaries', in Finite Elements in Fluids, vol. 1,pp. 95-118,ed. Gallagher etal, Wiley, 1974.
8.I.P. King, W.R. Norton, and K.R. Iceman, ' A finite element solution for two-dimensional stratified flow problems', in Finite Elements in Fluids, vol.1, pp. 133-156, ed. Gallagher etal, Wiley, 1974
9. J. Connor and J. Wang, 'Finite element modelling of hydrodynamic circulation', in Numerical Methods in Fluid Dynamics, ed. Brebbia and Connor, pp.355-387, 1974
10. G. Abraham, A.G. van Os and G.K. Verboom in., 'Transport models for inland and coastal waters', ed. H.B. Fischer, pp.1-38.
11. W.G. Gray, 'On normal flow boundary conditions in finite element codes for two-dimensional shallow water flow', Int. J. for Num. Meths. in Fluids, 4, 99-104, 1984.
12. Y. Saad and M.Schultz, GMRES: A generalized minimal residual algorithm for solving nonsymmetric linear systems. SIAM J. Sci. and Sta. Comp. 7, pp. 856-869, 1986.

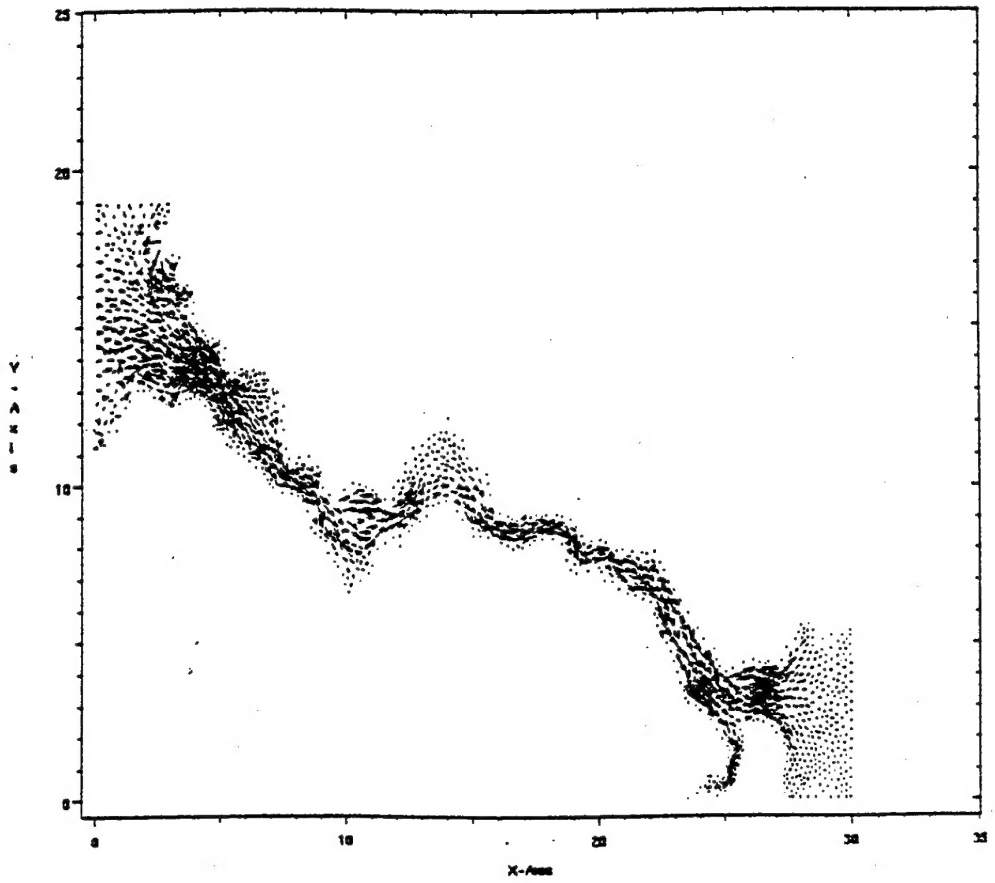

Computed flow field in the Bosphorus at t = 3000 s.